

# CHALMERS



## Novel Turbo Compressor System with Liquid Erosion Resistance *for a DME Truck*

MARINA YUDANOV

Department of Applied Mechanics  
Division of Fluid Dynamics  
CHALMERS TECHNICAL UNIVERSITY  
Gothenburg, Sweden 2016  
Master's Thesis 2016:41

## **Abstract**

This thesis investigates the prevention of liquid impingement erosion of a DME truck turbo compressor for low-pressure EGR. The work attempts to build a methodology for assessing liquid impingement erosion in this application, and to investigate the possibility of mitigating erosion by including a special nozzle in the intake. This problem is addressed with computational fluid dynamics using Star-CCM+, where one-phase simulations are run to correspond to a physical Volvo test case for the new nozzle design. Different erosion models from the literature are formulated and compared to experimental studies in the literature and then applied to this Volvo test case. The overall result is that this new design will decrease the erosive potential of exhaust gas condensate for this application.

## **Sammanfattning**

Denna masteruppsats undersöker möjligheten att förebygga vattenerosion i en DME-lastbils turbokompressor för lågtrycks-avgasåterföring (lågtrycks-EGR). Arbetet bygger en metodik för att bedöma erosionspotentialen i denna applikation, och undersöker möjligheten att motverka erosion från vattendroppar genom att inkludera ett rör i mitten av inloppet till turbokompressorn. Detta problem angrips med numerisk flödessimulering med hjälp av Star-CCM+, där enfasflöde beräknas för en fysisk experimentell arbetspunkt som av Volvo körts med det nya mittenröret. Olika erosionsmodeller från litteraturen formuleras och jämförs med experimentella studier från litteraturen, och appliceras sedan på testfallet från Volvo. Arbetets huvudresultat är att den nya designen skulle minska erosionspotentialen av de återförda avgasernas kondensat för denna tillämpning.

# Preface

This Master's thesis has been conducted jointly at the department of Applied Mechanics at Chalmers Technical University and at Volvo Trucks, both located in Gothenburg, Sweden. The work is an investigation of erosion resistance design improvement of an intake nozzle configuration for a dimethyl ether truck turbo compressor working in a low pressure exhaust gas recirculation regime. The result of this thesis will hopefully be helpful in predicting erosion for different turbo compressor operating points and designs, and a successful design of intake nozzle may aid the commercialisation of the Volvo DME truck.

I extend my humblest appreciation and warmest gratitude to the many competent, helpful, curious and patient people who have helped me throughout this thesis work: Tomas and Olivier at Chalmers University, whose encouragement, understanding and experience always helped nudge me further in my work; Magnus I. and Per A. at Volvo Powertrain in Malmö, whose eagerness to give genuine practical help and share deep knowledge of the subject was absolutely invaluable; Magnus B., Karl W., Lili H. at the Combustion Simulation Group at Volvo Trucks in Gothenburg, who selflessly indulged both my most inane and most complicated enquiries; and most importantly, my father Sergi who has given me an immeasurable amount of help and support before and during this work.

Thank you also to those people who have borne with me and discussed thesis-related topics in the search for a clear path of work and peace of mind, I cannot name all but a few of you are: Srdjan S., Björn H., Anders M., Calle L., my mother Natasha, the guys on level three and Oscar C.

Contact information to the author:

Marina Yudanov: [yudanov@student.chalmers.se](mailto:yudanov@student.chalmers.se)

# Contents

<b>1</b>	<b>Introduction</b>	<b>1</b>
1.1	Background . . . . .	1
1.2	Purpose . . . . .	2
1.3	Limitations . . . . .	2
<b>2</b>	<b>Theory</b>	<b>4</b>
2.1	Turbomachinery . . . . .	5
2.1.1	Radial Compressors . . . . .	7
2.1.2	Compressor Map . . . . .	8
2.1.3	Non-Dimensional Numbers Describing Compressor Performance . .	10
2.2	Emerging Green Fuel Dimethyl Ether . . . . .	10
2.3	Turbocharging . . . . .	11
2.4	Exhaust Gas Recirculation (EGR) . . . . .	12
2.4.1	High-Pressure EGR . . . . .	12
2.4.2	Low-Pressure EGR . . . . .	13
2.4.3	Water in DME Exhaust Gas Recirculation . . . . .	13
2.5	Erosion by Liquid Impingement . . . . .	14
2.5.1	Liquid Impingement Erosion in Turbo Compressors . . . . .	15
2.5.2	LIE Dependence on Impact Velocity . . . . .	16
2.5.3	LIE Dependence on Droplet Size . . . . .	16
2.5.4	LIE Relation to Cavitation Erosion . . . . .	16
2.5.5	LIE Dependence on Both Impact Velocity and Droplet Diameter .	17
2.5.6	LIE Dependence on Droplet Impact Pressure . . . . .	17
2.5.7	LIE Dependence on Impact Angle . . . . .	19
2.5.8	Previous Experimental Work on LIE . . . . .	19
2.5.9	Previous Relevant Computational Work . . . . .	20
2.5.10	Liquid Impingement Erosion Mitigation . . . . .	21
2.6	Computational Fluid Dynamics . . . . .	21
2.6.1	General . . . . .	22

2.6.2	<i>y</i> + Wall Refinement . . . . .	22
2.6.3	CFD for Erosion . . . . .	23
2.6.4	Basic Multiphase Flow Theory . . . . .	24
<b>3</b>	<b>Method</b>	<b>26</b>
3.1	The Turbo Compressor . . . . .	27
3.2	CFD Problem Definition . . . . .	28
3.2.1	Progression of CFD Simulations . . . . .	28
3.2.2	Identifying Operational Points to Investigate . . . . .	29
3.2.3	Geometry and Simplifications . . . . .	34
3.2.4	Mesh Models . . . . .	38
3.2.5	General Flow Models . . . . .	42
3.2.6	Wall Treatment . . . . .	42
3.2.7	Turbulence Modelling . . . . .	43
3.2.8	Impeller Rotation Modelling . . . . .	43
3.2.9	Solution Methodology and Convergence Criteria . . . . .	44
3.2.10	Boundary and Initial Conditions . . . . .	45
3.2.11	Two-Phase Modelling . . . . .	46
3.2.12	Grid Independence . . . . .	47
3.3	Liquid Impingement Erosion Analysis . . . . .	48
3.3.1	Making Use of Previous Experimental Work on LIE . . . . .	49
3.3.2	LIE Dependence on Impact Velocity . . . . .	51
3.3.3	LIE Dependence on Droplet Size . . . . .	52
3.3.4	LIE Relation to Cavitation Erosion . . . . .	53
3.3.5	LIE Dependence on Both Impact Velocity and Droplet Diameter . . . . .	53
3.3.6	LIE Dependence on Droplet Impact Pressure . . . . .	53
3.3.7	Making Use of Previous Relevant Computational Work . . . . .	54
3.3.8	LIE Dependence on Impact Angle . . . . .	55
<b>4</b>	<b>Results</b>	<b>56</b>
4.1	CFD Results . . . . .	57
4.1.1	Cases III and IV . . . . .	57
4.1.2	Effect of Overall Mesh Refinement on Calculated Efficiency . . . . .	68
4.2	Liquid Impingement Erosion Investigation . . . . .	69
4.2.1	Making Use of Previous Experimental Work on LIE . . . . .	69
4.2.2	Previous Relevant Computational Work Applied . . . . .	70
4.2.3	LIE Dependence on Impact Velocity . . . . .	71
4.2.4	LIE Dependence on Droplet Size . . . . .	71
4.2.5	LIE Relation to Cavitation Erosion . . . . .	72
4.2.6	LIE Dependence on Both Impact Velocity and Droplet Diameter . . . . .	72
4.2.7	LIE Dependence on Droplet Impact Pressure . . . . .	75
4.2.8	LIE Dependence on Impact Angle . . . . .	77
<b>5</b>	<b>Discussion &amp; Future Prospects</b>	<b>78</b>

5.1	CFD . . . . .	79
5.1.1	Geometry . . . . .	79
5.1.2	Mesh . . . . .	79
5.1.3	Choice Of Models . . . . .	80
5.1.4	Reaching and Evaluating Convergence . . . . .	80
5.2	Liquid Impingement Erosion . . . . .	80
5.2.1	LIE Indicators . . . . .	81
5.2.2	LIE Predictors . . . . .	81
5.3	Overall Drawbacks and Considerations . . . . .	81
5.3.1	Flow Interpretation and Operating Points . . . . .	82
5.4	Accuracy of Compressor Map . . . . .	82
5.5	Conclusions . . . . .	82
	<b>Bibliography</b>	<b>84</b>
	<b>Appendix A Deriving Compressible Flow Relations</b>	<b>88</b>
	<b>Appendix B Relating Pumps by Flow Coefficient</b>	<b>91</b>
	<b>Appendix C Derivation of Explicit Droplet Impulse</b>	<b>92</b>
	<b>Appendix D Erosion of Coal Ash on Aluminium</b>	<b>94</b>
	<b>Appendix E Karstadt et al. Study Parameters</b>	<b>95</b>
	<b>Appendix F Grid Independence Study</b>	<b>97</b>
	<b>Appendix G Fraction of Particles Impinged</b>	<b>98</b>
	<b>Appendix H Results For Cases I and II</b>	<b>100</b>
	<b>Appendix I Calculation of Stokes Number</b>	<b>104</b>
	<b>Appendix J Mixing Temperature Cases III-IV</b>	<b>106</b>

# List of Abbreviations

<b>CAC</b> Charge Air Cooler	Heat exchanger for cooling pressurised air that is to enter engine cylinders
<b>CFD</b> Computational Fluid Dynamics	-
<b>EGR</b> Exhaust Gas Recirculation	Engine operation regime
<b>HP</b> High Pressure	-
<b>ICE</b> Internal Combustion Engine	-
<b>LE</b> Leading Edge	Foremost part of compressor blade, first to meet flow
<b>LIE</b> Liquid Impingement Erosion	-
<b>LP</b> Low Pressure	-
<b>TC</b> Turbo Charger	Joint turbine and compressor using energy in exhaust gas to pressurise intake gas to cylinders

# List of Symbols

Symbol	Meaning	Unit, Value
$A$	Area	[m <sup>2</sup> ]
$a$	Sound speed in current medium	[m/s]
$c$	Bulk gas velocity	[m/s]
$\dot{m}$	Mass flow	[kg/s]
$M$	Mach number	[–]
$P$	Pressure	[Pa]
$\rho$	Density	[kg/m <sup>3</sup> ]
$R$	Gas constant for dry air	287 [J/kgK]
$T$	Temperature	[°C or K]
$\gamma$	Ratio of specific heats	[–]
$\varepsilon$	Erosion rate as: mg material loss per g impacted particle	[mg/g]
$\zeta$	Cumulative erosion of main blade as: mg erosion of main blade	[mg]
<b>Subscripts (unless explicitly stated otherwise)</b>		
$0$	Stagnation property	
$c$	Continuous phase	
$d$	Dispersed phase	
dyn	Dynamic property	
$l$	Liquid property	
$s$	Isentropic quantity	

# 1

## Introduction

This section outlines the background, purpose and limitations of this work. An overview of the problem is given and its relevance for engineering is presented. The framework for finding a solution to the given task is explained.

## 1.1 Background

Heavy duty trucks are to a large extent one of the backbones of the globalised and industrialised society today, and the great transportation networks allow for development of trade and growth of welfare around the world. Volvo is one of the major suppliers of transport solutions, with trucks being a large part of the company. It is no secret that the transportation sector is overwhelmingly fossil-fueled, being more than 95% oil-dependent at the start of this decade, even in Europe [1]. Solving this problem is at the heart of the question for today's industrialised society: how to keep and improve the level of civilisation and welfare that has been achieved, while at the same time not compromising the needs of future generations? Transport by road is responsible for one-fifth of EU carbon dioxide emissions [2], and trucks and other heavier vehicles account for a quarter of this [3]. In other words, heavy duty vehicles account for 5% of the total EU emissions of carbon dioxide.

Throughout the decades, much effort has been put into mitigating emissions from road-based transports. Examples include catalysts used for reducing NOx emissions, or optimising engine efficiency to reduce specific CO<sub>2</sub> emissions. The diesel engine has incrementally become less and less harmful to the environment. The use of turbochargers has been yet one measure on this journey, improving the engine thermodynamics for higher efficiency and reduced exhaust emissions [4]. However, any internal combustion engine will always be encumbered with the basic fact of burning in air: hydrocarbons and oxygen react to form carbon dioxide and water. This chemical fact means that in order to be carbon-neutral, trucks will need to use a fuel with net zero carbon dioxide contribution. This is achievable if use is made of renewable carbon, i.e. biomass-based fuel.

As far as biofuels go, dimethyl ether, or DME, is one of Volvo Trucks' strongest future green fuel technologies. It performs at the very top of Volvo's grading system for potentially carbon dioxide neutral fuels [5]. It may also reduce the need for catalysts in the exhaust gas aftertreatment. This is in part because DME burns without soot, and the exhaust gas can then be re-used in the engine to a higher degree than diesel exhaust gas can. Instead of releasing the exhaust into the atmosphere, it can be sent into the cylinders again to mix with the normal intake air. Doing this reduces the peak temperatures of combustion which in turn reduces NOx emissions.

The re-routing of exhaust gas into the cylinders can be done in different ways: by a short route or long route. Which route is taken depends on the pressure of the exhaust. Short-route EGR is used when the exhaust has a high pressure; then the exhaust gas goes almost immediately back into the cylinders. Long-route EGR is used when the exhaust is at a lower pressure, and is made to pass a device called a turbocharger before entering the cylinders again. The turbocharger, or turbo, has a compressor and is necessary because combusting a pressurised gas results in more power from the engine [4]. One problem with compressing the low-pressure exhaust is that it contains condensate which

causes liquid impingement erosion of the compressor. This erosion is detrimental to compressor performance and lifetime [6]. Today, this erosion is one of the obstacles to taking advantage of low-pressure EGR for lower NO<sub>x</sub> levels.

Volvo is developing a way to feed the recirculated exhaust gas without damaging the blades of the compressor. Modifying the nozzle that feeds exhaust gas and intake air to the compressor may be an alternative. Preliminary physical testing with one altered nozzle design has indicated positive results in terms of compressor blade wear reduction. The next step is to support this with computer software simulations of the way the mixed exhaust gas/intake air flow impinges on the blades. A computational fluid dynamics (CFD) analysis is to be made to identify a nozzle design that reduces compressor wear caused by liquid impingement erosion.

Erosion, and especially liquid impingement erosion, is a very complex field where many different approaches are used to calculate or estimate damage and wear on solid materials. This thesis aims to make use of previous work to suggest a methodology for estimating liquid impingement erosion for compressors in DME trucks.

## 1.2 Purpose

The aim of this project is to aid the development of a more liquid erosion-resistant nozzle for low-pressure exhaust gas recirculation system in Volvo's dimethyl ether trucks.

Volvo Trucks have performed preliminary physical engine tests on one new nozzle. This work will attempt to replicate these tests through simulation using computational fluid dynamics (CFD), and then use the results of these simulations coupled with liquid erosion theory and previous studies to suggest design alterations in order to reduce the liquid erosion potential.

The ambition is to design a pipe to minimise the impact that the water droplets in the exhaust gas have on the blades. This should minimise the erosive damage.

## 1.3 Limitations

The problem of CFD-aided nozzle design for better liquid erosion resistance for low pressure EGR turbocharging is extensive. Clear and restrictive limitations have to be set to fit into the resource and time framework of a master's thesis.

Limitations of this project include:

- The one-phase simulations of the turbo compressor are limited to a simplified geometry. Description of and rationale for these CFD-related assumptions are given in Section 3.2.3.

- The possibility of liquid erosion in a turbo compressor exists for a range of different operational conditions with exhaust gas recirculation and can depend on many different factors. For the purpose of this thesis, one operational point with high likelihood of condensation is chosen with the help of Volvo Trucks. Experimental data on pressures, temperatures and water content in the exhaust gas is available for this point, for a DME engine.
- Two-phase simulations are not the focus of this thesis. The ambition is instead to predict erosion using one-phase simulations and appropriate assumptions. An analysis of the one-phase simulation results together with a review of appropriate CFD methods for future two-phase simulations is given and chosen methods are backed up with feasibility calculations for the problem at hand. The many limitations and assumptions associated directly with two-phase CFD are given in section 3.2.11.
- The only aspect of the engine considered for adaptation in order to increase liquid erosion resistance is adaptation of the central nozzle. It is important to keep the existing truck design as conventional as possible because of cost considerations.
- Experimental validation of the erosion potential predicted in this work is outside of the scope of this thesis.

Volvo will provide characteristics of the exhaust gas and boundary conditions. The amount of water in the mixture of exhaust gas and intake air will be in accordance with Volvo data for the operating conditions investigated.

# 2

## Theory

Four topics are central to this thesis: turbomachinery in general and radial compressors in particular; turbocharging in an internal combustion engine combined with exhaust gas recirculation; liquid impingement erosion (LIE), and finally computational fluid dynamics (CFD). This chapter outlines a limited selection of knowledge underlying each of these areas which may be helpful in following the forthcoming chapters.

## 2.1 Turbomachinery

A generic turbomachine is defined as a device in which energy is transferred to or from a continuously flowing fluid by the dynamic action of one or more moving blade rows [7]. A compressor is a turbomachine that increases the pressure of a gas flowing through it at the expense of work to rotate the blades. The flow in compressors needs to be analysed using compressible gas theory, as the gas is moving with a velocity high enough to affect its properties.

Important quantities for turbomachine performance analysis are pressures, temperatures, mass flows and properties of the gas medium as well as its velocity through the machine. For turbomachines, the relevant quantities are often expressed as stagnation/total quantities: these are defined as the total amount of e.g. pressure or temperature that a moving fluid would have if it was brought adiabatically to rest. The definitions of stagnation properties are:

$$T_0 = T\left(1 + \frac{\gamma - 1}{2}M^2\right) \quad (2.1)$$

for temperature, where  $T$  is the static temperature,  $\gamma = c_p/c_v$  is the ratio of specific heats, and  $M$  is the Mach number: the relation of the fluid speed to the speed of sound in current medium.

Stagnation pressure can be found by:

$$\frac{P_0}{P} = \left(\frac{T_0}{T}\right)^{\frac{\gamma}{\gamma-1}} = \left(1 + \frac{\gamma - 1}{2}M^2\right)^{\frac{\gamma}{\gamma-1}} \quad (2.2)$$

It can be seen from Eqs. 2.1 and 2.2 that if the Mach number is zero, i.e. the fluid is at a standstill, then stagnation properties  $T_0$ ,  $P_0$  are equal to static properties  $T$ ,  $P$ . With an increasing Mach number i.e. an increase in the fluid speed compared to the sound speed, the stagnation properties grow.

Efficiency for a compressor is the relation of temperature increase for a desired ideal compression, compared to the actual temperature increase that occurs. Assuming, as is common to do, adiabatic conditions and constant specific heats, it follows that:

$$\eta = \frac{T_{02s} - T_{01}}{T_{02} - T_{01}} \quad (2.3)$$

where  $T_{01}$  represents the stagnation temperature at inlet,  $T_{02}$  the stagnation temperature at outlet and  $T_{02s}$  represents the stagnation temperature that would be achieved for an ideal compression. This principle of ideal vs. non-ideal compression can be seen in a Mollier diagram. Figure 2.1 shows that an ideal compression is going “straight up” to

take the shortest distance from  $P_{01}$  to  $P_{02}$  at  $T_{02s}$ , whereas the real compression results in a diagonal line up to  $T_{02}$  which is higher than  $T_{02s}$ .

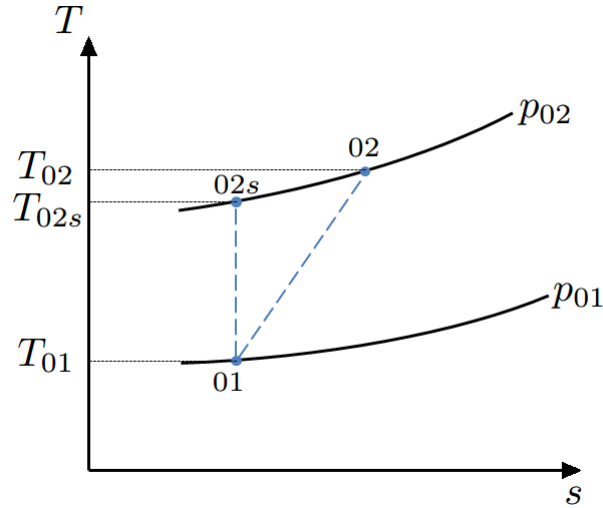


**Figure 2.1:**  $T$ - $s$  diagram showing a real compression from  $p_{01}$  to  $p_{02}$ . An ideal isentropic compression would have caused a temperature increase from  $T_{01}$  to  $T_{02s}$ , while the real compression brings a greater increase: from  $T_{01}$  to  $T_{02}$ .

Dividing both numerator and denominator in Eq. 2.3 by  $T_{01}$  leads to:

$$\eta = \frac{\frac{T_{02s} - T_{01}}{T_{01}}}{\frac{T_{02} - T_{01}}{T_{01}}} \quad (2.4)$$

or:

$$\eta = \frac{\frac{T_{02s}}{T_{01}} - 1}{\frac{T_{02}}{T_{01}} - 1} \quad (2.5)$$

and substituting the isentropic temperature ratio for the pressure ratio expression from Eq. 2.2 finds:

$$\eta = \frac{\left(\frac{P_{02}}{P_{01}}\right)^{\frac{\gamma-1}{\gamma}} - 1}{\frac{T_{02}}{T_{01}} - 1} \quad (2.6)$$

This describes the so-called total-to-total efficiency of the compression process in a turbo-machine.

### 2.1.1 Radial Compressors

A radial compressor is a device where flow comes in axially to a rotor (rotating blade configuration) and flows out radially. In doing so its pressure increases through the work done by the blades. Note that this is the opposite of the working principle of a turbine, which takes a high-pressure fluid and generates work. An example of a radial compressor device can be seen in Fig. 2.2. Radial compressors consist of four main parts: intake, rotor, diffuser and volute. The intake is a pipe which directs the fluid into the rotor in a desirable way (not shown in Fig. 2.2). The rotor (or, for radial compressors, *impeller*) is a spinning blade configuration that accelerates the fluid by whirling it outward, increasing both its static pressure and velocity. After the impeller, the high-energy fluid enters the diffuser, where it slows down and increases significantly in pressure. The final part, the volute (or scroll), collects this fluid and delivers it, radially, to the next place it needs to be. The volute in Fig. 2.2 is the lighter-coloured pipe curling around the impeller like a snail shell. In both the diffuser and volute, dynamic pressure is converted to static pressure [7].



**Figure 2.2:** A view into the intake of a turbo compressor. The flow enters perpendicular to the plane of the propeller-looking inducer section of the impeller. Flow exits at the round pipe outlet to the top left in this figure. Picture found online [8].

A sketch showing how the velocities of admitted gas and of blades are related is shown in Fig. 2.3. The vector sum of relative velocity  $w$ , and blade velocity  $U$ , is the gas velocity  $c$ . These types of velocity triangles are often employed in turbomachinery design estimates.

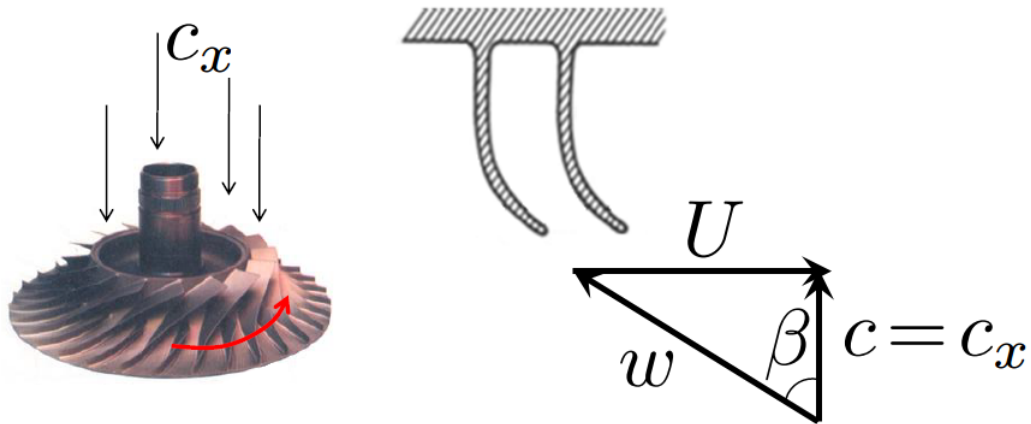


**Figure 2.3:** A sketch of the velocity triangles on inlet to the radial compressor. The left part of the figure shows a side view, while the right side is a schematic view from above of the tops of the blades closest to the reader.  $U$  is blade velocity,  $w$  relative velocity and  $c$  gas velocity. Purely axial intake means that the axial component, here  $c_x$ , is the same as  $c$ . Figure adapted from Grönstedt [9].

### 2.1.2 Compressor Map

Compressor performance is characterized by mass flow, achieved stagnation pressure increase, rotational speed and temperature. Designers achieve desired performance by sizing the compressor and shaping the flow passages and blades. It is not possible to analytically determine how a given compressor will perform for a certain mass flow and rotational speed. Empirically derived diagrams (or *maps*) are often used to identify which parameters will give a certain performance for a specific machine.

An example of such a compressor map can be seen in Fig. 2.4. Along the  $x$  axis is the (corrected) mass flow. Along the  $y$  axis is the pressure ratio. Corrections are made when it is necessary to determine compressor performance for non-standard operating conditions such as high altitudes or low temperatures. The pressure ratio on the  $y$  axis is given as the full pressure ratio, i.e. from inlet pipe to the outlet of the volute/scroll. The lines going from left to right in the diagram and bending more and more downwards mark a constant (corrected) rotational speed of the impeller. Their curving downwards shows that, for progressively higher mass flows, the same rotational speed will deliver less and less of a pressure rise. The ellipses in the map define the constant efficiency operational areas. It is desirable to operate the compressor at higher efficiencies.

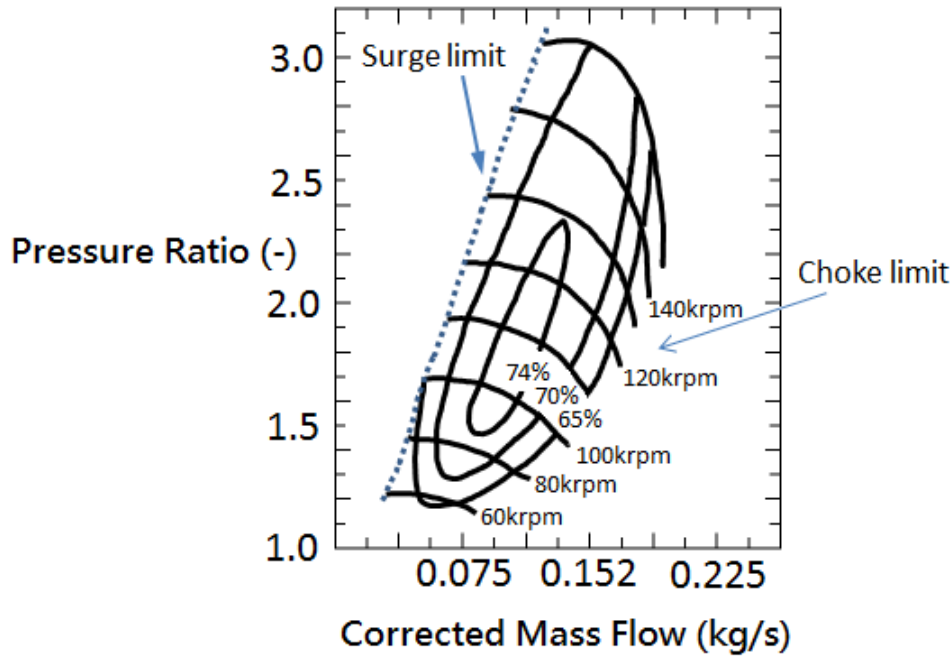


**Figure 2.4:** A view of a typical compressor map showing pressure ratio for different mass flows at different rotational speeds, achieving a range of efficiencies.

The region inscribed by the ellipses is where the compressor can function well. Note that the efficiencies become lower towards the outskirts of the contoured region. The region to the left of the map where the shapes terminate is called the surge region, and to the far lower right is the choke limit. The choke limit is reached when the flow speed goes to Mach number one across some section of the compressor, meaning the mass flow can no longer increase, a condition associated with pressure and shock losses. The surge limit is when the compressor no longer can deliver a higher pressure ratio [7], and shows an aerodynamically unstable behaviour risking the integrity of the entire system.

### Useful Compressible Flow Relations

Dealing with compressible flow means taking into account physical effects of gas behaviour which are neglected in an incompressible analysis. Combining these relations with e.g. the continuity equation can give valuable information about gas properties throughout the turbomachine. The continuity equation gives:

$$\frac{\dot{m}}{A} = \rho c = \frac{pc}{RT} \quad (2.7)$$

where  $\dot{m}$  is the mass flow (kg/s),  $A$  is the cross-sectional area ( $\text{m}^2$ ),  $\rho$  is the flow density

( $\text{kg}/\text{m}^3$ ),  $c$  is flow velocity (m/s),  $R = 287 \text{ J}/\text{kgK}$  is the dry air gas constant and  $T$  is the temperature (K). This combined with the compressible flow relations from Eq. 2.2, relates the stagnation pressure to static pressure, mass flow, area, and stagnation temperature according to:

$$P_0 = P \left( \frac{1}{2} + \sqrt{\frac{1}{4} + \frac{\gamma - 1}{2\gamma} \left( \frac{\dot{m}}{pA} \right)^2 RT_0} \right)^{\frac{\gamma}{\gamma-1}} \quad (2.8)$$

This relationship makes possible the determination or approximation of the stagnation pressure at a certain point in the compressor without knowing the Mach number. The full derivation of this expression can be found in Appendix A.

### 2.1.3 Non-Dimensional Numbers Describing Compressor Performance

Turbomachine designers make use of non-dimensional groups of variables to relate similar machines and their performances. For example, if two pumps are identical in everything except their diameter (size), this is called dynamic similarity. They can deliver the same performance (i.e. desired pressure rise at certain mass flow) for different rotational speeds. The flow coefficient can then be used to determine which of the two pumps will have to rotate faster to deliver the same performance.

Flow coefficient is defined as:

$$\phi \propto \frac{Q}{ND^3} \quad (2.9)$$

where  $Q$  is the flow rate,  $N$  represents the rotational speed and  $D$  is the diameter. An example of how to use the flow coefficient when comparing two pumps (or compressors) is given in Appendix B, where it is derived that a larger compressor needs to rotate at a lower number of revolutions per unit time to achieve the same pressure ratio at given flow rate. This relates operating points for different compressors.

## 2.2 Emerging Green Fuel Dimethyl Ether

Dimethyl ether, DME, is the simplest ether with the chemical formula  $\text{CH}_3\text{OCH}_3$ . DME is one of the most promising biofuels existing for road transport today. It is a colorless, non-toxic gas that liquifies under light pressure, and was initially developed for use in aerosols. DME can be manufactured from different sources, including natural gas, organic waste or biomass, and has a low carbon footprint [10].

DME can be used in compression ignition diesel engines with only small modifications compared to other technologies [11], which is a major advantage considering the tech-

nological maturity of the internal combustion engine. This is because DME has good ignition quality and a high cetane number. Furthermore, it gives very low emissions of other particles when combusted. Volvo Trucks have the ambition to launch alternative fuel trucks running on DME in the future. In order to make them as competitive as possible, making use of all potential advantages of this special fuel is absolutely necessary. Using exhaust gas recirculation to a large extent is desirable to keep NO<sub>x</sub> emissions down to anticipate future emission legislation.

## 2.3 Turbocharging

The temperature and velocity of the exhaust gas leaving the cylinders of an internal combustion engine are very high. Instead of directly expelling them to the surroundings, a turbocharger makes use of the remaining exhaust gas energy. In a connected arrangement of turbine and compressor, the exhaust gas expands in the turbine and generates work that is directly used by the compressor in compressing air that is taken into the engine. A figure of this arrangement, called a turbocharger, can be seen in Fig. 2.5.

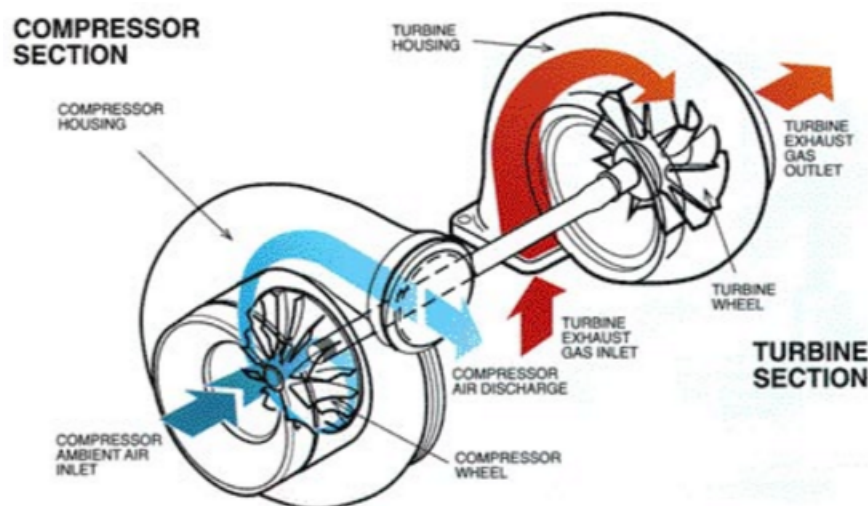


**Figure 2.5:** A schematic of a typical turbocharger, with hot gas (right side) turning the turbine which allows the compressor to do work on the intake gas (left side). Figure adapted from Super Street Network [12].

Using a turbocharger is a way of harvesting otherwise wasted energy. It is highly desirable to increase the intake air density, as the power output of an internal combustion engine is directly related to the air mass flow through the engine [4]. The more air that can be taken in to the cylinders of the engine, the more heat can be introduced through more fuel, and the more work can be done.

Increasing density by compression, however, increases the temperature of the air. Cool-

ing this compressed air can increase the density further, as well as lower combustion temperatures which in turn reduce NO<sub>x</sub> emissions [6]. Compression and cooling of the air before admitting it to the cylinder also increases the efficiency of the engine, and is now standard practice in practically all trucks [4].

## 2.4 Exhaust Gas Recirculation (EGR)

Not only is the exhaust gas used to run the turbocharger – it is also often to a significant extent re-routed back into the engine cylinders as combustion medium. This is because, among other things, reducing the partial pressure of oxygen in the combustion chamber means less nitrous oxides can be formed [13]. Reducing harmful emissions has been firmly on the agenda for road transport in the past decades, which is why EGR and other measures have become increasingly standard.

There are two main concepts available for re-introducing exhaust gas into the cylinders. These are usually called high-pressure and low-pressure EGR, respectively. High-pressure EGR is the more commonly used method, whereas low-pressure EGR is still beset with some technical issues. Both have advantages and drawbacks, and are described below.

### 2.4.1 High-Pressure EGR

In high-pressure EGR, exhaust gas is taken directly from the engine exhaust manifold and sent via a cooler back to the inlet of the engine. Shown in Fig. 2.6, this method is also called short-route EGR and is best used when the pressure difference between the exhaust and the cylinder inlets is high enough i.e. at high power loads. For this regime, the exhaust gas does not pass through the compressor and thus does not increase the risk of compressor erosion.

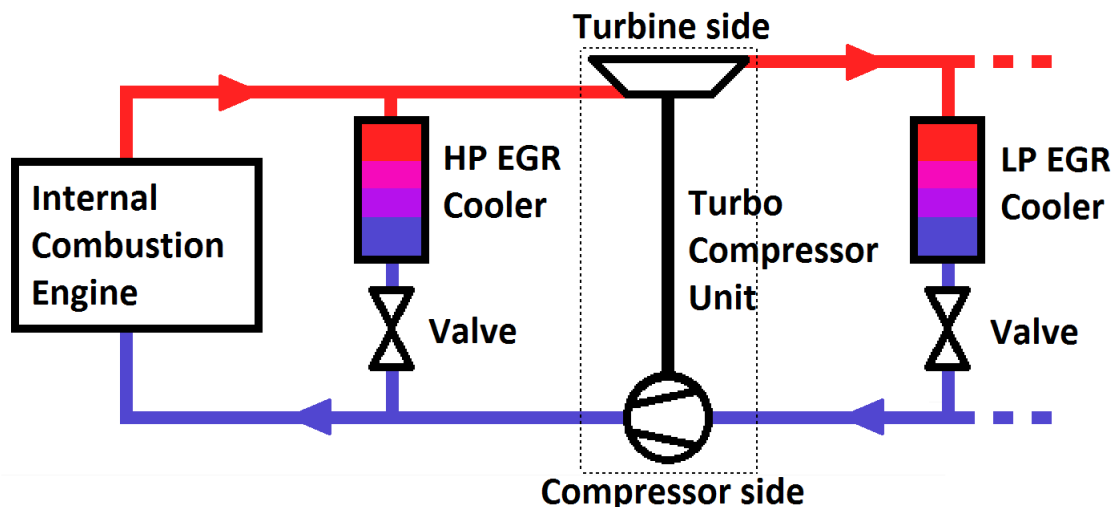


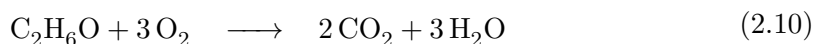
**Figure 2.6:** A schematic of the engine and different EGR paths. Note that the short-route HP (high-pressure) EGR loop does not pass the compressor. The long-route LP (low-pressure) EGR loop passes the compressor on its way back into the engine. Schematic based on standard engine design and only intended to show components immediately relevant to the understanding of this work.

### 2.4.2 Low-Pressure EGR

Low-pressure EGR is also called long-route EGR because the exhaust gas takes a longer path before getting back into the cylinders, as pictured in Fig. 2.6. One of the persisting issues with this concept is that, especially for a cold engine, exhaust gas may contain non-negligible amounts of condensate [13]. Namely, condensation of water droplets may occur as exhaust gas is mixed with the ambient air taken into the compressor. This happens mainly at cold start and at low recirculated exhaust gas temperatures, such as  $T < 60^\circ\text{C}$  [14, 15]. As a low temperature is desirable for other reasons (see Section 2.3), keeping it low enough while avoiding harmful droplets is a trade-off.

### 2.4.3 Water in DME Exhaust Gas Recirculation

The combustion in a diesel engine is hydrocarbons reacting with oxygen in air to form carbon dioxide and water. For dimethyl ether, which has the chemical formula  $\text{C}_2\text{H}_6\text{O}$  or  $\text{CH}_3\text{O}_{1/2}$ , the stoichiometry dictates:



The molar mass of  $\text{CH}_3\text{O}_{1/2}$  is 23 g/mol, yielding  $1.5\text{H}_2\text{O}$  after combustion. As the

molar mass for water is 18 g/mol, some 23 g of DME will yield  $18 \cdot 1.5 = 27$  g of water. Hence, every gram of DME fully combusted gives  $27/23 = 1.174$  g of water formed. As a reference, diesel combustion gives 1.21 g of water per gram of diesel, and natural gas (methane) yields 2.25 g of water per gram of natural gas [16].

In practice, combustion in engines is often performed at a different air-to-fuel ratio than the stoichiometric one. Having more air available than is stoichiometrically necessary according to Eq. 2.10 makes no change in the theoretical amount of water produced as the air does not generally add significant amounts of hydrogen. Knowing how much fuel is combusted allows an estimate of how much moisture there is in the exhaust gas (assuming complete combustion). The proportion of condensate and vapour in this moisture content is however unknown. Typically, the lower the temperature, the more condensate will exist.

## 2.5 Erosion by Liquid Impingement

Erosion is the progressive wearing down of a target material by the repetitive impact of some other fluid or material [17]. It is recognised as an important and difficult issue within many engineering fields, with the the primary concern often being a performance decrease or even total failure resulting from the degradation of material due to the erosion wear [18]. Erosion – which is purely mechanical – is not to be confused with corrosion, where wear can occur because of chemical reactions between the fluids and materials involved.

There are many factors included in determining the magnitude of liquid droplet erosion, such as: droplet amount, size, speed, interaction, temperature, impingement angle and liquid and material properties. This section presents a collection of different relevant theoretical, computational and experimental studies of erosion in general and liquid impingement erosion in particular. The biggest factors in liquid impingement erosion are brought up and the most prevalent mechanisms are presented.

Literature suggests that erosion by liquid particle impact occurs in different phases: first, there is an incubation period where the material weight loss is almost undetectable. The existence of an incubation period is widely recognised [19–21]. After this, Soni suggests that the erosion abruptly takes on a significant and linear character, the rate being largely constant [21]. After these two phases is the final erosion phase which is less explored.

Engineering spheres other than LP EGR in turbo compressors which entail a high propensity for liquid erosion include, for example, steam turbines, gas/liquid flows in pipe channels and bends or aircraft compressors and propellers. In steam turbines, a submicron fog forms and is deposited on blades, collecting into a thin water film. When this film is flung off blades it is called “coarse water” (on the order of 10 – 200  $\mu\text{m}$ ), and erodes downstream blades [22, 23].

### 2.5.1 Liquid Impingement Erosion in Turbo Compressors

It is known that erosion is a common problem in turbomachinery applications. Applications where a turbulent flow is disturbed by sudden changes in the flow system geometry are subject to the most severe erosion [18]. A developed turbulent flow will have much larger velocity gradients at walls and boundaries than a laminar flow. Naturally, fluid motion affected by high-speed blades falls into this category.

Turbo compressor erosion due to exhaust gas recirculation is caused by droplets condensing from the moisture in the exhaust gas. These droplets impact the compressor blades at a high impact velocity because of the very high speed with which the blades are rotating. Repeated impacts of this kind eventually wear down the blades. Turbo compressors are often made from aluminium that is more susceptible to erosion than other “harder” metals. A different material such as a titanium alloy could be substituted to increase erosion resistance, but this increases both weight and cost of the turbocharger.

Turbo compressors have a typical pattern of erosion by particles or droplets, characterised by material loss at the leading edge of the blades, which is aggravated towards the tip. Such a pattern can be seen in Fig. 2.7. This may be because the initial droplet impact occurs on the leading edge, and also because the speed of the blade is higher closer to the tip, causing higher impact velocities and more severe erosion.

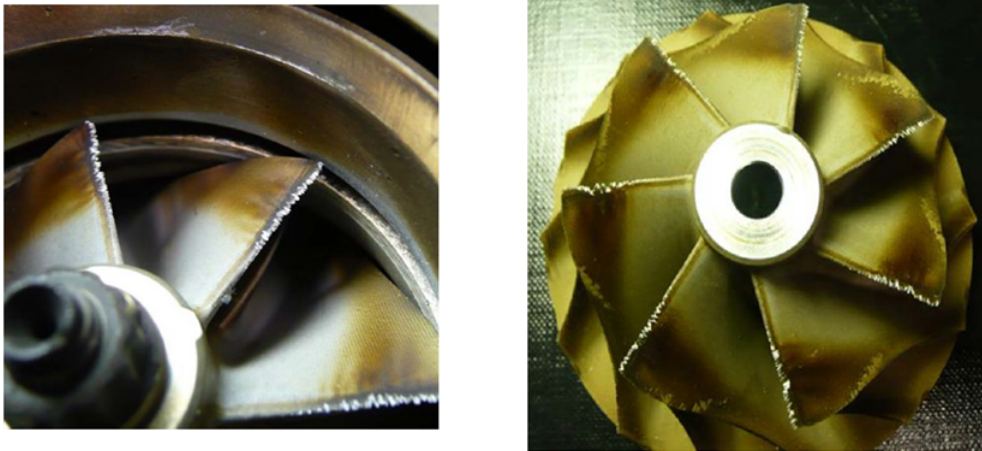


**Figure 2.7:** A view into the inlet of the impeller for two highly eroded compressor impellers [24]. For turbo compressors, it seems that the leading edge tip always suffers most from erosion. This coincides with the increasing blade speeds on the outer parts of the blades as mentioned in Section 2.5.2.

### 2.5.2 LIE Dependence on Impact Velocity

As mentioned in Section 2.1.1, the relative velocity  $w$  of the fluid on the blades is a combination of the fluid absolute velocity  $c$  and the blade velocity  $U$ . Relative velocity is interpreted as impact velocity for droplets: assuming that droplets will travel at the same speed as the gas, and that droplet speed is constant or varies little along the blade radius, the impact velocity then depends mostly on  $U$ . This blade tangential speed  $U$  at a specific radius  $r$  can be calculated from the rotational speed  $\Omega$  by  $U = \Omega r$ , where  $U$  increases outward along the radius. Using the velocity triangles from Fig. 2.3, the impact (i.e. relative) velocity of the droplets will reach a maximum farthest out on the blades.

Starzmann et al. have suggested that the bulk of droplet erosion occurs, at least for steam turbines, mainly when impact velocities on the moving blades reach above 300 m/s [25]. Uhlig and Revie have suggested as a rough estimate that bulk flow velocity can be associated to the erosion (metal loss) rate by liquid in a gas flow by an exponent of 5-8 [18]. Such an estimated relationship can be of use in preliminary considerations, despite the fact that actual erosion mechanisms have more to do with the detailed and local behaviour of the flow near boundaries.

### 2.5.3 LIE Dependence on Droplet Size

According to Ahmad et al., the blade material volume loss in steam turbines due to droplet impact erosion is proportional to droplet diameter raised to an exponent  $n$  between 3 and 5 [26]. Following from this, a fixed volume of water will cause more erosion as fewer larger droplets than many smaller ones, despite fewer discrete impact incidents.

### 2.5.4 LIE Relation to Cavitation Erosion

Erosion by liquid impingement attack is related to the destruction caused by cavitation [18, 20]. Cavitation is when a liquid undergoes a phase change to gas because of a local low-static pressure zone, causing the liquid to boil at lower temperatures than it otherwise would [7]. As the newly formed bubbles enter regions of higher pressure there are no longer favourable conditions for their existence and they collapse, causing a shock wave that can cause material destruction.

Cavitation in turbomachinery has been extensively studied, and data exists for many materials and applications. Hattori and Takinami have suggested that cavitation erosion rates and liquid impingement erosion rates could be associated by a linear correlation, after noting that cavitation maximum depth of erosion curves looked similar to liquid impingement erosion curves [20]. The same authors propose that the maximum depth

of erosion rate (in depth per time as  $\mu\text{m/h}$ ) depends on the flow velocity to the 6th or 7th power.

Toshiyuki et al. have suggested that it may be the cavitation bubbles forming inside small liquid droplets that cause liquid impingement erosion [27]. The article suggests that the equilibrium radius of such a cavitation bubble can be determined by relating the temperature-dependent surface tension of water ( $\sigma$  in  $\text{mN/m}$ ) to its vapour pressure ( $p_v$  in  $\text{kPa}$ ):

$$R_{eq} = \frac{2\sigma}{p_v} \quad (2.11)$$

If bubble equilibrium radius is smaller than droplet radius, it is suggested to be theoretically possible for cavitation to be present as a phenomenon.

### 2.5.5 LIE Dependence on Both Impact Velocity and Droplet Diameter

A theory put forward in a number of articles is that of a threshold velocity, diameter or angle [28–30], which acts as a limit below which no erosion will occur. Amelyushkin and Agafonov in 2002 used the idea that the respective materials used for steam turbine rotor blades have constant values of  $w_{th}^2 d$ , where  $w_{th}$  is threshold velocity and  $d$  is droplet diameter. Hence, the lower the diameter, the higher the threshold velocity will be for the same erosion. Also, the higher the velocity, the smaller the droplet has to be in order to avoid erosion [29].

### 2.5.6 LIE Dependence on Droplet Impact Pressure

In a study by Ahmad et al., the droplet impact pressure responsible for erosion is described by a modified water-hammer equation [31]. The mechanism of impact and shock means that lateral jetting occurs, increasing impact pressure about three times as high as the original water-hammer pressure. The modified water-hammer impact pressure that may describe the potential for erosion is:

$$p_{impact} = \rho_l a_l v_{impact} \left( 1 + \frac{k v_{impact}}{a_l} \right) \quad (2.12)$$

where  $k \approx 2$  is a constant for water,  $\rho_l$  is the density of the liquid,  $a_l$  is the speed of sound in the liquid, and  $v_{impact}$  is the droplet impact speed [17, 31]. Note that this expression is independent of droplet size.

With the help of Thomas and Brunton, the impact pressure  $p_{impact}$  from Eq. 2.12 can be used to define the impulse transferred from droplet to surface [32]. The droplet impact

pressure can be assumed to act on a circular contact area determined by the contact radius given by:

$$r_{contact} = R \frac{v_{impact}}{a_l} \quad (2.13)$$

where  $v_{impact}$  is the impact velocity,  $a_l$  is the sound speed, and  $R$  is the actual radius of the droplet. The pressure and area combine to identify impact force:

$$F_{impact} = P_{impact} A_{impact} \quad (2.14)$$

In order to relate this to what is experienced by the material, the impulse can be found by integrating the force from time  $t_1 = 0$  to the time of the water hammer pressure duration,  $t_2$ :

$$I = \int_{t_1}^{t_2} F_{impact} dt \quad (2.15)$$

where the time of water hammer is defined by:

$$t_2 = \frac{R}{v_{impact}} \left( 1 - \sqrt{1 - \frac{v_{impact}^2}{a_l^2}} \right) \quad (2.16)$$

The impulse then becomes:

$$I = F_{impact} \Delta t = P_{impact} A_{impact} t_2 \quad (2.17)$$

Developing this formula gives a dependence of impulse by water droplet as a function of acoustic speed in water  $a_l$ , droplet impact velocity  $v_{impact}$ , water density  $\rho_l$ , and droplet radius  $R$  as follows:

$$I = \left( 1 - \sqrt{1 - \frac{v_{impact}^2}{a_l^2}} \right) \rho_l (a_l + k v_{impact}) \pi R^3 \left( \frac{v_{impact}}{a_l} \right)^2 \quad (2.18)$$

The explicit derivation of this expression is given in Appendix C. It provides a method by which to evaluate erosive potential through the quantification of something physically relevant.

### 2.5.7 LIE Dependence on Impact Angle

For jet flow, an erosion correlation by Hattori et al. suggests that the material loss and maximum depth of erosion is proportional to the impingement angle of the jet as  $\sin^n \theta$  for all steels for some exponent  $n$  [19]. For an aluminium surface onto which a spray nozzle is directing water, the same authors suggested that a relationship for the mass loss could be:

$$\dot{m}_{\text{loss}} = 2.87 \cdot 10^{-9} (V \sin \theta)^{4.65} \text{ [mg/h]} \quad (2.19)$$

where  $V$  is the flow velocity and  $\theta$  is the impact angle.

For aluminium impinged by coal ash particles, Tabakoff and Hamed have developed a relationship between impact angle and erosion which suggests that erosion is greatest for an angle of attack in the region of  $\beta = 25^\circ$ , not changing between velocities  $U = 85 - 137 \text{ m/s}$  [33].

Erosion damage is formulated by Tabakoff and Hamed as the rate of mass loss of the impacted part compared to the mass of the impinging particles, for solid particles [34, 35]. The equation is presented as:

$$\varepsilon = A_1(1 + A_2 \sin(A_3 \beta_1))^2 (V^2 \cos \beta_1^2 (1 - (1 - A_4 V \sin \beta_1)^2)) + A_5 (V \sin \beta_1)^4 \quad (2.20)$$

where  $V$  is the particle speed before impact,  $\beta_1$  is the impact angle in radians, and the coefficients  $A_i$ ,  $i = 1, 2, 3, 4, 5$  are empirically determined constants. For the case of coal ash particles impacting aluminium, the coefficients are given in Appendix D. This relationship does not differentiate between different droplet sizes, instead taking the total mass of impinged droplets to be the more pertinent quantity.

### 2.5.8 Previous Experimental Work on LIE

One of the few systematic experimental investigations into the effects of liquid impingement erosion on turbo compressor blades was conducted by Karstadt et al. [36]. They directed mono-dispersed single droplet streams onto 2/3 of the radial length of the centrifugal compressor blades and noted the resultant erosion in terms of both leading edge erosion and blade erosion.

The study was designed to investigate the dependence of erosion on droplet size and on rotational speed (i.e. impact velocity). In the first experiment, rotational speed and total volume of water was kept constant while four cases of different droplet sizes were conducted. In the second experiment, the droplet size which had appeared to give the highest specific erosion (erosion per mass of droplet) was used to conduct four cases

with different rotational speeds. The total volume of water was kept the same for each case.

Karstadt et al. noted that larger droplets caused more leading edge erosion up to a certain size. For droplets larger than  $d_3 = 470 \mu\text{m}$ , a further increase in erosion was marginal. In the investigation of rotational speed, it was noted that higher rotational speeds gave more erosion, but again a certain saturation was noted above 100 krpm. The study gives results for erosion in picture form for two investigations: a variation of droplet diameter at a fixed rotational speed, and a variation of rotational speed for a fixed droplet diameter. As the resulting erosion is given in photographic form (as opposed to e.g. grams of material loss), it is difficult to quantify for future use. Nevertheless, in order to grasp the trends identified by this study, the results for the different operating cases are given here in the form of Table 2.1 to show what cases were looked at and to give an approximate rating for the erosion suffered. These physical results can later be compared to predictions from erosion formulae.

**Table 2.1:** Summary of the cases tested and the visually assessed erosion results from Karstadt et al. study.

OBSERVED EROSION	Droplet diameter			
Rot. speed	$d_1 = 153 \mu\text{m}$	$d_2 = 340 \mu\text{m}$	$d_3 = 470 \mu\text{m}$	$d_4 = 1120 \mu\text{m}$
$n_1 = 50 \text{ krpm}$	-	-	zero	-
$n_2 = 100 \text{ krpm}$	-	-	minimal	-
$n_3 = 150 \text{ krpm}$	minimal	moderate	heavy	heavy
$n_4 = 200 \text{ krpm}$	-	-	heavy	-

Another relevant finding was for water admitted into the compressor from inlet pipe walls (wall film admission). Such water was expected to cause large droplets to be flung off and to hit the blades at the outer edge where the blade speed is highest, and therefore cause much erosion. In a side experiment however, wall film admission did not show more erosion. This was explained by the existence of recirculation vortices at the leading edge tip, which atomised the large water droplets into smaller ones, decreasing the erosion potential greatly. Karstadt et al. suggest that it is the relative velocity between droplet and continuous medium that causes break-up [36]. Other findings were that the splitter blades are generally erosion-free. The conclusion was that below approximately 250 m/s blade speed, water droplets seem to have low erosion potential for this application [36].

### 2.5.9 Previous Relevant Computational Work

Ghenaiet performed computational studies of small (solid) particle behaviour in a truck turbo compressor [37]. The results suggested that local erosion rates are highly depen-

dent on impact speed, showing a correlation between higher speeds and more erosion. This study used Tabakoff & Hamed's erosion equation (given as Eq. 2.20 here), and noted that the impingement angles in the regions of highest erosion were moderate ( $20-25^\circ$ ). It was also noted that particles bounced off the shroud walls as the intake became narrower leading up to the inducer [37].

### 2.5.10 Liquid Impingement Erosion Mitigation

Mechanisms to mitigate liquid impingement erosion effects are divided into design or material measures. Material considerations include covering walls and blades with special coatings or changing the material altogether to something more durable. Design measures to combat erosion include altering the flow path of the carrying medium, changing the geometry of the flow channel to direct or break up droplets, and any other way to decrease the amount, speed or size of liquid droplets impinging on the affected surfaces [38].

Different methods are employed to reduce the LIE in turbo compressors. Control strategies can be employed to ensure that the exhaust gas recirculated is of a high enough temperature to avoid condensation and harmful droplet formation before the compressor. Condensate can be somehow collected and re-introduced to the engine downstream of the compressor. Compressor blades can be coated with special paint that is more erosion-resistant than the typical aluminium used for the turbo impellers. Suggestions of such mechanisms have been outlined by turbo manufacturers [13, 36, 39].

As mentioned, this work is about the analysis and improvement of a way of feeding liquid droplets closer to the centre of the compressor, where reducing impact velocity because of lower blade speed should reduce erosion. This in itself has been done before, e.g. by what is described and patented in a U.S. patent [39] and on online forums by automobile enthusiasts [40, 41].

## 2.6 Computational Fluid Dynamics

Computational Fluid Dynamics is a collective name for when computational power is used with numerical methods to calculate the behaviour of fluids. Often a commercial software is used where the users themselves do not need to formulate the differential equations to be solved, but need to set up the correct models and inputs to evaluate their specific case. The objective is to resolve the flow to gain information about the velocities, temperatures, pressures, mass flows etc. for a certain design of component. These CFD simulations can then be used to suggest and/or develop design changes to attain certain objectives. In this case, CFD simulations will be used to aid development of an intake design with higher resistance to liquid erosion.

### 2.6.1 General

At the core of computational fluid dynamics, the so-called Navier-Stokes equations describe the transport and conservation of momentum, energy and mass throughout the fluid body. This work relies on the numerical solvers provided by commercial software Star-CCM+ and do not modify the transport equations. Interested readers are referred to e.g. Andersson [42] for the explicit formulation of these equations. When setting up a CFD problem, the following steps need to be fulfilled:

**Geometry** There needs to be a digital rendition of the object being studied.

**Mesh** The fluid domain needs to be discretized in a way appropriate for the physics involved.

**Models** Models need to be selected to correctly incorporate the desired flow physics. Boundary and initial conditions need to be identified and set.

**Solution** The numerical solvers need to be chosen and run, and appropriate criteria for convergence need to be identified and attained.

**Validation/Verification** Analysis of the results needs to be performed, in order to identify what parts of the solution are reliable and what parts are unreliable or unphysical, and why. Have the models been successful in capturing the physics of the flow?

### 2.6.2 $y+$ Wall Refinement

One important quantity that is brought up when assessing mesh quality for a given problem is the  $y+$  value of the cells nearest to the walls. It is defined as follows:

$$y+ = \frac{yu^*}{\nu} \quad (2.21)$$

where  $y$  is the normal distance from the wall,  $u^*$  is an estimation of the wall friction velocity  $u^* = \sqrt{\tau_w/\rho}$ , where  $\tau$  is the wall shear stress in  $\text{kg/ms}^2$ , and  $\rho$  is the fluid density ( $\text{kg/m}^3$ ). The denominator  $\nu$  is the fluid's kinematic viscosity, defined as  $\nu = \mu/\rho$  ( $\text{m}^2/\text{s}$ ) where  $\mu$  is the dynamic viscosity ( $\text{Pas} = \text{kg/ms}$ ). The choice of different models for the treatment of the flow near walls warrant the use of different  $y+$  values. Solutions where the flow near the wall is modeled using a logarithmic law demand  $y+ \approx 30-100$ , whereas more computationally expensive solutions seeking to explicitly resolve the boundary layer near the wall need a  $y+ \approx 1$  [42].

The use of different near wall models is exemplified in Fig. 2.8. For a  $y+$  value below 5 it is common to resolve the flow velocity using  $U_{norm} = y+$ , where in this case the flow velocity  $U$  is made dimensionless according to  $U_{norm} = U/u^*$ . In the range of approximately  $5 < y+ < 30$  neither complete resolution of the wall nor the logarithmic

law are said to be valid enough. This region of  $y+$  values should be avoided. For  $y+ > 30$  the logarithmic wall law is generally considered valid.

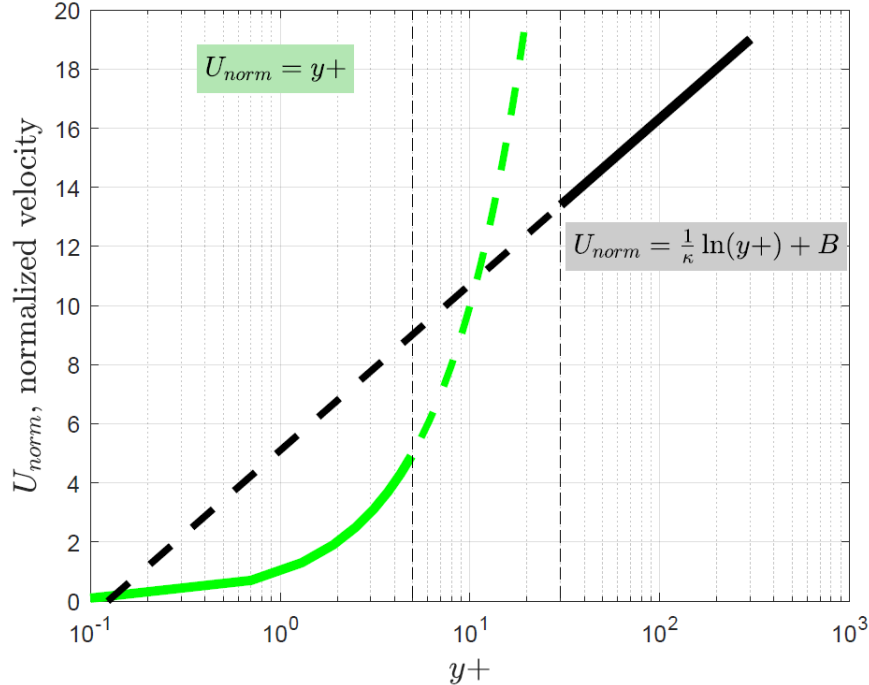


**Figure 2.8:** A graphic illustrating use of different near-wall models for different  $y+$  spans. Solid lines represent where the models are considered to be good enough. The middle region or so-called buffer layer is not captured well by either of the models. Figure generated from equations and values in [42].

### 2.6.3 CFD for Erosion

In order to make a detailed investigation of liquid impingement erosion using computational fluid dynamics, one would need to set up a multiphase flow problem, i.e. define a flow problem including not only the bulk gas flow but also the droplets as a discrete/dispersed phase co-existing with the bulk continuous gas flow. This is computationally much more expensive than one-phase flow. Introduction of a new species into the fluid creates the need for a multitude of new assumptions and simplifications. When it comes to small droplets, questions immediately arise as to droplet size, break-up and coalescence, evaporation and condensation, rebound and others.

Important aspects for the modelling of two-phase flow are: volume fraction of dispersed phase to bulk phase, particle size and shape, the forces acting upon the particles, and much more. Once the behaviour of the particles in the flow is determined, an investigation into the erosive potential of these particles would need a fluid-solid interaction

coupling to take into account the impact force and mechanical effect of dispersed phase onto a surface in question.

The present work predominantly uses one-phase flow and certain simple, robust correlations and relationships to get an idea of what kind of erosion can be expected in the cases studied. A first methodology for estimation of erosion potential for different turbo intake designs should perhaps not have to rely on an entire two-phase simulation to give some indication. This would be both time-consuming and too precise given the approximative input data about the droplet characteristics. Therefore, the focus of this study lies on formulating a conservative, robust and at the same time informative indicator of erosion potential.

### 2.6.4 Basic Multiphase Flow Theory

There are a few concepts central to multiphase theory which allow for categorisation of problems into typical cases. These typical cases each have their own toolbox which is most appropriate to apply for a valid solution. Identifying what flow regime applies to this case of droplets in low-pressure exhaust gas recirculation will help in taking the step from one-phase CFD calculations to two-phase.

#### Stokes Number

An important parameter in the choice of multiphase models is the Stokes number. It represents particle response time (particle relaxation time) compared to system response time:

$$St_T = \tau_d / \tau_c \quad (2.22)$$

where  $\tau_d$  is a time constant for the dispersed phase (for the droplets):

$$\tau_d = \frac{|\rho_d - \rho_c| d_d^2}{18\mu_c} \quad (2.23)$$

where  $\rho$  is the density of the dispersed ( $\rho_d$ ) and continuous ( $\rho_c$ ) phases,  $d_d$  is the characteristic diameter of the dispersed phase and  $\mu$  is the dynamic viscosity of the continuous phase [43]. The corresponding time constant for the system,  $\tau_c$ , can for turbomachinery applications be assumed to be the time for one blade passing. This can be found by:

$$\tau_c = \frac{2\pi}{Z\Omega} \quad (2.24)$$

where  $Z$  is the number of blades and  $\Omega$  is the rotational speed in rad/s. Another alternative for a characteristic time scale is:

$$\tau_c = \frac{L_c}{U_c} \quad (2.25)$$

where  $L_c$  is some characteristic length scale (such as the inducer diameter) and  $U_c$  is a characteristic velocity of the flow (e.g. the relative flow velocity).

If the Stokes number from Eq. 2.22 is much lower than 1, the particles in question will follow the continuous phase's behaviour closely, i.e. follow streamlines. If the Stokes number is much greater than 1, particles will ignore streamlines, be dominated by inertia and will follow along on whatever previous trajectory they had [43].

### Two-Phase Simulations for Erosion From The Literature

For radial turbines, Ghenaiet has found that particle trajectories related to Stokes numbers behaved according to the following: a Stokes number of 0.03 – 0.3 meant that particles would follow streamlines, whereas those with Stokes number 0.3 – 3 would impact the blades and the ones with Stokes numbers above 3 would behave altogether ballistically and ignore streamlines [44].

Brun et al. have made suggestions that entail performing one-way coupled, steady (i.e. not time-resolved) simulations of two-phase flow with particles for turbomachinery, and then using functional relationships relating the resolved forces to each other to determine where and which particles are most likely to impact blades, and which of them are likely to follow the gas flow [45].

### Multiphase Models

Adapting chosen models to suit the case at hand are a large part of a multiphase solution. Without going too deeply into the subject, it is worthwhile knowing that Lagrangian Particle Tracking is a multiphase solving technique which assumes that the dispersed phase makes up a very low fraction of the total flow (as in mass and volume fraction). Individual particles or parcels of similar particles are tracked through the velocity fields and the forces acting upon them are calculated [43].

# 3

## Method

This chapter describes the method used to achieve the desired goal of providing a liquid impingement erosion methodology which aims to suggest improved compressor intake design for this application. The turbo compressor used is introduced, and the problem at hand is specified in terms of CFD framework. The chosen models of liquid impingement erosion are concretized and adapted for use within this task, based on both a theoretical and experimental foundation.

This thesis work aims to incorporate several different areas: commercial software for flow simulation, experimental results for one operating case, and theoretical models of erosion. The aim is to use these tools to suggest an improved nozzle design for erosion resistance for the turbo compressor. The hypothesis is that a higher erosion resistance will be found for the intake pipe with the central nozzle than for the standard intake pipe.

In order to systematically approach this task, a workflow for the project has been outlined together with Volvo Trucks:

- a. Set up CFD simulation of the air flow through the standard turbo compressor (intake configuration 1).
- b. Incorporate the central nozzle (intake configuration 2) into the simulation model determined in a.) of the main compressor intake flow.
- c. Perform and compare simulations for both case a.) and b.) for a given operating point suggested by Volvo Trucks for the low pressure exhaust gas recirculation case of interest.
- d. Using relevant scientific literature and engineering sense: suggest, implement and assess erosion models that can combine the one-phase flow results from c.) with an appropriate assumption for the droplet characteristics to predict erosion potential.
- e. Evaluate and quantify the rate of impact wear of the impeller for both intake configurations for the same mass flow rate of liquid water.
- f. Suggest a nozzle design that might eliminate erosion for this engine point.

### 3.1 The Turbo Compressor

This work has compared the liquid erosion susceptibility of two intake designs for the same turbo compressor: one design with a standard intake, the other including a central nozzle. The impeller and diffuser were the same in both cases. The volute, though not included in simulations, was also the same.

The compressor used for the CFD simulations case had an outlet diameter  $d = 85$  mm and an inlet diameter at 68% of this, i.e.  $d_{in} = 0.68 \cdot 85 = 57.8$  mm. It had 7 main blades and 7 splitters. A view of the impeller is given in Fig. 3.1. It was assumed to be made of aluminium alloy.

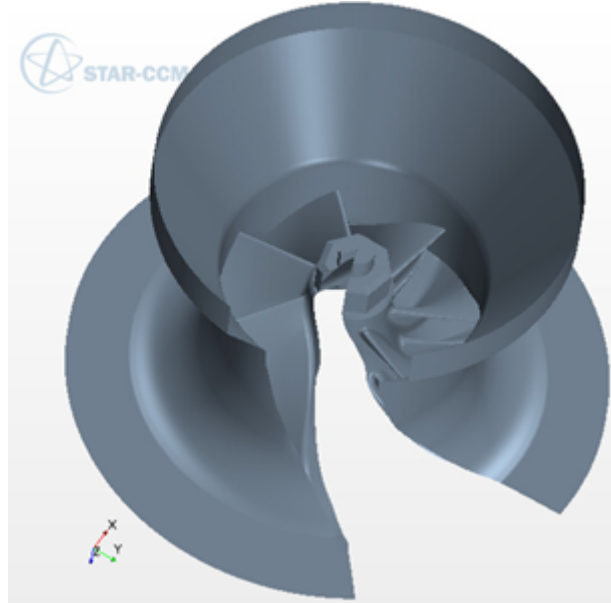


**Figure 3.1:** The impeller used in CFD calculations. One sector is omitted to give a better view of the inside.

The compressor used in the Volvo bench test was larger than the compressor to be used in simulations. The larger compressor had an outlet diameter  $d = 92$  mm and an inlet diameter at 67% of this, i.e.  $d_{in} = 0.67 \cdot 92 = 61.6$  mm. The discrepancies between experimental and simulated compressors, and their implications for calculations, are treated in Sections 3.2.2 and 3.2.3 below.

## 3.2 CFD Problem Definition

The CFD analysis was mainly performed in Star-CCM+ version 10.06.009. The Volvo computational cluster was used to perform CFD, reducing computational time substantially. In this section the methodology for the CFD case solution is outlined.

### 3.2.1 Progression of CFD Simulations

The CFD work was performed with cases of gradually increasing complexity. An outline of the different compressor operating points of interest and the cases investigated is presented below.

#### One-Phase

High Pressure Operational Point

Case I: Standard Intake

Medium Pressure Operational Point

Case II: Standard Intake

Low Pressure Operational Point (Bench Test Case)

Case III: Standard IntakeCase IV: Central Nozzle Intake**Two-Phase (simulation not included in this thesis work)**

Low Pressure Operational Point (Bench Test Case)

Case V: Central Nozzle Intake**3.2.2 Identifying Operational Points to Investigate**

When performing CFD calculations, it is vital to validate the results against previous experimental or theoretical results. The compressor map provided by Volvo gave an indication of the operational points of the compressor with respect to rotational speed, mass flow and pressure ratio. However the pressure ratio given by compressor maps is  $P_{03}/P_{01}$ , meaning the stagnation pressure rise from inlet to volute outlet. In the CFD cases the volute was omitted. Simulations were terminated at the diffuser outlet and give  $P_{02}/P_{01}$ . The different locations are shown in Fig. 3.2: diffuser outlet is point 2 and volute outlet is point 3. CFD calculated the pressure at diffuser outlet/volute inlet (pt. 2), and after this the engineering approximations described in Section 3.2.2 below were used to find the pressure at volute outlet (pt. 3).

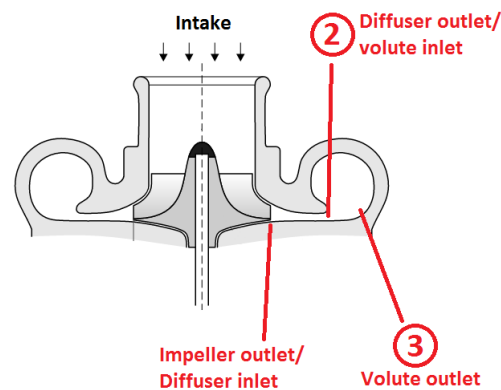


**Figure 3.2:** A cross-section through the turbo compressor.

### Matching Points in Compressor Map with Experiment and Simulation

It was necessary to relate the CFD-simulated pressure ratio ( $P_{02}/P_{01}$ ) to the one given in the compressor map ( $P_{03}/P_{01}$ ), as the latter was used for validation. For this, Volvo's experience in turbochargers was used: with the help of the simulated diffuser outlet stagnation and static pressures, and an estimate of the typical recovery of dynamic pressure to static pressure in the volute, an approximation was made of the outlet pressure from the volute,  $P_{03}$ , that would be expected for each case.

The dynamic pressure at diffuser outlet was found as the difference between the total and static pressure at diffuser outlet. Here, the total pressure was a result of the CFD simulation and the static pressure was set as a boundary condition. Hence:

$$P_{\text{dyn},2} = P_{02} - P_2 \quad (3.1)$$

and the following engineering estimate for the static pressure at volute outlet was used:

$$P_3 = P_2 + 0.44P_{\text{dyn},2} \quad (3.2)$$

Then, this information was used together with compressible flow relations to find the total pressure at volute outlet. Derived in Appendix A and relating volute outlet total pressure to properties at the diffuser outlet, Eq. A.13 was applied in the following way:

$$P_{03} = P_3 \left( \frac{1}{2} + \sqrt{\frac{1}{4} + \frac{\gamma - 1}{2\gamma} \left( \frac{\dot{m}}{P_3 A} \right)^2 R T_{02}} \right)^{\frac{\gamma}{\gamma - 1}} \quad (3.3)$$

Here  $P_{03}$  represents the stagnation pressure at volute exit, which was found using the static pressure at the volute exit  $P_3$  (calculated from Eq. 3.2), as well as the mass flow  $\dot{m}$  and the area  $A$  at volute outlet. The diffusion process in the volute was assumed to be adiabatic (commonly done in turbomachinery calculations) [7], meaning the volute total temperature  $T_{03} = T_{02}$ . The outlet volute area  $A$  was calculated as a disc with diameter 52 mm, meaning that  $A = \pi(0.052)^2 = 2124 \text{ mm}^2 = 2.124 \cdot 10^{-3} \text{ m}^2$ .

A back-of-the-envelope check of the feasibility of the volute outlet pressures was done by calculating the total-to-total efficiency for the different CFD cases according to Eq. 2.6 and comparing them to the compressor map in Fig. 3.3.

### Compressor Map: Identifying Operating Point Corresponding to Test Point

Physical experiments on a turbo compressor with a new nozzle had been performed at Volvo's test facility in Malmö prior to the commencement of this work. The tests had been performed for an engine operating point which exhibited a high rate of condensation of water for exhaust gas recirculation.

In order to gain some knowledge on the reliability of the one-phase CFD calculations, simulations were performed for three different operational points, of which one matched the operational point run in the Volvo test rig. Three compressor working points were simulated to ensure that the flow behaviour agreed with what would be expected of the different points.

Figure 3.3 shows a compressor map corresponding to the geometry of the compressor used for calculations. The green and blue locations marked "X" were the ones chosen for simulations. The upper two points (Cases I and II) were simulated to see that the models and settings chosen in Star-CCM+ gave results that corresponded to similar calculations performed earlier at Volvo, as well as what would be expected from the compressor map.

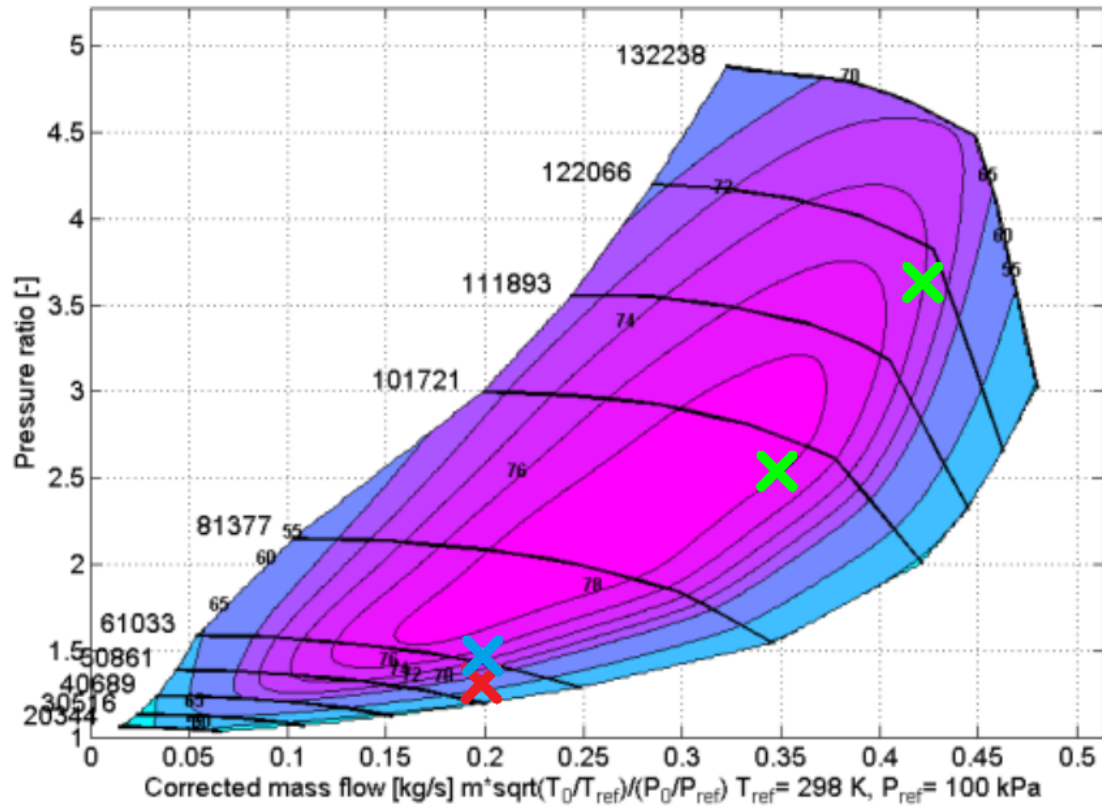


**Figure 3.3:** This compressor map corresponds to a large degree with the compressor used in the computational parts of this work. The different crosses marked X show the different operating points of interest here. The green points correspond to Case I and II (pure simulations), whereas the red point marks the characteristics for the bench test. The blue X marks the point for simulations of Cases III and IV.

The lower left point (Cases III-IV) was intended to correspond to the point run in the test rig. However, the actual compressor used in the test rig was of a larger diameter than the one for which the CAD (digital) geometry was available. Hence, the physical experimental compressor achieved the desired mass flow and pressure ratio at a lower rotational speed than the virtual one. Therefore, the simulated compressor's rotational speed was adjusted upward to be able to deliver the desired flow and pressure rise desired. How this was done is described below.

### Correction of Rotational Speed for Different Compressor Diameter

In order to have a first approximation of what the new rotational speed might be, the relationship outlined in Section 2.1.3 was used, inserting values of  $D_a = 92$  mm

for the physical test compressor and  $D_b = 85$  mm for the virtual CFD compressor. The rotational speed for the compressor in the physical test was approximately  $N_a = 53200$  rpm, giving:

$$N_b = N_a \frac{D_a^3}{D_b^3} \Rightarrow N_b = N_a \frac{92^3}{85^3} \Rightarrow N_b = 53200 \frac{778688}{614125} \approx 66200 \text{ rpm} \quad (3.4)$$

This indicated that the rotational speed for the smaller CFD compressor needed to be higher than what was given in the bench test data for the larger compressor.

In the compressor map in Fig. 3.3, the red X represents mass flow and rotational speed for the turbo used in Volvo's engine test (one with a larger diameter). Using those specifications in the CFD calculations gave a pressure rise that was lower than necessary. Therefore, this point was shifted up (higher rotational speed) to achieve correct pressure ratio for current mass flow. This simulated operating case is represented by the blue point.

### Choosing Mass Flow Conditions For Cases III-IV

The other quantity necessary to find the correct operational point is mass flow. Mass flow can often be difficult to accurately measure for low flows, but Volvo did provide data from the bench test.

According to the experimental data, the air flow into the compressor was  $\text{Flw\_InletAir} = 0.1663$  kg/s, and the exhaust gas flow was  $\text{Flw\_EGR} = 0.0317$  kg/s. The total mass flow into the compressor was thus  $\text{Flw\_Tot} = \text{Flw\_InletAir} + \text{Flw\_EGR} = 0.198$  kg/s. This gave an EGR percentage of  $0.0317/0.198 = 16\%$ , which is also what is given explicitly in the test data.

For Cases III-IV, all exhaust flow was sent through the central nozzle and all intake air through the main pipe, which corresponded to the actual engine design.

### Amount of Water in Intake Gas

For the case tested in the rig, the fuel flow was 6.055 g DME/s, which would give 7.1 g  $\text{H}_2\text{O}$ /s when fully combusted according to the stoichiometry outlined in Section 2.4.3.

Other information on the moisture levels available from the test was an air humidity of 76%. Using a psychrometric chart (can readily be found online [46]), the water fraction in the air was found to be:  $x_{\text{H}_2\text{O}} = 0.0085$  kg  $\text{H}_2\text{O}$ /kg air for the 16 °C outdoor air. This, combined with the known mass flow  $\dot{m} = 0.166$  kg/s of air taken in to the engine, gave:

$$\dot{m}_{\text{H}_2\text{O}} = \dot{m} x_{\text{H}_2\text{O}} = 0.166 \cdot 0.0085 = 0.986 \text{ g H}_2\text{O/s} \quad (3.5)$$

Combining these two sources of water in the exhaust gas, the water content totaled approximately 8 g H<sub>2</sub>O/s. In the experimental case, the rate of exhaust gas recirculation into the turbo compressor was given as 16%, meaning 16% of the maximum of 7.1 g H<sub>2</sub>O/s was received from the products of a complete combustion for the given fuel amount. Hence, the total water mass flow was written as:

$$\dot{m}_{\text{H}_2\text{O}} = 0.16 \cdot 7.1 + 0.986 = 2.12 \text{ g H}_2\text{O/s} \quad (3.6)$$

### 3.2.3 Geometry and Simplifications

The turbo compressor digital geometry was provided by Volvo in ParaSolid format (.xt). This was imported into Star-CCM+ where the Surface Repair function was used to make sure there were no apparent defects on the surfaces. Views of the imported geometries can be seen in Fig. 3.4, where both the standard intake and the intake with the new nozzle are shown.

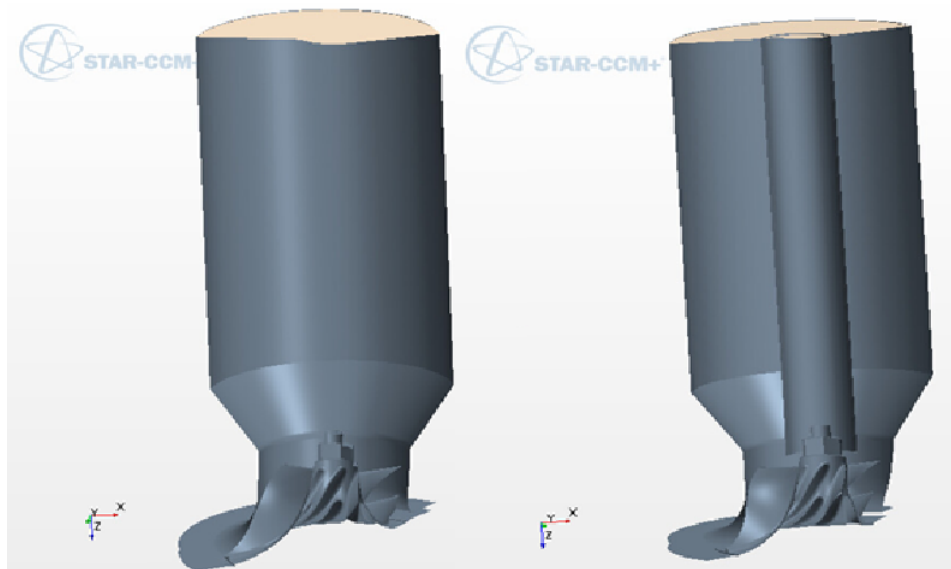


**Figure 3.4:** A view of intake, impeller and diffuser for the standard turbo design (left) and the design including the central nozzle (right).

For the purpose of this master thesis, certain simplifications were made in order to speed up meshing and simulations. These are outlined below.

#### Ported shroud neglected

In both CFD geometries, the turbo compressor intake lacked a so-called ported shroud. A ported shroud is an intake modification that effectively widens the compressor operating

range (i.e. widens the region with ellipses in a compressor map such as Fig. 2.4). An example of a compressor with a ported shroud is shown to the right in Fig. 3.5. By comparing the turbo compressors shown in Fig. 3.5 it is possible to see the omittance of the channel on the periphery around the circumference of the normal main intake pipe. A ported shroud is generally present in modern engines, but as it would have made the geometry more complex it was omitted from this study.



**Figure 3.5:** Comparison of turbocharger with and without ported shroud. The plain inlet is to the left and the ported shroud is to the right. Picture found online [47].

### Inlet straightened and lengthened

In an actual truck configuration, a lack of space often means that many bends and turns in the pipes are necessary to fit into the installation space. In both CFD cases, the inlet length used in the simulation was much longer and straighter than it is in reality. This was done because, for computational purposes, it is sensible to have an inlet length several times longer than the the pipe inlet diameter [42] in order to allow the flow to develop completely before it encounters the obstacles of interest in the domain. If the inlet is too short, inlet effects set by the boundary and initial conditions may affect the flow characteristics at critical areas in unrealistic ways, obscuring the most relevant effects.

### Periodicity of impeller utilised

In order to save a considerable amount of computational time, only one-seventh of the geometry was actually modelled in the software. Periodic interfaces were set on the sector sides, as shown in Fig. 3.6 where a sector view is given both as standalone and repeated. The assumption of such periodicity is common practice in turbomachinery applications, and from it follows the assumption of an identical blade and splitter geometry for the full compressor.

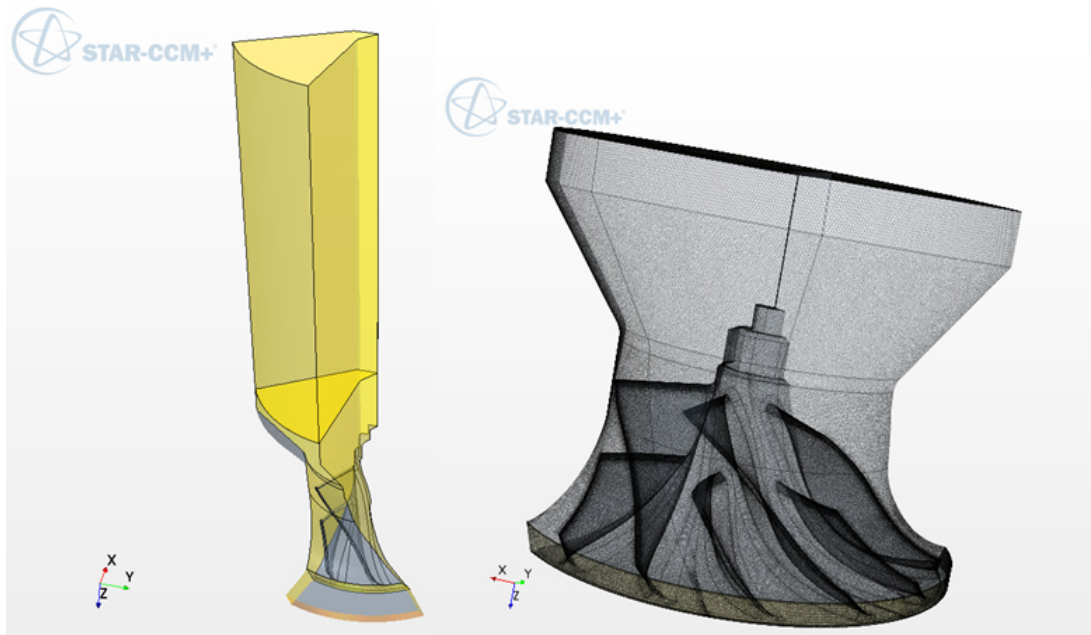


**Figure 3.6:** One-seventh of the geometry and a view resembling the periodic repetitions of the impeller region.

### Volute omitted

The volute, or scroll, was not included in this analysis as it was not considered an area of interest from an erosion point of view. It would have increased the mesh size of the computational domain without increasing the relevance of the results. The outlet pressure was thus calculated by CFD only up to the diffuser outlet. This was then used to estimate an outlet pressure at the volute. Such a calculation was necessary in order to at least approximately identify where the simulated points were in the compressor map, as compressor maps give information for the *full compressor*, from intake to volute outlet. See Section 3.2.2 and, if necessary, the derivation in Appendix A for details.

### Mounting for Central Tube Ignored

The bench test (real) compressor also featured a fastening mechanism for the central nozzle, which has been neglected in the calculations, but may have resembled Fig. 3.7 [40].



**Figure 3.7:** Possible three-pin design for fastening a central nozzle into the main intake pipe. Note that this is not the actual compressor studied in this thesis, but merely an example of a fastening mechanism.

The mechanism by which the central tube is fastened in place inside the main intake tube was not included in the geometry. The decision was made that any disturbance in the flow field that the chosen fastening mechanism causes would not be long-lived enough to affect the flow at the blades.

### Cylindrical Volume Removed at Centre

To avoid numerical difficulty at the singular tip of the sector where the two periodic sector surfaces meet, a small cylindrical volume along the  $z$  axis was subtracted from the geometry at the very tip of the triangular sector, see Fig. 3.8. This enabled turbo-specific post-processing in Star-CCM+ and made meshing less demanding. Boundary conditions for this surface were set for the least interference with the flow. Details on this can be found in Section 3.2.6.

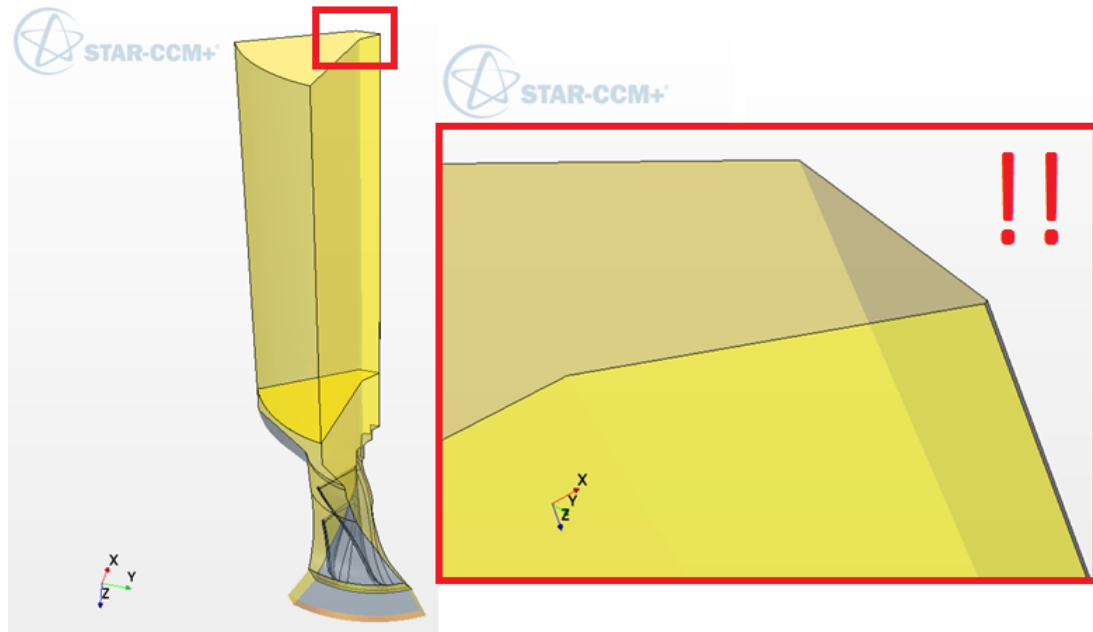
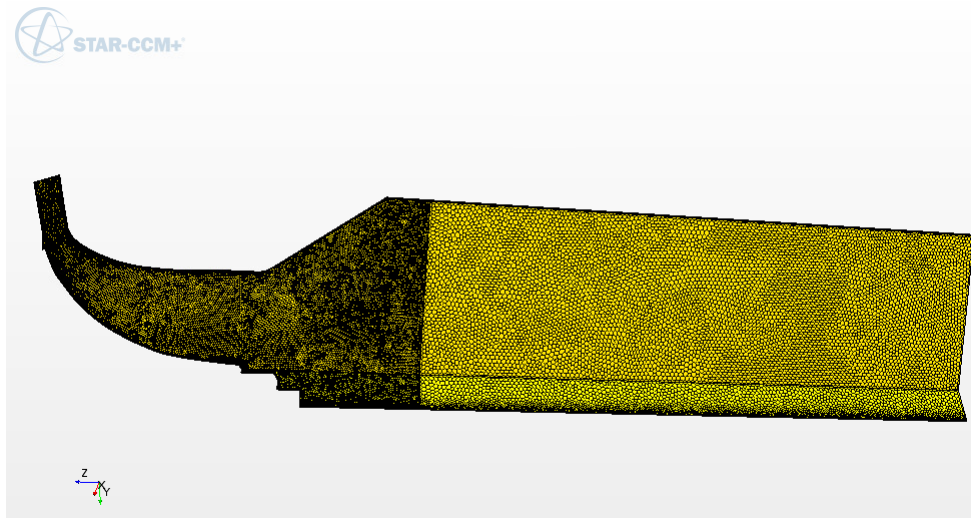


**Figure 3.8:** Illustrating the cylindrical volume cut out from the tip of the sector.

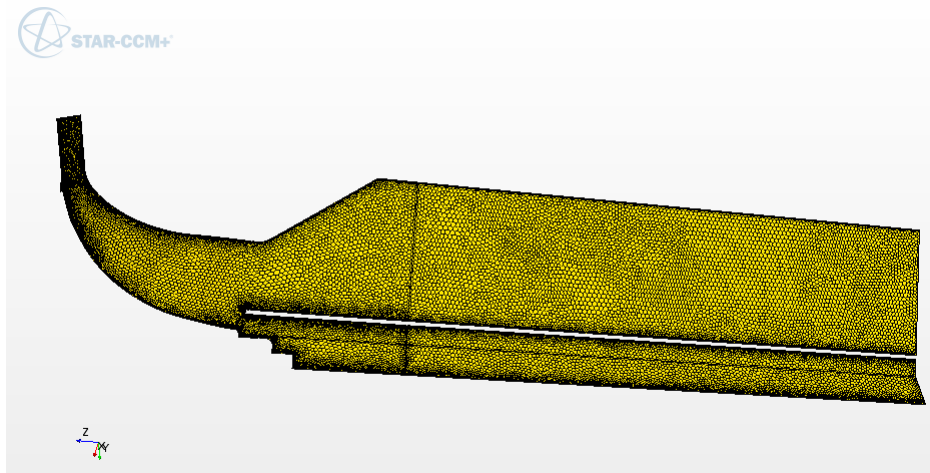
### 3.2.4 Mesh Models

For flows through blade passages in turbomachinery, hexahedral structured meshes are often preferred for their accuracy and the low number of elements needed.

For this project however, it was discovered that the complexity of the geometry involved, as well as issues with software compatibility, meant that a hexahedral mesh would not be possible to achieve in an acceptable amount of time for both the standard compressor configuration and the new configuration with the central nozzle. Therefore, the automatic mesher function in Star-CCM+ was used: it combines polyhedral cells in the bulk of the flow with prism (hexahedral) cells near walls. Overall views of the two resulting meshes for the cases with and without central nozzle are given in Fig. 3.9. Specifications in Star-CCM+ regarding the base mesh size and relative sizes of mesh cells were kept as similar as possible for the two cases. The number of cells for the different parts of the geometry for both standard intake and central nozzle intake are shown in Table 3.1.



(a) Standard intake case.



(b) Case with central nozzle.

**Figure 3.9:** Cross-section of the meshes used for the two cases. View between blade and splitter.

Mesh parameters and refinement were performed with the help of Volvo turbo experts: a finer mesh was used closer to regions of large velocity gradients such as at tip clearance, and relative cell growth for adjacent cells was limited in order to promote numerical accuracy. A cross-section of the mesh through the impeller for the standard intake case can be seen in Fig. 3.10. A view from the impeller outlet is given in Fig. 3.11, where the yellow surfaces mark the surfaces set as periodic in the simulation.

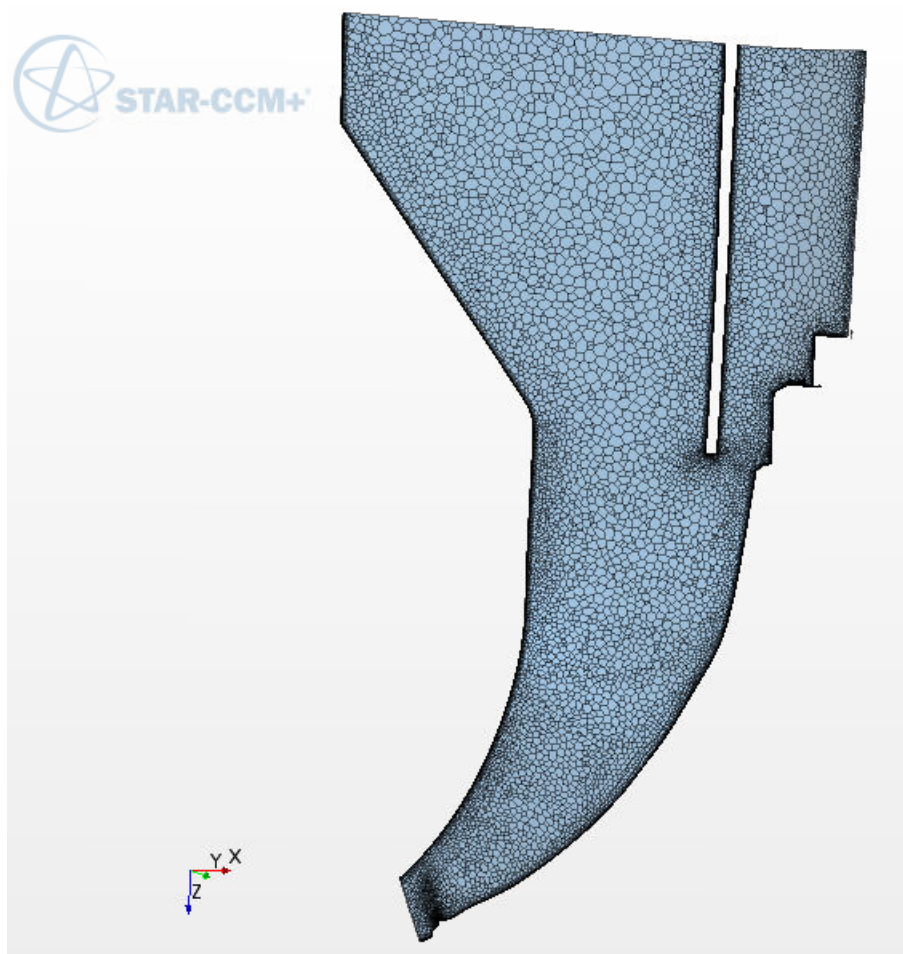


**Figure 3.10:** A meridional cross-cut of the mesh throughout the impeller fluid volume. Note the denser (darker) mesh closer to the walls and the coarser mesh in the free-stream main intake pipe.

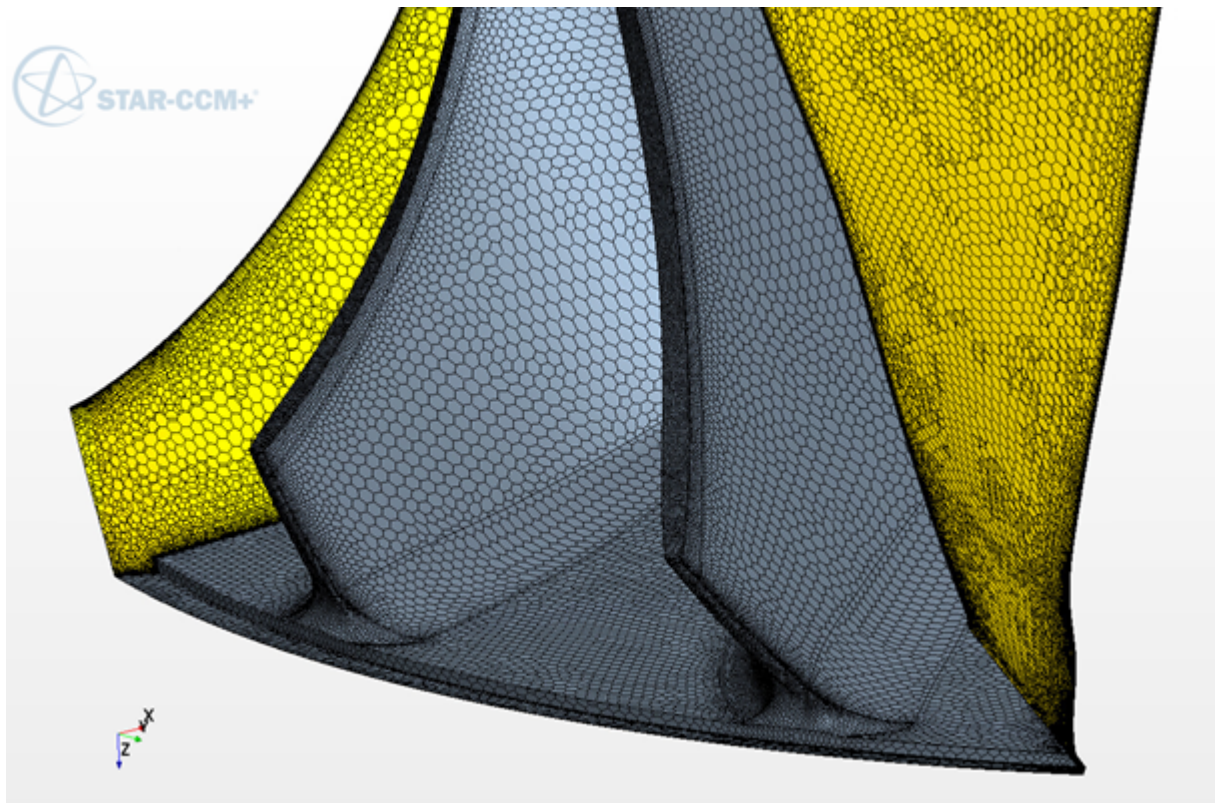


**Figure 3.11:** Mesh view from impeller outlet. Areas of mesh refinement are shown e.g. towards the blade tips and the trailing edges. Yellow surfaces are periodic, showing the overlapping of the periodic mesh.

**Table 3.1:** Number of cells in the different parts of the computational meshes used for the one-phase CFD calculations.

Number of Cells	Diffuser	Impeller	Inlet	Total
Standard Configuration	196664	1763785	181340	2141789
Central Nozzle Configuration	196664	1777815	390411	2364890

### 3.2.5 General Flow Models

The solution settings chosen in Star-CCM+ for this problem were:

- ★ Coupled energy
- ★ Coupled flow (2nd order discretization)
- ★ Implicit solver
- ★ Steady simulation
- ★ Three dimensional
- ★ Turbulent
- ★ Air properties: Sutherland’s law for dynamic viscosity, thermal conductivity. Constant molecular weight. Specific heat as polynomial in  $T$ . Compressible ideal gas.
- ★ Reynolds-Averaged Navier-Stokes (RANS)
- ★ SST (Menter)  $k$ - $\omega$  turbulence (2nd order discretization)

### 3.2.6 Wall Treatment

In order to appropriately discretize the wall layer of the fluid body, ten prism layers were set closest to the wall. Their total thickness was defined as 33% of the base size of the mesh (i.e.  $3.3 \cdot 10^{-4}$  m), and the increase in size of neighbouring prisms was set to 1.5. See Fig. 3.12 for a close-up of such prism layers. Star-CCM+ uses an “All  $y+$  Treatment” model where it automatically resolves the boundary layer when the  $y+$  is low enough, and applies the equilibrium wall law where  $y+$  is too high to resolve [48].

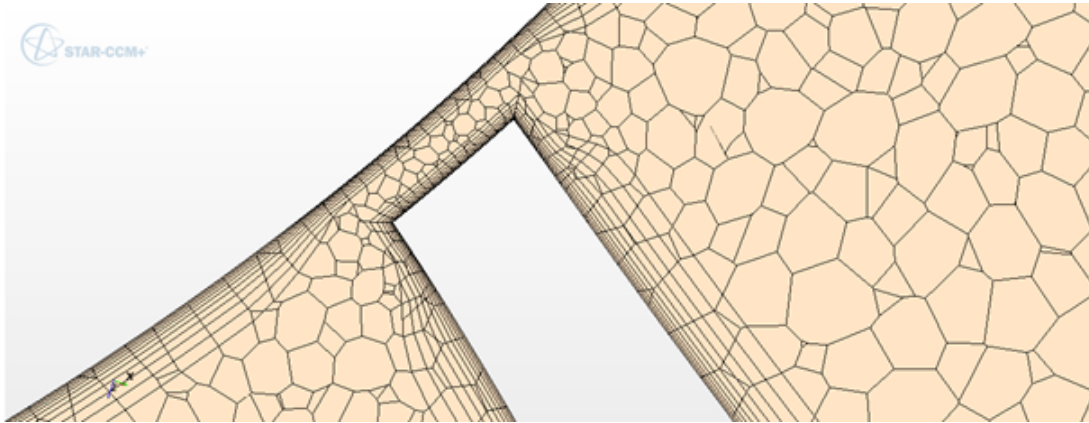


**Figure 3.12:** Mesh cross-section showing prism layers near shroud and around the blade tip.

The wall boundary conditions as defined in Star-CCM+ were:

- ★ No-slip condition
- ★ Adiabatic
- ★ Smooth wall
- ★ Blended wall function

The exception to this wall treatment was the cylindrical volume mentioned in Section 3.2.3: it was set as a “Symmetry plane”, which caused the least disturbance to the flow at its boundary. This kind of boundary condition can be seen as the opposite to a no-slip condition, i.e. completely frictionless.

### 3.2.7 Turbulence Modelling

In a compressor, an adverse pressure gradient is caused by the pressurised flow downstream tending to return to the region of lower pressure where it came from. This phenomenon is best captured by the  $k-\omega$  turbulence model [42]. However, the  $k-\omega$  model is notorious for overpredicting free-stream turbulence. The Menter’s SST  $k-\omega$  model was therefore chosen as a trade-off [49].

### 3.2.8 Impeller Rotation Modelling

In order to be able to incorporate the rotation of the impeller region, a rotating reference frame was used in Star-CCM+. The impeller was set at a standstill in its own reference frame, while the reference frame rotated. The whole of the impeller region was set to this rotating reference frame except the following: shroud, hub cavity (between hub rim

and diffuser), and – for Cases III and IV – the central nozzle. Rotation was defined as around the positive  $z$  axis.

### 3.2.9 Solution Methodology and Convergence Criteria

When attempting to simulate a certain point in the compressor map, the following procedure was followed:

- ★ Set the rotational speed and mass flow at inlet according to compressor map point.
- ★ Guess and set an appropriate static pressure at diffuser outlet.
- ★ Run simulation and keep track of the static pressure at impeller inlet.
- ★ Adjust the set static pressure at diffuser outlet until the inlet static pressure is approximately 97 kPa.

The static pressure as boundary condition was an initial guess, but as the simulation converged toward finding an inlet static pressure, this guessed outlet pressure was adjusted to make sure the correct inlet pressure was achieved.

Due to the non-experimental nature of two of the operational points run using CFD Cases I and II, and the compressor in the test bench case being different from the provided geometry for Cases III and IV, some leeway was granted around landing at the exact operating points in the compressor map. A solution was considered converged when the following is fulfilled:

- ★ Mass flow throughout the domain has reached and stabilised at the expected value.
- ★ Pressures at inlet and outlet have reached their asymptotic values.
- ★ Temperatures at inlet and outlet have reached their asymptotic values.
- ★ Residuals are stable and below a given convergence value (preferably below  $1 \cdot 10^{-4}$ ).

The term “asymptotic value” here means that the quantity in question does not vary from one iteration to the next. Because of convergence difficulty for certain cases, no formal convergence criteria was set in the software. Instead, qualified assessments of the residuals and monitoring of vital quantities in communication with Volvo Powertrain were used to determine convergence. More about this can be seen in Section 5.1.4.

Cases I and II in Fig. 3.3 were not validated against experimental tests but against similar simulations run by Volvo experts. The pressures and mass flows achieved were compared to compressor map points.

The operational point of Cases III and IV corresponded to the experiment conducted on the central nozzle design by Volvo, and was validated by the solver finding a solution that on the whole corresponded to the measured quantities.

### 3.2.10 Boundary and Initial Conditions

The vitally important boundary and initial conditions set in the simulations are listed and described below.

#### Boundary Conditions

- Mass flow set at inlet, static pressure set at diffuser outlet.
- Periodic boundary conditions set at the sides of the sector slice <sup>1</sup>.

#### Initial Conditions at Inlet

- Turbulent velocity scale: 1 m/s
- Gas velocity: (0,0,25) m/s (purely axial)
- Internal interfaces were set between inlet/impeller and impeller/diffuser.

#### Initial Conditions over Whole Domain

- Static temperature: 298 K
- Turbulence intensity: 5%
- Velocity: (1.0, 1.0, 1.0) m/s
- Turbulent viscosity ratio: 100

The simulations were run initially with first order accuracy and with the desired diffuser outlet pressure set to the whole fluid domain. This was done for improved solver stability, and meant that the initial values of pressure, mass flow etc. were very different from their converged values. The solver gradually worked its way down and stabilised at the correct mass flow. Such a far-off guess substitutes an investigation of initial condition dependence of solution. When a first order accurate flow field was obtained, the simulation was switched to second order.

A compilation of parameters set in Star-CCM+ for Cases III-IV can be found in Table 3.2.

### **Water in Recirculated Exhaust Gases: Implications for Two-Phase Simulations**

Knowing the intake air and exhaust gas mass flow, worst-case calculations were performed for the amount of water in the mixture as outlined in Section 2.4.3. By assuming that all the moisture in the recirculated exhaust gases was condensed, a conservative approach was ensured.

---

<sup>1</sup>Star-CCM+ automatically calculated these to approximately 51.4286 degrees rotation.

**Table 3.2:** The conditions set in Star-CCM+ for the operating points representing Case III (without central nozzle) and Case IV (with central nozzle).

CFD Setup	Case III	Case IV
Mass flow total (kg/s)	0.19788	0.19788
Mass flow set (kg/s)	0.02827	$0.0237428 + 0.00452571 = 0.02827$
Static pressure diffuser outlet (Pa)	135000	135000
Static temperature diffuser outlet (K)	343	343
Rotational speed (rpm)	62500	62500
Pressure ratio $P_{03}/P_{01}$ from map	1.517	1.517

For this calculation the density of air was taken as  $\rho_g = 1.2 \text{ kg/m}^3$  and the density of water as  $\rho_w = 10^3 \text{ kg/m}^3$ . The maximum mass flow of water in the exhaust gas according to specifications in the test case, as calculated in Section 2.4.3, was  $2.12 \text{ g/s}$ . The mass fraction of water in the central intake pipe was thus equal to the maximum amount of water in the exhaust gas, divided by the total mass flow of exhaust gas.

According to Section 2.4.3, the amount of water that could be found in the intake pipe was  $2.12 \text{ g/s}$  while the EGR flow is  $0.0317 \text{ kg/s}$ , which gave a mass fraction of:

$$\text{massfrac} = \frac{2.12 \cdot 10^{-3}}{0.0317} = 0.0669 \approx 6.7\% \quad (3.7)$$

And the volume fraction became:

$$\text{volfrac} = \frac{\dot{v}_w}{\dot{v}_g} = \frac{\dot{m}_w/\rho_w}{\dot{m}_g/\rho_g} = \frac{2.12 \cdot 10^{-3}/10^3}{0.0317/1.2} = \frac{2.12 \cdot 10^{-6}}{0.0264} \approx 8 \cdot 10^{-5} \quad (3.8)$$

For the case with all exhaust gas being admitted through the central nozzle, both mass and volume fractions of liquid were low enough to warrant the use of Lagrangian particle tracking methods. For the case of a standard intake pipe, where all EGR is mixed with the main flow, the mass and volume fractions of water would be still lower.

The true size of the droplets was not known, meaning that any attempt at two-phase simulations would need to include assumption of a size distribution.

### 3.2.11 Two-Phase Modelling

In order to keep a two-phase simulation as simple as possible, the droplets were assumed to be spherical. Some suitable size distribution needed to be assumed, as no data was available. To begin with, a one-way coupling between gas and particles should be con-

sidered. The chosen setup would entail a guessed size distribution of non-interacting spherical particles.

As the gas temperature in the bench test was  $T < 35^\circ\text{C}$ , it was assumed that all moisture was condensed and that nothing evaporated. No distortion or break-up of droplets was considered.

The mass flow of water in the exhaust gas from Section 3.2.10 was used for a quick back-of-the-envelope calculation as to the number of particles. Assuming spherical droplets with radius  $r_p = 50 \cdot 10^{-6}$  m, the volume per particle became:

$$V_p = \frac{4\pi r_p^3}{3} = 5.236 \cdot 10^{-13} \text{ m}^3$$

The mass of one particle was found as  $m_p = V_p \rho_p = 5.236 \cdot 10^{-10}$  kg, where  $\rho_p = 1 \cdot 10^3$  kg/m<sup>3</sup> is the density of water. The droplets were assumed incompressible. Knowing the mass flow of condensate to be  $\dot{m}_w = 2.12 \cdot 10^{-3}$  kg/s, the number of particles in this specific mass flow was found as:

$$n_p = \dot{m}_w / m_p = \frac{2.12 \cdot 10^{-3}}{5.236 \cdot 10^{-10}} \approx 4 \cdot 10^6 \text{ per second} \quad (3.9)$$

which indicated 4 million droplets per second if they were 100  $\mu\text{m}$  in diameter each. Injecting these in groups (or more commonly, “parcels”) of 1000 droplets each meant 4000 parcels per second.

The method of running two-phase calculations would be to start from a one-phase solution, switch the solver to “unsteady” and inject particles at an appropriate rate. A multiphase setup of this kind would be an overlaying of two-phase models onto Case IV.

Using the calculations made here on the probable water content in the exhaust gases, a two-phase simulation could have been performed for the case with the tube for one droplet diameter size in order to try and see how many of the droplets impact the blades.

### 3.2.12 Grid Independence

A grid independence study was conducted to demonstrate the sensitivity of the solution to mesh refinement.

Eight different mesh sizes were used to compute the flow for Case IV (shown in the compressor map in Fig. 3.3). The case investigated was the geometry with the central nozzle included, as this was the more complex design. It was assumed that a mesh that is “fine enough” for this case would also be fine enough for the case without the tube.

The mesh size was varied using the parameter Base Size in Star-CCM+ under the node Continua/Mesh/Reference Values/Base Size. As the size of the computational cells was set relative to this base size, changing it effectively kept the same regions of refinement relative to the main mesh, but reduced the size of all cells. The following base sizes were investigated:  $5 \cdot 10^{-3}$  m,  $25 \cdot 10^{-4}$  m,  $2 \cdot 10^{-3}$  m,  $15 \cdot 10^{-4}$  m,  $1 \cdot 10^{-3}$  m,  $9 \cdot 10^{-4}$  m,  $8 \cdot 10^{-4}$  m and  $5 \cdot 10^{-4}$  m. A table showing the different amounts of cells involved in each case run for the grid independence study is shown in Appendix F.

The number of prism layers was kept constant, only the size of the total thickness of the prism layer was changed. This was changed relative to the base size which was, in its turn, kept at the base size defined as good enough by the mesh independence study. The prism layer stretching in the impeller was set to 1.5, meaning that adjacent prisms cannot differ more than 50% in width/thickness.

The total-to-total efficiency was calculated according to Eq. 2.6. The outlet pressure  $P_{02}$  was here taken to be the pressure at impeller outlet/diffuser inlet.

Because of different pressures in the central nozzle and the outer main intake pipe, a mass flow averaged value of these pressures was taken as  $P_{01}$ . This was calculated according to:

$$P_{01} = \frac{(\dot{m}_{big}P_{in,big} + \dot{m}_{small}P_{in,small})}{\dot{m}_{big} + \dot{m}_{small}} \quad (3.10)$$

where subscripts *big* and *small* represent the main intake pipe and the smaller nozzle, respectively. The two different pipes also had gases of different temperatures in reality. As a first estimation, a mixing process was assumed where enthalpy is conserved and the gases immediately find an appropriate mixing temperature  $T_{mix}$ . This was calculated according to:

$$T_{mix} = \frac{T_{EGR}\dot{m}_{EGR} + T_{air}\dot{m}_{air}}{\dot{m}_{EGR} + \dot{m}_{air}} \quad (3.11)$$

a short derivation of which is shown in Appendix J. The result was  $T_{mix} = 24^\circ\text{C}$ .

### 3.3 Liquid Impingement Erosion Analysis

A collection of relevant literature on erosion was studied in order to find models, correlations and formulae applicable to this problem. Suggestions for predictions of liquid impingement erosion were brought up. These predictions were compared to the results of the experimental case outlined by Karstadt et al. [36] described in Section 2.5.8 and presented in Table 2.1, as it was the only systematic experimental information on liquid impingement erosion presently available for a highly similar case. The aim was to find

a method for evaluating erosion potential that would give results analogous to the experimental results achieved in that study. Suggestions for such methods were identified and used to give an indication of the erosion potential for the Volvo test case with and without the central nozzle.

As the literature on LIE was gathered from different fields and uses different methods, a part of this work was to interpret and standardise the results of different studies to make them applicable to the Karstadt case and also eventually the actual Volvo case. This entailed many simplifications and adaptations.

In general, in calculations, worst-case assumptions and scenarios were assumed for unknown values. For example, no information was available as to the actual amount of water condensed in the Volvo bench test case. Therefore, all the water was assumed to be condensed before the gas reached the impeller. Such worst-case assumptions were to suggest a region of “safe operation” for high-condensate flows for the nozzle designs.

### 3.3.1 Making Use of Previous Experimental Work on LIE

Impact velocities for the different cases and diameters investigated in the Karstadt study were found as follows:

- The volume of the individual particles was calculated assuming spherical shape:  $V = 4\pi r^3/3$ . The number of droplets was then calculated knowing that for the different-diameter experiment, 5 litres were used in each case:

$$n_{droplets} = 5/V$$

- The time of the experiments was found by dividing the total litres by the flow rate:

$$t_{expts} = 5/\dot{Q}_{expts}$$

The numbers can be found in the study and are given in Appendix E for convenience.

- Droplets were assumed to travel with the flow (i.e. they have the same speed  $c$  as the carrying gas) before impacting the moving blades.
- Rotational speed in rad/s was found by using  $n$  in rpm as follows:  $\Omega = 2\pi/n60$ . The injection diameter was  $2/3$  of the blade length, which is why blade speed at impact was calculated as:

$$U = \Omega \frac{2}{3}r$$

- The idealised velocity triangles from Fig. 2.3 were used to find  $w$ :

$$w_{droplets} = \sqrt{c^2 + U^2}$$

which identified the supposed droplet impact velocity.

This was used in liquid impingement erosion models.

#### Using One-Phase Simulations For LIE Investigation

The one-phase simulations provided a velocity field for the Volvo bench test case with and without installed nozzle. The software provided a solution for all relevant flow properties in all mesh cells, such as: velocity, pressure, density, dynamic viscosity etc. Referring to Section 2.6.4, the only parameters needed from the discrete phase to determine the Stokes number were then particle density and particle diameter. The Stokes number was therefore calculated for a variety of different droplet sizes according to Eq. 2.22, and special attention was paid to the diameters actually tested in the experiment by Karstadt et al., namely: 153, 340, 470 and 1120  $\mu\text{m}$  [36]. The resulting Stokes numbers for Cases III and IV were then used to assess how likely droplets would be to ballistically hit the blades.

It was assumed that droplet slip velocity was zero just before the impeller, i.e. that droplets follow the gas path until they have approached the impeller blades. This is an assumption made by Karstadt et al. themselves [36]. A computational study by Khan and Wang also indicated that slip velocity for liquid particles approached zero as the particles traveled through the inlet [30]. The number of blades as used in Eq. 2.24 was  $Z = 7$ .

Numerical values for density and dynamic viscosity from the simulations were taken along the leading edge of the blade, between the outlet of the central nozzle and the blade surface. An illustration of where the samples were taken is shown in Fig. 3.13. Full values are given in Appendix I.

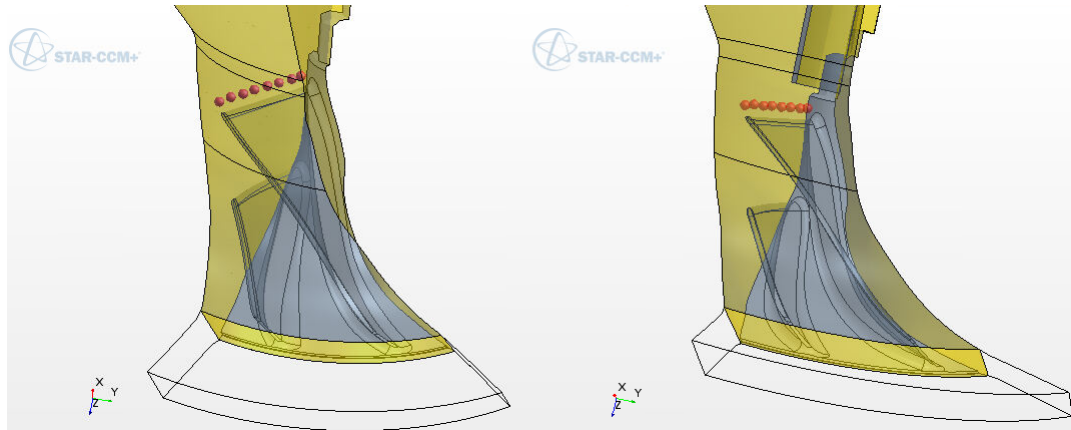
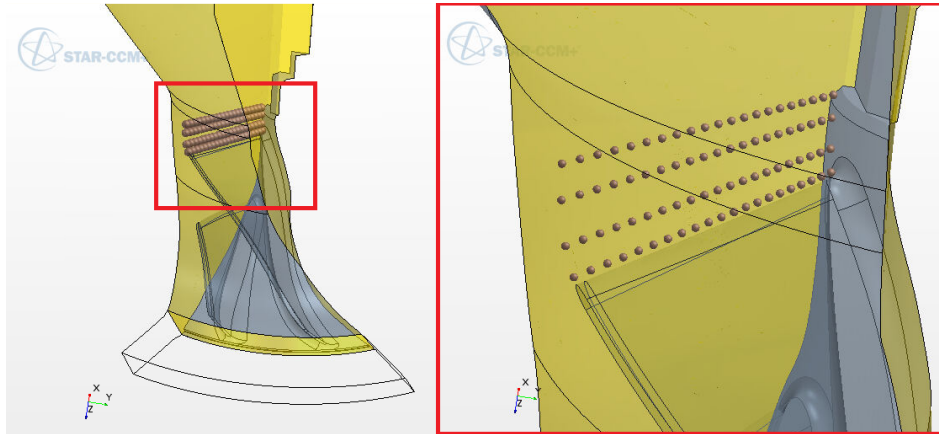


**Figure 3.13:** Illustrating the measurement positions used to determine values of local flow density and dynamic viscosity for the calculations of Stokes numbers for cases with and without the nozzle.

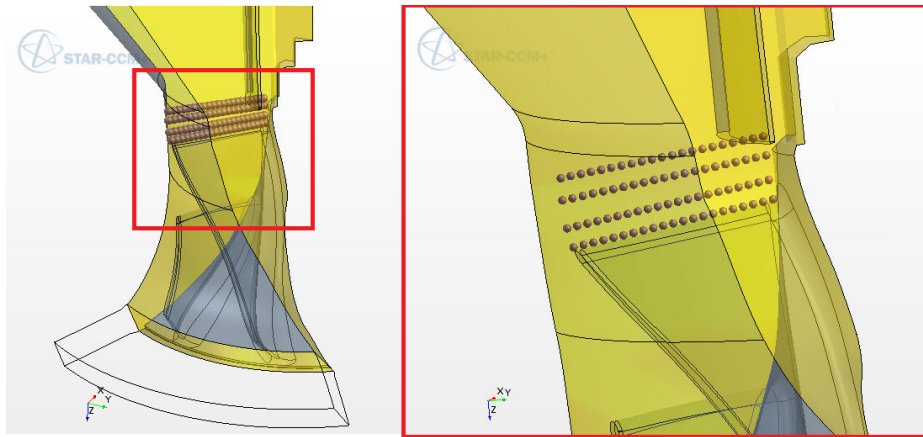
Supposed droplet impact velocities for the Volvo bench test case are taken as the relative velocities near blade leading edge calculated by CFD for Case III and Case IV.

### 3.3.2 LIE Dependence on Impact Velocity

The erosion caused for the rotational speed variation experiment in the Karstadt et al. study was compared to its calculated impact velocities from Section 3.3.1. A correspondence to an exponential development with increasing impact speed was investigated. For the Volvo bench test case, the worst-case (highest) relative velocities at blade vicinity were taken from CFD simulations of Case III and Case IV. The sample points for these velocities are shown in Fig. 3.14.



(a) Case III: standard intake case.



(b) Case IV: with the central nozzle installed.

**Figure 3.14:** Showing the location of measurement points for fluid velocities near the leading blade edge for Cases III and IV.

### 3.3.3 LIE Dependence on Droplet Size

To investigate this dependence, Karstadt et al diameters were used [36]. The agreement of erosion results from their experiment to an exponential erosion development with droplet diameter was checked.

As the effect of the tube on droplet size is unknown, it was not possible to perform a comparison of Cases III and IV based on this parameter.

### 3.3.4 LIE Relation to Cavitation Erosion

Relating liquid impingement erosion to cavitation erosion as suggested in Section 2.5.4 would require an established existing linear relationship for cavitation erosion that was not currently available.

The equilibrium cavitation bubble radius was found using Eq. 2.11 to determine what size of bubble could be accommodated in the droplets. This was done for both the Karstadt et al. experimental study, and CFD cases III and IV.

### 3.3.5 LIE Dependence on Both Impact Velocity and Droplet Diameter

For the Karstadt et al. experiment, the combination of droplet diameter  $d_3 = 470 \mu\text{m}$  and rotational speed  $n_1 = 50 \cdot 10^3 \text{ rpm}$  gave no observable erosion as given in Table 2.1. Erosion was first observed for  $n_2 = 100 \cdot 10^3 \text{ rpm}$  at this droplet diameter. Combining the impact velocity for the non-erosion-inducing rotational speed  $n_1 = 50 \cdot 10^3 \text{ rpm}$  with  $d_3$  gave a constant value  $\xi$  according to:

$$\xi = w_1^2 d_3 \quad (3.12)$$

This established a threshold value using the results of Karstadt et al. For the different droplet diameters, the threshold velocity necessary to stay under this constant value found by Eq. 3.12 was derived as:

$$w_{th} \leq \sqrt{\frac{\xi}{d_3}} \quad (3.13)$$

Likewise, for the different rotational speeds 50 to 200 krpm, it was possible to derive diameters of droplets necessary to stay under the constant value:

$$d_{th} \leq \frac{\xi}{w_{th}^2} \quad (3.14)$$

To incorporate the Volvo test case into this analysis, the relative velocities for Cases III and IV were then used with the worst-case droplet diameter from the Karstadt et al. study. This suggests where the Volvo case may lie in relation to the threshold established by the constant value  $\xi$  from Eq. 3.12.

### 3.3.6 LIE Dependence on Droplet Impact Pressure

Using the Karstadt et al. case of droplet diameter  $d_3 = 470 \mu\text{m}$  and  $n_1 = 50 \cdot 10^3 \text{ rpm}$  as the no-erosion benchmark, calculated impact velocity from Section 3.3.1 together with

the droplet diameter give a threshold impulse below which erosion does not occur.

Once this threshold was established, the impulse due to the impact pressures of droplets of sizes ranging from 10–500  $\mu\text{m}$ , and velocities ranging from 1–150 m/s were calculated using the relationship suggested in Eq. 2.18.

In the same way as Section 3.3.5 above, impulse values for the different cases studied by CFD were then calculated and compared to the established threshold.

### 3.3.7 Making Use of Previous Relevant Computational Work

It is not straightforward to know what fraction of the admitted particles actually impinge on the blades and have the possibility to erode. In order to have some estimate of this, data from Ghenaïet’s study [37] was used, where  $m_{\text{loss}} = \varepsilon \cdot 0.01 m_{\text{admitted}}$ . Ghenaïet used sand particles as opposed to water droplets; nevertheless, it was used as an approximation of the order of magnitude of droplets that impinge on blades.

Cumulative erosion of the main blade (mg erosion of main blade), here called  $\zeta$ , can be related to overall erosion rate (mg erosion per g impacted particle), here called  $\varepsilon$ . Overall erosion rate and cumulative erosion were used to find the grams of particles responsible:

$$m_{\text{impacted}} = \zeta / \varepsilon$$

This gave the mass of particles impacted during one hour. Dividing by 3600 gave the impacts per second. Now, knowing the rate of sand admittance into the turbo compressor overall,  $m_{\text{admitted}}$ , it was found that:

$$x_{\text{impacted}} = m_{\text{admitted}} / m_{\text{impacted}}$$

From this, the mass of impinged particles was inferred knowing the total amount of admitted particles. See Appendix G for numerical values and explicit calculations: 1% of the particles admitted into the compressor were found to impinge on the main blade leading edge.

An estimate of eroded material mass was made by combining this information with the amount of ingested water from the Karstadt et al. study. Tabakoff & Hamed’s Eq. 2.20 describes specific erosion per impinged mass of abrasive (in their case coal ash, in the present case water), used to approximate a total mass of erosion. This erosion was calculated using the different impact velocities from the Karstadt et al. study.

### 3.3.8 LIE Dependence on Impact Angle

As no detailed two-phase simulations were conducted in this work, it was not possible to study different impingement angles using CFD.

Tabakoff and Hamed [33] presented an angle dependence of erosion complete with material constants for aluminium. For an arbitrary velocity of  $v = 100$  m/s, the angle dependence of erosion was explicitly calculated and illustrated for a set of different angles  $0 - 90^\circ$ . Particle size may affect the degree to which they follow the flow, which would lead to different impingement angles and hence different erosion potential.

When implementing erosion rate as  $\varepsilon$  from Eq. 2.20, it is necessary to remember that the particles described in both studies mentioned in Section 2.5.9 are solid. Material constants will likely be different for impinging liquid droplets, and may need to include effects of pressure waves or cavitation bubbles not present in solid particles.

# 4

## Results

This chapter shows results of the work performed in Star-CCM+, and also of calculations performed on the liquid impingement erosion models described in previous chapters.

## 4.1 CFD Results

Assorted results from the CFD simulations for Cases III and IV are presented in this section. For a short overview of the results of Cases I and II, the reader is referred to Appendix H.

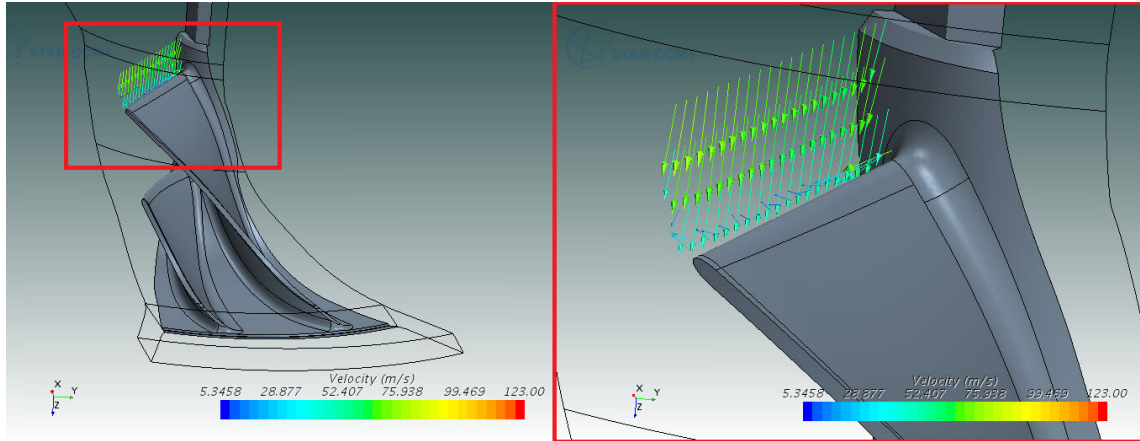
### 4.1.1 Cases III and IV

Table 4.1 gives a short summary of numerical results achieved from the set boundary properties as defined in Table 3.2.

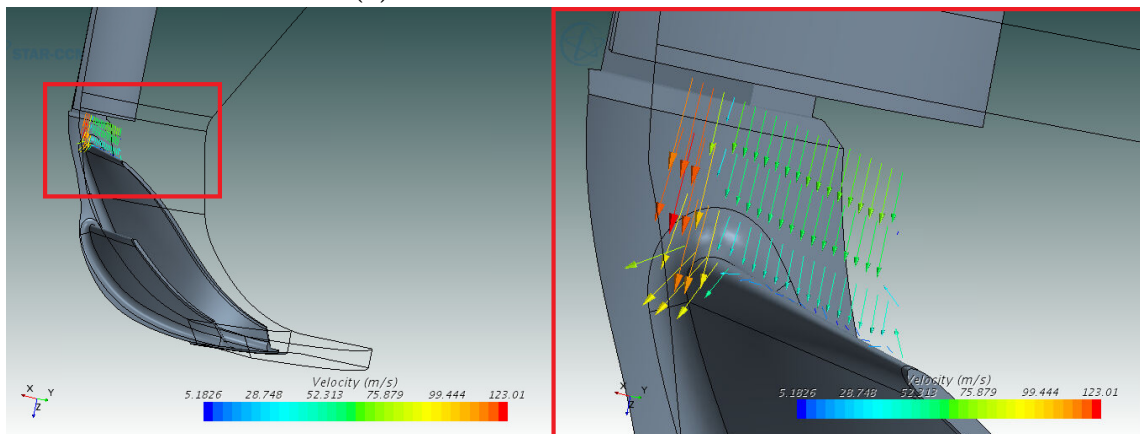
**Table 4.1:** A summary of the most important monitored quantities for CFD Cases III and IV. The last two rows are based on the calculated value  $P_{03}$ , the derivation of which is outlined in Section 3.2.2.

CFD Results	Case III	Case IV
Static pressure diffuser outlet (Pa)	135000	135000
Static pressure inlet (Pa)	98546.42	97584
Mass flow (kg/s)	0.02827	0.02827
Total pressure diffuser outlet (Pa)	153426	153563.5
Total pressure inlet (Pa)	98819.1	98540
Calculated total pressure volute outlet $P_{03}$ (kg/s)	146107.7	146160
Pressure ratio $P_{03}/P_{01}$ calculated	1.478	1.483

Absolute velocities near the leading edge for Case III and IV are compared in Fig. 4.1. The absolute velocity out of the nozzle for Case IV was much higher than the absolute velocity for the same location for Case III without the nozzle.



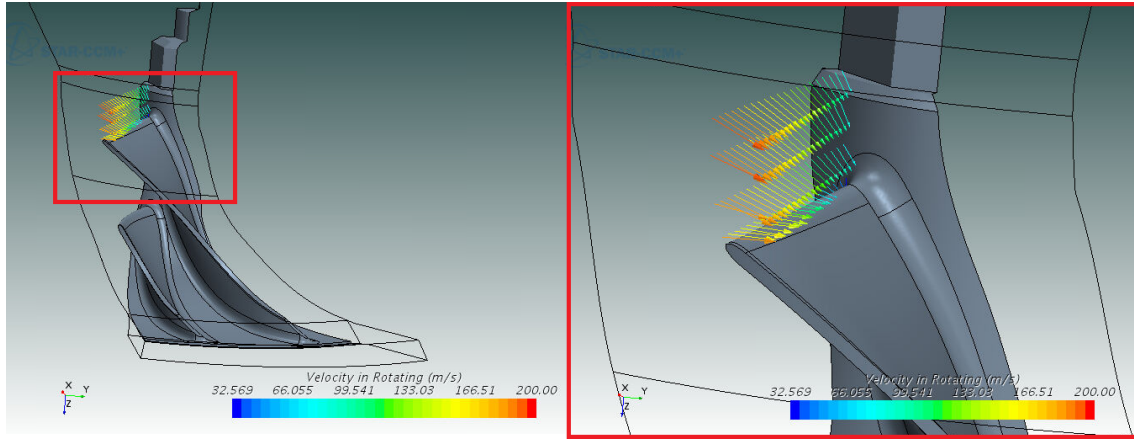
(a) Case III: standard intake nozzle



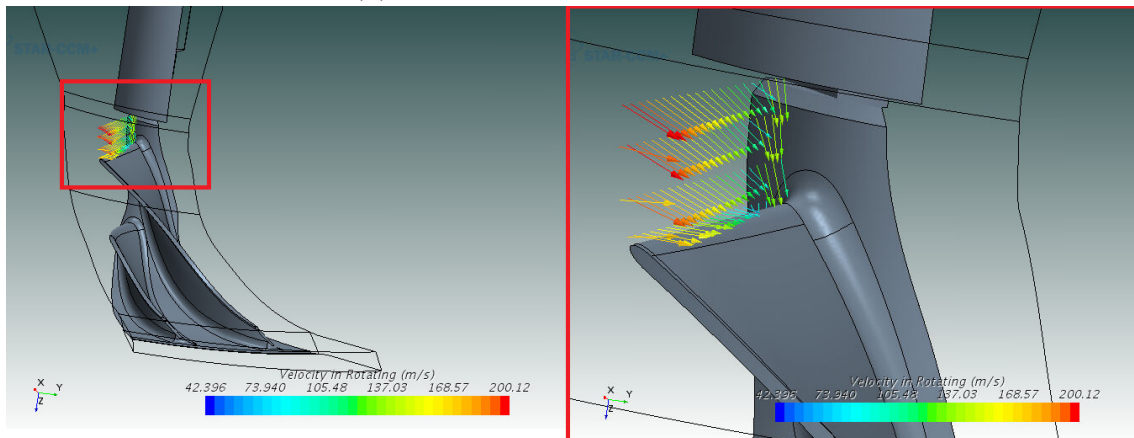
(b) Case IV: with the central nozzle installed.

**Figure 4.1:** Explicit view of absolute velocity vectors approaching the blade leading edge for Case III and IV. Both figures have the same scale: note the higher velocity through the central nozzle in (b) than for the same location in (a).

Relative velocities near the leading edge for Cases III and IV are compared in Fig. 4.2. The highest relative velocity in both cases is seen at the tip.



(a) Case III: standard intake nozzle



(b) Case IV: with the central nozzle installed.

**Figure 4.2:** Relative velocity vectors in the vicinity of the blade leading edge for Cases III and IV. The highest relative velocity is observed at blade tip.

A more exact way of visualising the distribution of velocities close to the blade leading edge is to extract the magnitudes of velocity at points close to the blade, and to show these in a graph related to the radial blade length. The positions where these point measurements have been taken are shown in Fig. 4.3.

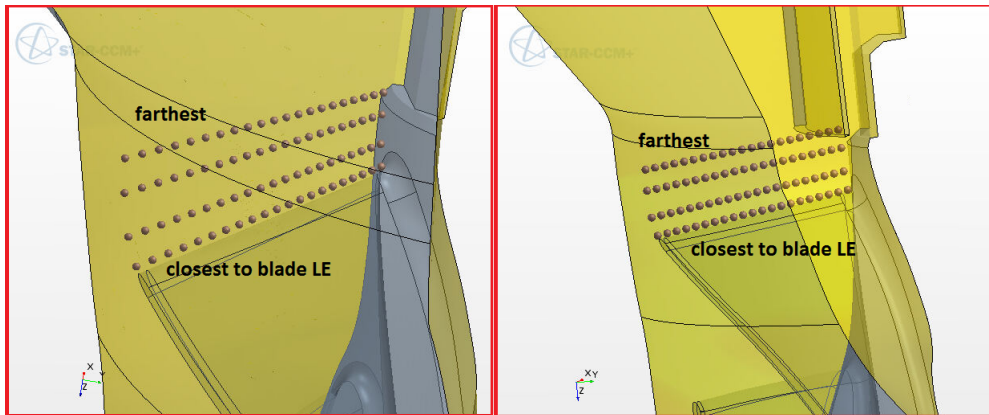
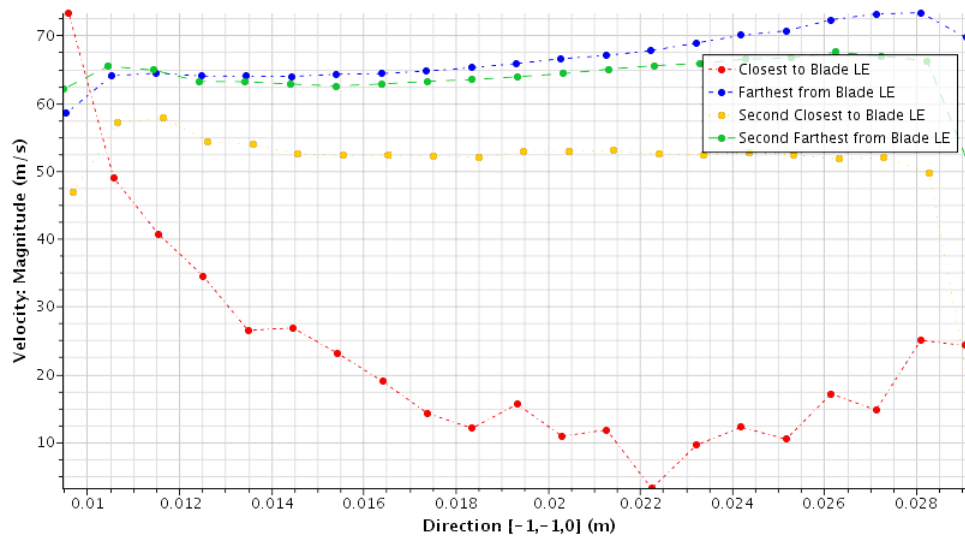
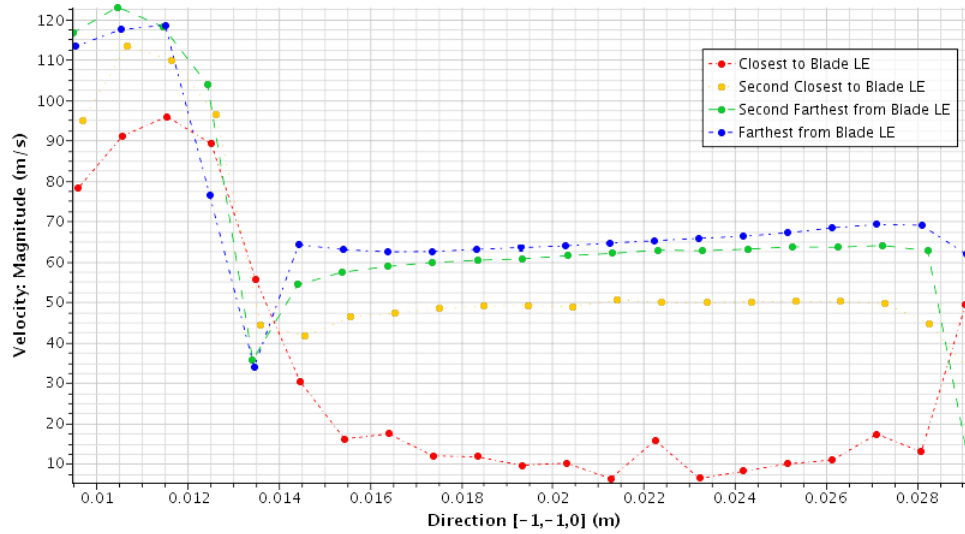


**Figure 4.3:** Illustrating the measurement positions used for magnitudes of relative and absolute velocity in Figs. 4.4 and 4.5 .

Graphs of distributions of absolute velocity magnitudes at these points along the blade leading edge are given in Fig. 4.4. Low absolute velocities closest to the blade is an effect of the wall no-slip condition. Note how the absolute velocity closest to the hub in Fig. 4.4(b) is high – this is because the flow coming out of the central nozzle is at a higher pressure and therefore travels at a higher speed than the rest of the flow.



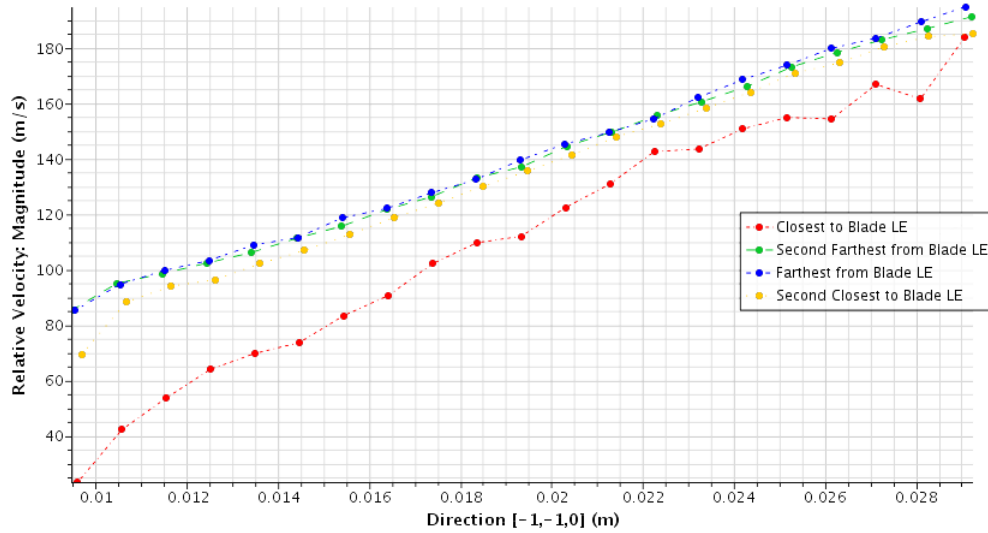
(a) Case III: standard intake nozzle



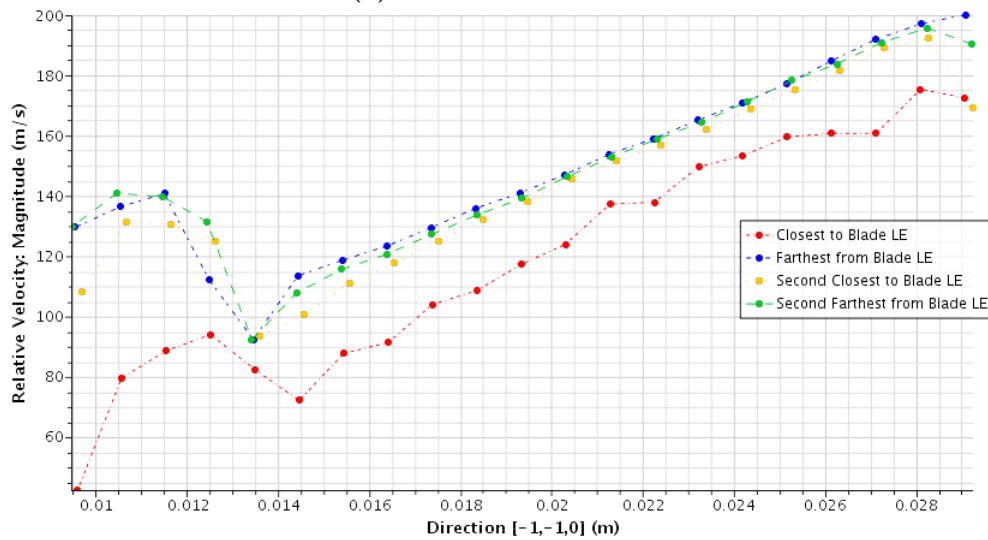
(b) Case IV: with the central nozzle installed.

**Figure 4.4:** Pictured here are the magnitudes of absolute velocity at different distances upwards from the blade for both cases. The  $x$  axis shows distance along the radial length of the blade tip. Locations of the samples can be seen in Fig. 4.3. Note how the absolute velocity closest to the blade is very low.

The corresponding graphs for relative velocities are shown in Fig. 4.5. The relative velocities increasing along the radius of the blade is an expected effect of the tangential blade speed increasing.



(a) Case III: standard intake nozzle



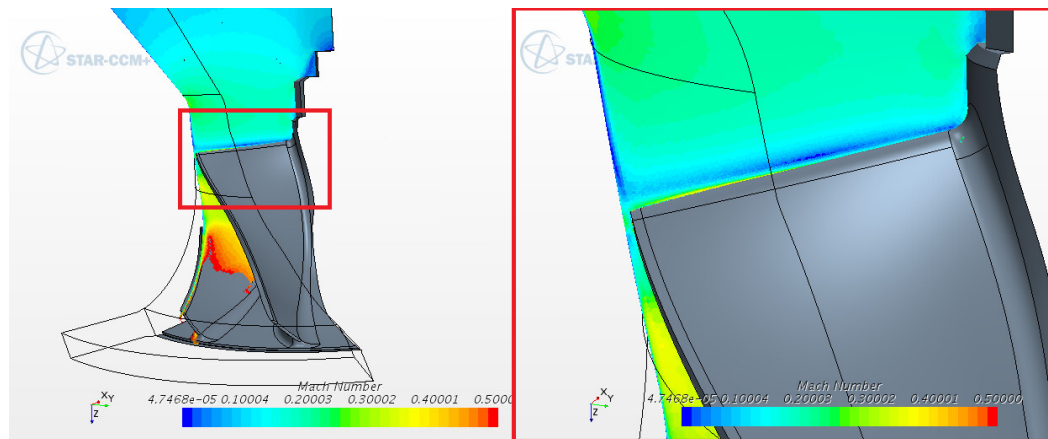
(b) Case IV: with the central nozzle installed.

**Figure 4.5:** Pictured here are the magnitudes of relative velocity along the blade leading edge, at different distances upwards from the blade. The locations of the samples can be seen in Fig. 4.3. Note how relative velocity increases linearly along the blade length for (a).

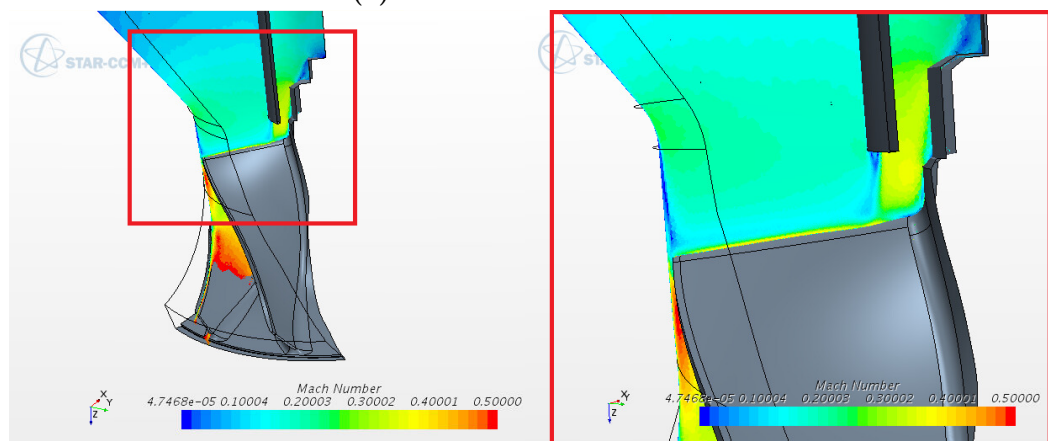
Notice that the central nozzle (Case IV) in Fig. 4.5(b) expels gas at a higher velocity than the standard intake (Case III) in Fig. 4.5(a). The relative velocities exiting the nozzle are as high as the relative velocities at half the blade length for the standard

intake.

The restricting behaviour of the central nozzle compared to a standard intake is shown in Fig. 4.6. The Mach number up to the blade is consistent and low for the standard case, whereas the nozzle introduces a region of slightly higher Mach number at the blade root.



(a) Case III: standard intake nozzle.



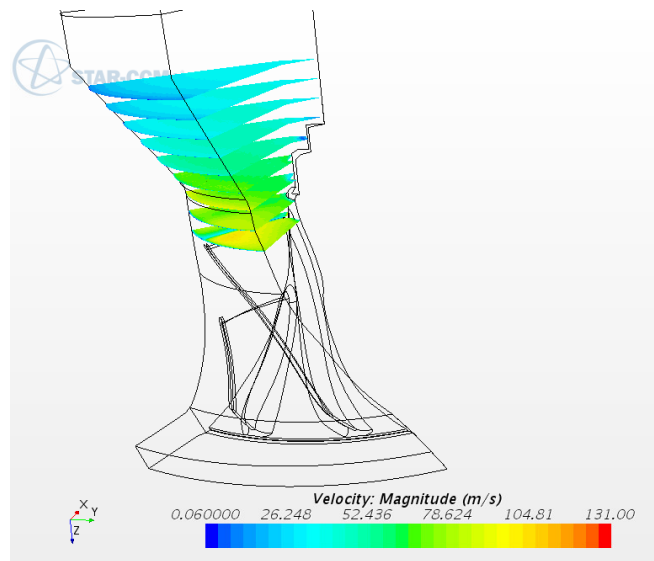
(b) Case IV: with the central nozzle installed.

**Figure 4.6:** A view of the Mach number in a plane that intersects with the top of the blade leading edge for cases III and IV. Both are shown in the same scale: note the lower Mach number in Case III. Mach number values higher than the maximum indicated by the scale are not visible in these figures, which is why the colours disappear further down the blade passage towards the impeller outlet.

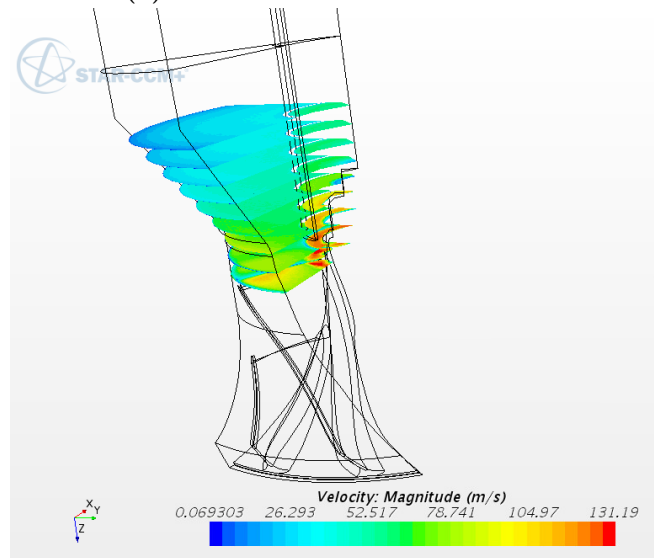
The higher velocity gas appears to flow more or less directly downwards from the nozzle – the increased absolute velocity in e.g. Fig. 4.4(b) is observed up to a radius of around 13mm, which is roughly the central nozzle radius itself.

Absolute velocity magnitudes for both cases as the flow approaches the impeller blades

through the different inlets are shown in Fig. 4.7.



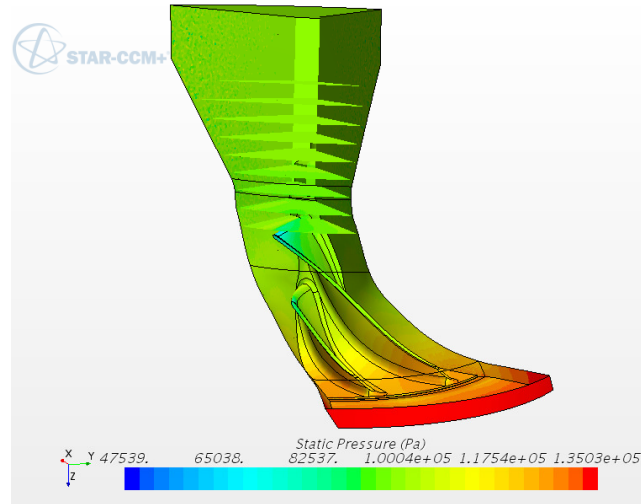
(a) Case III: standard intake nozzle.



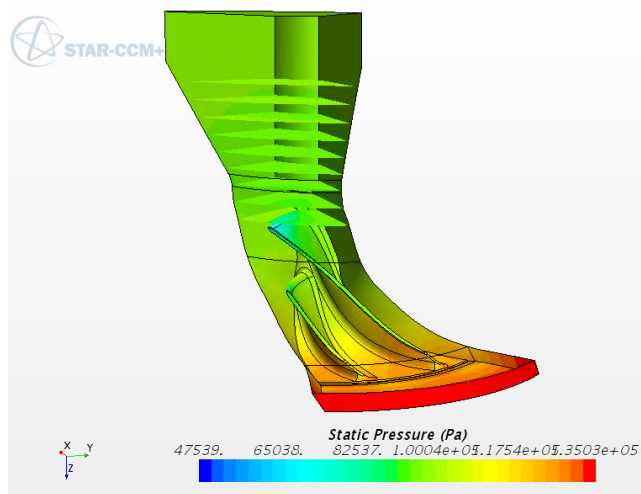
(b) Case IV: with the central nozzle installed.

**Figure 4.7:** Views of the development of absolute velocity as gas flows towards the impeller. Both plots are shown on the same scale so that it is possible to see how much faster the central nozzle makes the flow travel.

The static pressure rise delivered by the compressor is illustrated in Fig. 4.8. In comparison to the pressure rise in the impeller, the pressure difference at flow profile into the compressor is not so significant.



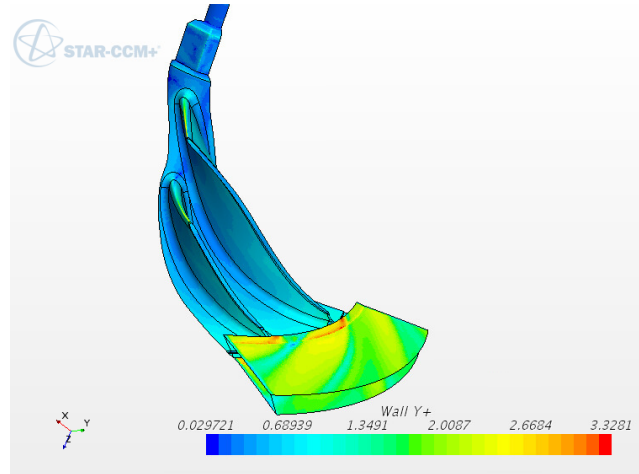
(a) Case III: standard intake nozzle.



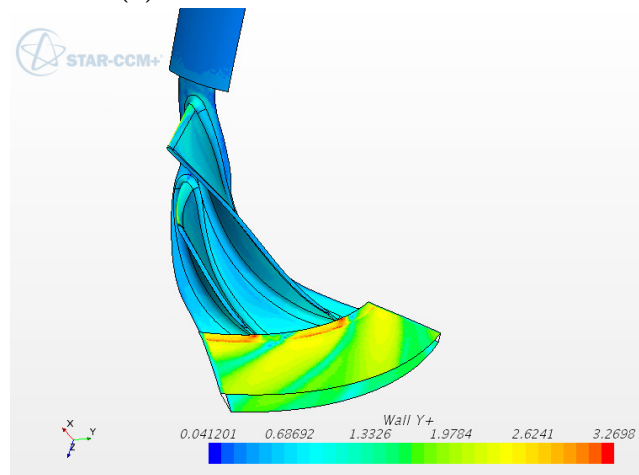
(b) Case IV: with the central nozzle installed.

**Figure 4.8:** Static pressure along the sector for both Case III and IV. There appears to be little difference.

Wall  $y^+$  values for the impeller and diffuser for both Case III and IV are shown in Fig. 4.9. Regions of highest  $y^+$  values are blade leading edges and diffuser inlet.



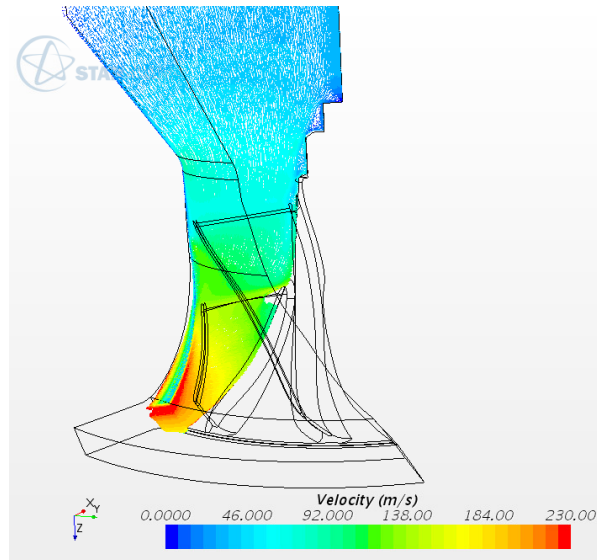
(a) Case III: standard intake nozzle.



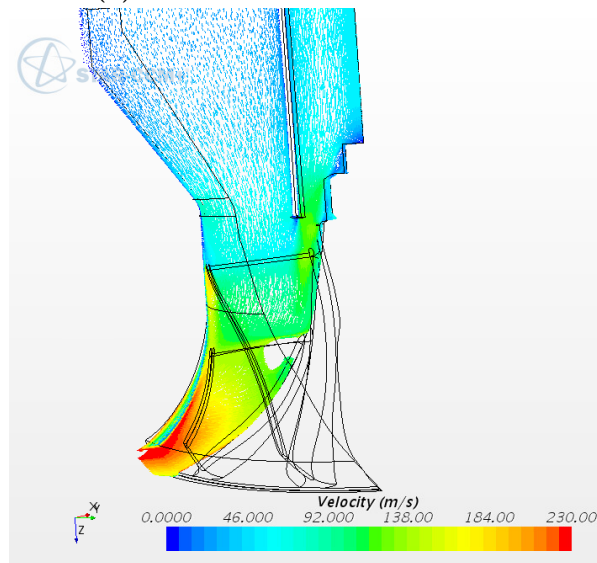
(b) Case IV: with the central nozzle installed.

**Figure 4.9:** Wall  $y^+$  values for Cases III and IV. Throughout the regions of most disturbed flow (the impeller) the  $y^+ \lesssim 1$ . In the diffuser a  $y^+ \approx 3$  is encountered.

For a more detailed picture of the flow acceleration as the central nozzle approaches the hub, see Fig. 4.10. The comparison between velocity vectors in a meridional plane shows the difference in flow field.



(a) Case III: standard intake nozzle.



(b) Case IV: with the central nozzle installed.

**Figure 4.10:** A view of the flow in a cross-section between blade and splitter. The identical scale emphasises the higher absolute velocity flow seen coming out from the central nozzle.

### 4.1.2 Effect of Overall Mesh Refinement on Calculated Efficiency

Results of the grid independence study described in Section 3.2.12 are given here. The efficiencies can be seen in Fig. 4.11, which shows that calculated efficiency rapidly increases with mesh refinement until a base size of approximately 1 mm is reached. However, the absolute magnitude of change in calculated efficiency is not very great even when comparing the most coarse mesh to the most fine:  $\eta \approx 0.86$  and  $\eta \approx 0.9$  respectively.

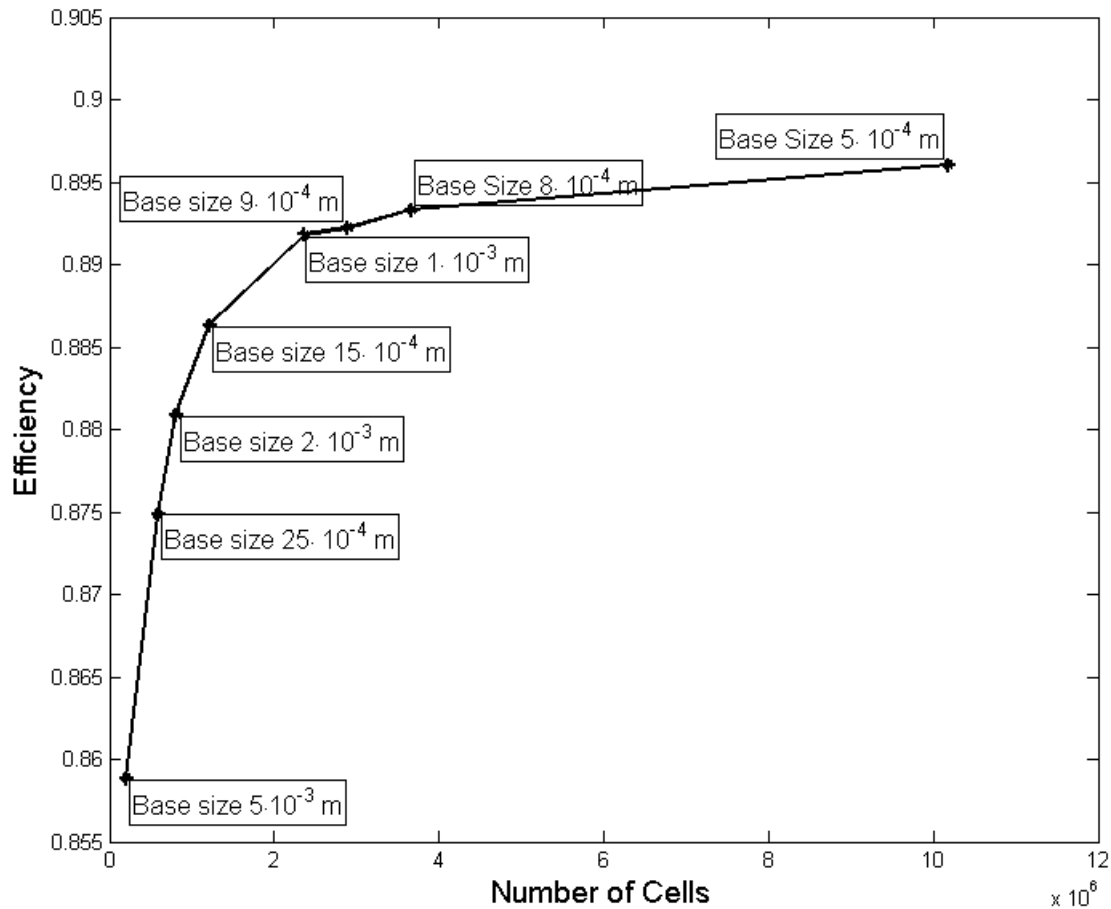


**Figure 4.11:** Calculated total-to-total efficiency from inlet to diffuser outlet for different base sizes, resulting in different numbers of cells in the computational mesh.

The static pressures at inlet are shown in Fig. 4.12, where a decrease in inlet pressure can be seen as the mesh is refined and the number of cells increases. Again this stabilises somewhat at base size 1 mm.

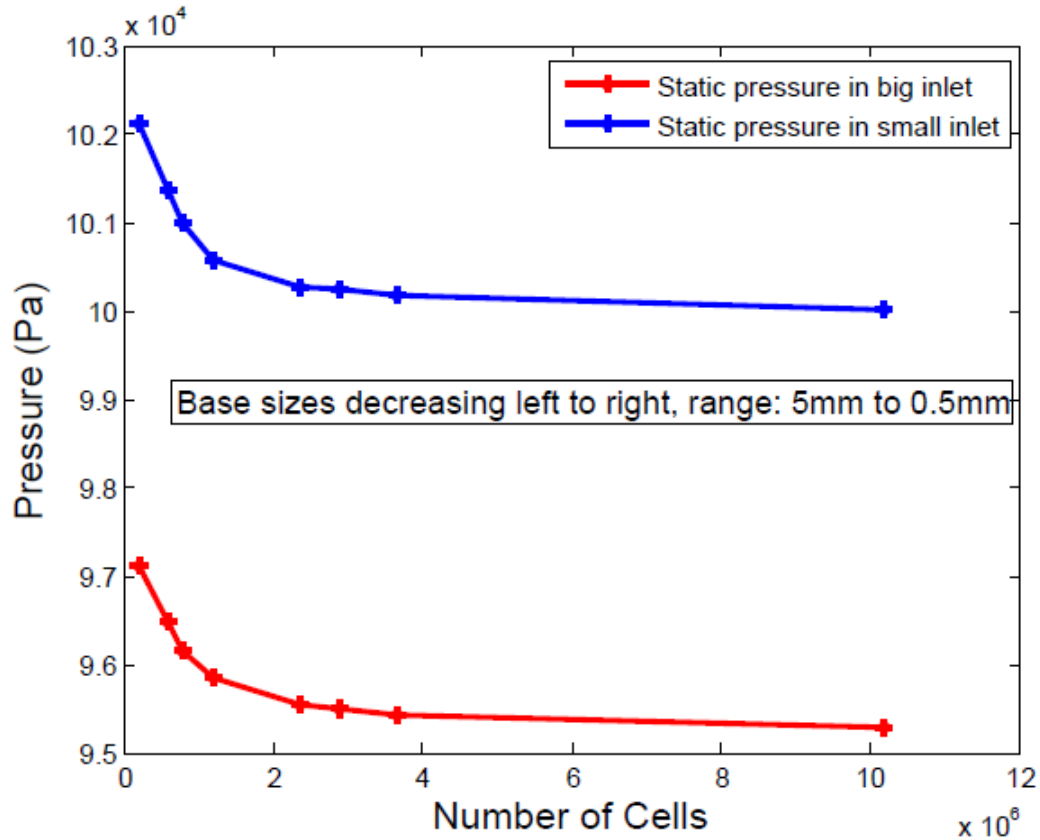


**Figure 4.12:** The variation of calculated inlet static pressures with changing base size. The base sizes are, from left to right, as presented in Fig. 4.11 above (and as described in Section 3.2.12). The *big* and *small* inlets represent the main intake pipe and the smaller nozzle, respectively. The curve begins to level out at base size 1 mm.

To conclude the mesh study: a base size of 1 mm seems appropriate considering the trade-off between accuracy and computational time.

## 4.2 Liquid Impingement Erosion Investigation

This section presents a collection of the results as pertaining to liquid impingement erosion relationships.

### 4.2.1 Making Use of Previous Experimental Work on LIE

As presented in Section 3.3.1, the Stokes number was calculated for the different droplet sizes of the Karstadt et al. experiment, but with flow parameters from Cases III and

IV.

A diagram of the droplet diameter relationship to the resulting Stokes number for Case IV is given in Fig. 4.13. Note that the Stokes number is on the order of  $10^2$  for all droplet diameters studied in the Karstadt et al. experiment. Similar graphs are obtained for Case IV and also for both definitions of system time constant  $\tau_c$  (Eqs. 2.24 and 2.25). This strongly indicates a ballistic behaviour in particles of these sizes, impacting blades rather than following the flow streamlines around blades.

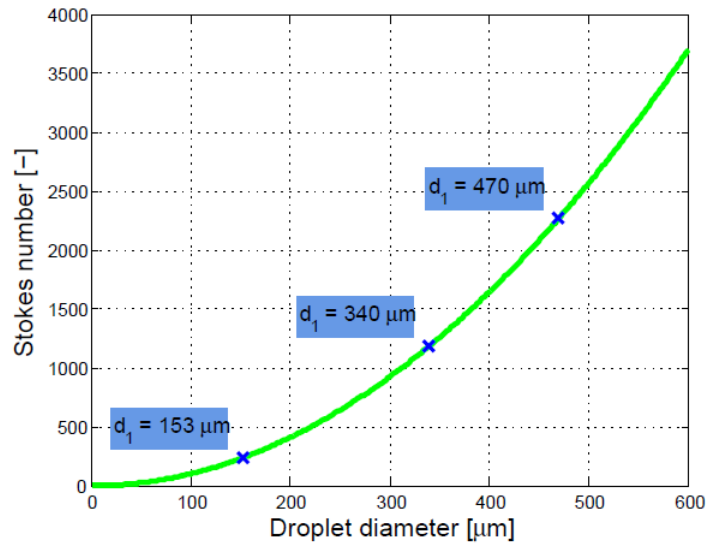


**Figure 4.13:** A graph to illustrate the relationship between Stokes number and droplet diameter as presented in Eq. 2.22 from Section 2.6.4. This graph was created for Case III using the definition of system time constant according to Eq. 2.25 as  $L_c/U_c$  where  $L_c$  is inlet pipe diameter and  $U_c$  is the impact velocity at blade tip as calculated by CFD, seen in Fig. 4.5(a) to be  $\approx 190$  m/s. The three smallest droplet sizes tested in the Karstadt et al. experiment are marked for reference.

#### 4.2.2 Previous Relevant Computational Work Applied

The total mass of water ingested for the droplet diameter experiments was 5 litres per experiment; one per cent of this means 50 g. Applying the equation for relative speeds as calculated from the Karstadt et al. study, an exponential relationship results, shown in Fig. 4.14.

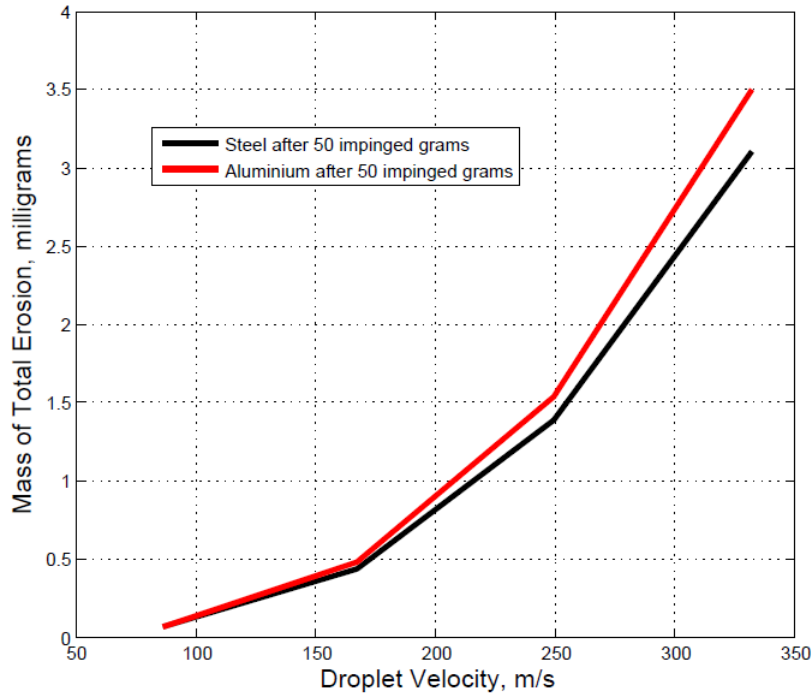


**Figure 4.14:** Velocity dependence of coal ash impingement erosion on an aluminium surface compared to a steel surface, as calculated from Tabakoff & Hamed [33]. The relative velocities used are the ones calculated from Karstadt et al., as is the amount of water.

### 4.2.3 LIE Dependence on Impact Velocity

Erosion dependence on the impact velocity to the power of some  $n$  gives an exponentially increasing erosion with velocity. As can be seen from the results of Karstadt et al., such a relationship does not appear to be able to incorporate the trend of erosion saturation occurring around the increase from 150 krpm to 200 krpm.

However, as a tool for comparison of relative erosion, this relationship naturally indicates more erosion for CFD Case III than for Case IV with the central tube. This is because the maximum impact velocity of the droplets is constrained by the nozzle in Case IV but not in Case III. For the standard intake pipe of Case III, maximum droplet impact speed is instead greatly governed by blade tip speed.

### 4.2.4 LIE Dependence on Droplet Size

Similarly to the previous section, a description of erosion based on the exponent of any single characteristic will not carry sufficient information. Such a relationship is unable to incorporate the apparent erosion saturation for droplet diameters larger than  $470 \mu\text{m}$

in the experiment by Karstadt et al. Furthermore, nothing is known of the droplet diameter for the Volvo case.

#### 4.2.5 LIE Relation to Cavitation Erosion

Cavitation erosion being dependent on flow velocity raised to an exponent of 6 or 7 provides the same type of guidance as the other exponents suggested in Section 3.3.2.

Cavitation bubble equilibrium size is investigated in Table 4.2, where different temperatures are shown to yield different equilibrium bubble sizes. Data is taken for water [50, 51]. For the operating cases III-IV studied here, it is assumed that the values for surface tension and vapour pressure for 24 °C fall between the values for 20–25 °C.

The Karstadt et al. study was performed at ambient conditions, which are assumed to correspond to 25 °C.

**Table 4.2:** Table of numerical values used in calculations.

Temperature (°C)	20	25	30
$\sigma$ (mN/m)	72.75	71.99	71.20
$p_v$ (kPa)	2.339	3.170	4.246
$R_{eq}$ ( $\mu\text{m}$ )	62.206	45.420	33.537

In order to avoid cavitation erosion damage at ambient conditions, Table 4.2 suggests liquid droplet radii need to be kept under 45  $\mu\text{m}$ . In terms of applying this theory to the Karstadt et al. study, the result is trivial as all droplets investigated are larger than this size and therefore all are cavitation-prone. Similarly to Section 4.2.4, no information is available on the droplet sizes for Cases III and IV.

#### 4.2.6 LIE Dependence on Both Impact Velocity and Droplet Diameter

For the Karstadt et al. study, the supposed impact velocity at rotational speeds  $n_i$  is extracted and can be read from Table 4.3 as  $w_i$ ,  $i = 1,2,3,4$ .

**Table 4.3:** Table of impact velocities in Karstadt case.

Rotational speed $n$ (krpm)	50	100	150	200
Blade speed $U$ (m/s)	82.9	165.8	248.7	331.6
Gas velocity $c$ (m/s)	24.5	24.5	24.5	24.5
Resulting droplet impact speed $w$ (m/s)	86.4	167.6	249.9	332.5

Using the impact velocity for the no-erosion case means calculating for  $n_1$ :  $w_{th} = \sqrt{U_1^2 + c^2} = \sqrt{82.9^2 + 24.5^2} = 86.4 \text{ m/s}$ . Combined with the identified largest no-erosion diameter  $d_3$ , this gives:

$$\xi = w_{th}^2 d_3 = 86.4^2 \cdot 470 \cdot 10^{-6} = 3.51$$

Solving for the droplet diameter and inserting the values for the different relative velocities (impact speeds) found in the Karstadt et al. study gives an indication of how small droplets need to be at those speeds to not cause damage. The values found are shown in Table 4.4. Similarly, droplet diameter values from the Karstadt et al. study are inserted to identify threshold velocities below which there should be no erosion, for those droplet sizes. The values for this are found in Table 4.5.

**Table 4.4:** Table of threshold droplet diameters for impact velocities in Karstadt case.

Droplet Impact Speed $w$ (m/s)	86.4	167.6	249.9	332.5
Threshold diameter ( $10^{-6}$ m)	470	125	56.2	31.8

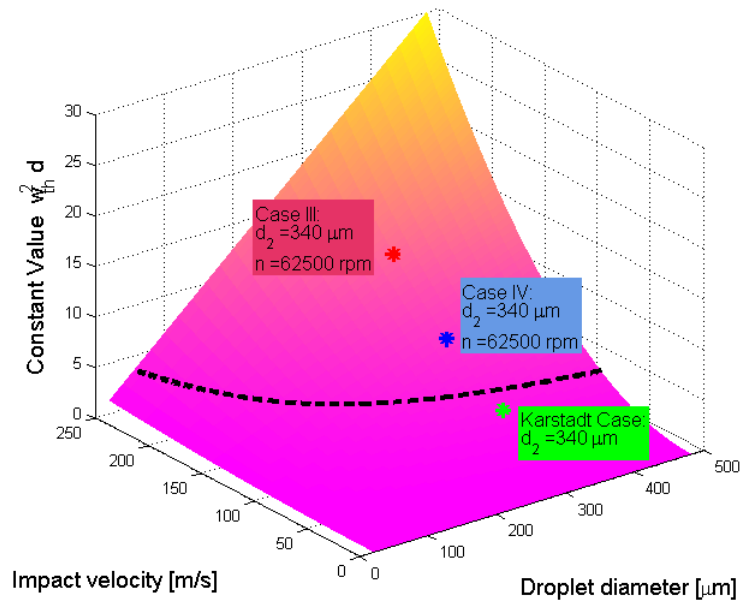
**Table 4.5:** Table of threshold speeds for different droplet diameters in Karstadt case.

Droplet Diameter ( $10^{-6}$ m)	153	340	470	1120
Threshold speed (m/s)	151.5151	101.6394	86.4476	56.0006

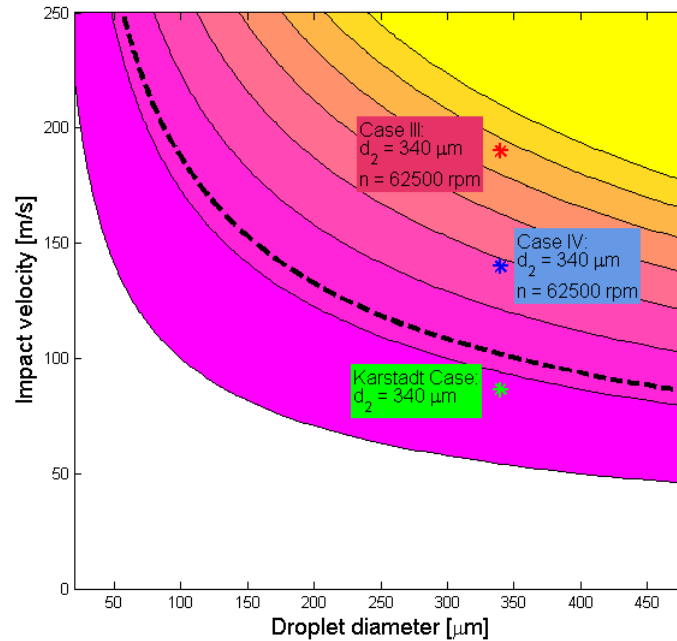
A threshold diameter is identified for the present operating case. It represents the size limit for droplets in order to avoid erosion in Case III and in Case IV:

For Case III, the relative tip speeds are, from CFD, seen to be  $\approx 200 \text{ m/s}$ . This suggests it is necessary to have  $3.51/200^2 = 87 \mu\text{m}$  droplet size or lower to avoid erosion. For Case IV, considering that droplets will not be able to impinge on a radius further out than the central nozzle radius, the relative velocity for droplets will be  $140 \text{ m/s}$ . The equation then gives:  $3.51/140^2 = 179 \mu\text{m}$ .

The relationships can be illustrated graphically by plotting the value of  $w_{th}^2 d$  for a range of relative velocities and droplet diameters. The result is shown in Fig. 4.15, where the intersection with the identified threshold value is plotted as a black dotted curve both on the three-dimensional surface in (a) and the two-dimensional illustration in (b). Three cases are illustrated as points in this diameter-velocity-erosion space to show their relation to the threshold value.



(a) 3D illustration of erosion potential of a range of diameters and velocities.



(b) A two-dimensional rendition of (a) above showing contours of erosion potential.

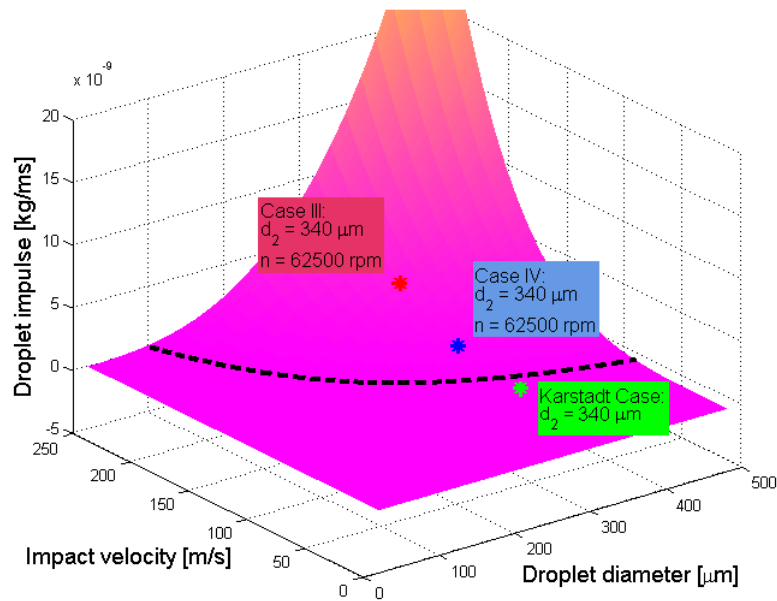
**Figure 4.15:** Relating impact velocity to diameter and the intersection with the threshold  $\xi = 3.51$  value as determined by the non-erosion case in Karstadt et al. study. Shown as points are the no-erosion Karstadt case of slowest rotational speed  $n_1$ , CFD Case III and CFD Case IV. All are plotted with the second-smallest droplet diameter  $d_2$ .

### 4.2.7 LIE Dependence on Droplet Impact Pressure

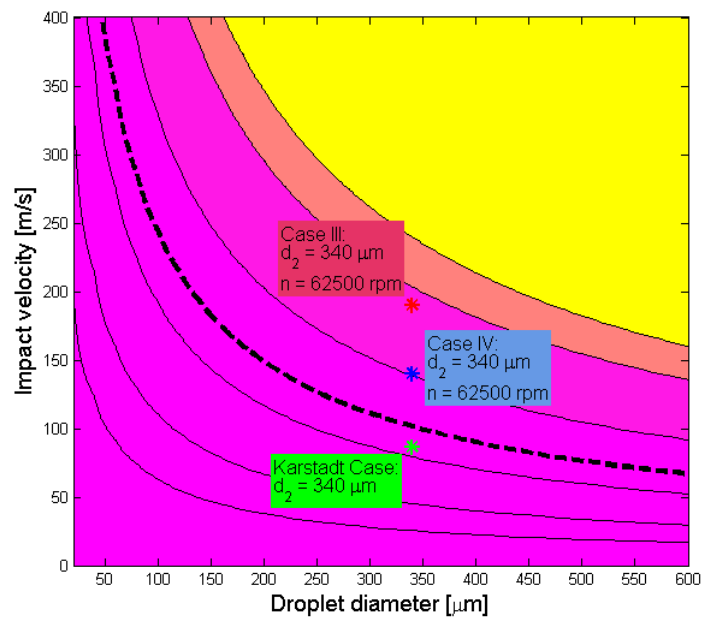
To identify the threshold impulse, the no-erosion case from Karstadt et al. where  $n_1 = 50$  krpm and droplet size  $d_3 = 470 \mu\text{m}$  is used [36]. Using a more conservative threshold impact velocity of  $v = 80$  m/s rather than the calculated  $w_1 = 86.4$  m/s, this translates to a threshold impulse as defined by Eq. 2.18:

$$I = \left(1 - \sqrt{1 - \frac{80^2}{1500^2}}\right) 1000 (1500 + 2 \cdot 80) \pi (235 \cdot 10^{-6})^3 \left(\frac{80}{1500}\right)^2 = 2.7399 \cdot 10^{-10} \text{ kg/ms} \quad (4.1)$$

An illustration of the three-dimensional surface created by plotting the impulse as a function of impact velocity and droplet diameter is given in Fig. 4.16(a), where the intersection with the threshold impulse below which no erosion should occur is marked as a black dotted curve. The same intersection is shown in Fig. 4.16(b), but with the impulse surface projected onto the  $xy$ -plane as contours, making it easier to see the relation of the different points to each other. The contour plots in Figs. 4.15(b) and 4.16(b) do not show the erosion potential values explicitly, but serve instead as a more conceptual and visual aid.



(a) 3D illustration of erosion potential of a range of diameters and velocities.



(b) A two-dimensional rendition of (a) above showing contours of erosion potential.

**Figure 4.16:** Showing how ranges of impact velocities and droplet diameters relate to a threshold value of erosion potential that is droplet impulse. Shown as points are the no-erosion Karstadt case of slowest rotational speed  $n_1$ , CFD Case III and CFD Case IV. All are plotted with the second-smallest droplet diameter  $d_2$ .

### 4.2.8 LIE Dependence on Impact Angle

Figure 4.17 shows the result of applying the formula by Tabakoff and Hamed given in Eq. 2.20 for an arbitrary impact velocity of 100 m/s and the assumption that five kilograms of droplets were admitted to the compressor, of which one percent impinged on blades. It can be seen that for aluminium, the maximum erosion occurs at moderate impact angles.

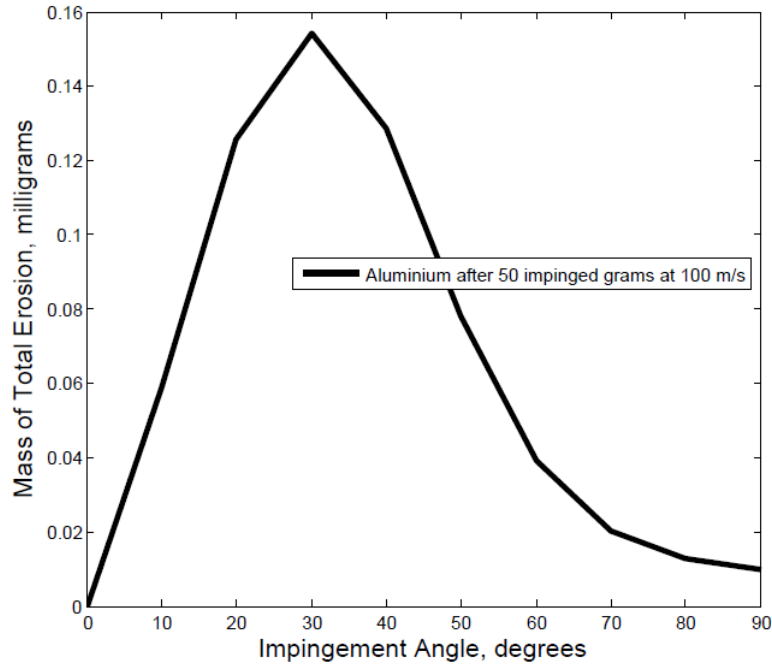


**Figure 4.17:** The impingement angle dependence of coal ash impingement erosion on an aluminium surface, as calculated from Tabakoff & Hamed [33]. Note that the highest erosion seems to occur at approximately 30 degrees.

# 5

## Discussion & Future Prospects

In this final chapter, the methods used and results achieved throughout this work are critically assessed. Ideas on how to improve and develop this work are given, as well as a set of conclusions to summarise the insights reached.

## 5.1 CFD

The computational fluid dynamics part of this work has significant room for improvement and development. Some of the areas which can be improved are discussed below.

### 5.1.1 Geometry

Simplifying the geometry removes information which will tend to reduce the accuracy of the solution. One very pronounced consequence of the choice to not include the volute in the simulation was an increased difficulty of convergence. Having an outlet in the simulation with so much tangential outflow, as was the case with the diffuser, created difficulties for the solver. A lack of knowledge as to how to connect one-seventh of the existing geometry to a full volute prevented the inclusion of volute in this work.

Apart from this, the choice to use a periodically repeated geometry rather than to perform calculations on the entire component also raises questions as to the accuracy of assumption and relevance of result to reality. It may be unrealistic to assume that the blade geometry is identical for the full rotation. There may also be e.g. numerical effects which become more critical when switching to a two-phase solution, which may suffer more greatly from the simplification in periodicity – for example through the need for irregular mesh elements in the singular point in the centre where the two periodic surfaces meet. This needs to be investigated further and motivated more thoroughly if the work is to be continued.

All geometry simplifications should ideally be investigated: the ported shroud, the omission of volute etc. Knowing what can be neglected and what must not be neglected is of vital importance to the relevance of any result.

### 5.1.2 Mesh

Better control of the mesh is needed if more detailed CFD simulations with e.g. two-phase flow are to be performed for this geometry. Hexahedral elements are highly preferable when tracking small particle behaviour, as the interpolation of their movement inside computational cells is simplified by the regularity of the elements.

It could be valuable to perform a  $y^+$  refinement dependence study. This would mean changing the width of the prism layers, solving the flow and seeing how the different prism sizes affects the  $y^+$  values which in their turn may affect the overall efficiency and flow characteristics. Such a study would be even more crucial to perform if this work was taken further to try and perform detailed two-phase simulations with particles impacting blades and walls.

The computational meshes for the cases of standard intake and central nozzle intake differed with respect to inlet and impeller sections. Cell counts for the two geometries

were given in Table 3.1. The inlet section for the central nozzle intake had more than double the amount of cells of the standard intake; this is understandable as the central nozzle introduces complications which have to be addressed by more prism cells and also smaller cells. In contrast, the impellers of both intake types have very similar cell counts. The result of a similar cell amount for two geometries different in complexity means that the less complex geometry will have smaller cells overall, which can be seen in Fig. 3.9.

As mentioned, all specifications in Star-CCM+ were kept as similar as possible for both intake cases. For this reason, the explanation for such distinctly differing impeller meshes must lie either with the meshing optimisation algorithm in Star-CCM+ or with human error. Nevertheless, the grid independence study of Section 4.1.2 suggested that changes in results were increasingly marginal for meshes more refined than the mesh chosen for the central nozzle case.

### 5.1.3 Choice Of Models

As the flow within turbomachines is highly turbulent with many disturbances, the choice of turbulence model can have a large effect on the overall solution. Future work should investigate the effect of choosing different turbulence models on both one-phase flow and two-phase flow.

### 5.1.4 Reaching and Evaluating Convergence

One drawback of this CFD investigation is that no rigorous convergence criteria have been formulated to allow automatisation of the decision of when a solution is “good enough”. The simulations proved difficult to run without supervision: many manual adjustments and ramping of different simulation parameters were performed during iterations of the solver. It would not have been practical to implement automatic stopping criteria for this initial investigation. In future however, when e.g. attempting different nozzle designs, automation of the process could be immensely time-saving and beneficial in terms of consistency.

## 5.2 Liquid Impingement Erosion

Indications of correlations between impact velocity and droplet diameters for erosion potential have been investigated. The consensus seems to be that erosion will be decreased for the case with the central tube nozzle, but a method of calculating absolute erosion has not been identified within this study.

The highest relative velocity in both Case III and IV is observed at blade tip, as shown in Fig. 4.2. Crucial for LIE mitigation is that admittance of droplets through the central

nozzle should restrict the relative impact velocities to lower than what is expected at the blade tip.

### 5.2.1 LIE Indicators

The different indicators of erosion captured a few trends, such as more erosion for higher velocities and bigger droplet diameters. However, none seemed able to capture the saturation occurring for the highest rotational speeds and largest droplets shown by Karstadt et al. A combination of these different models should be looked at in future, together with some attempted incorporation of the saturation behaviour.

### 5.2.2 LIE Predictors

All of the investigated methods show that erosion potential is lower for the central nozzle construction, but none can as yet quantify by how much. The idea of an impulse threshold for a certain impact velocity and droplet diameter seems sound, but the sparseness of experimental results to set proper thresholds made utilisation difficult. Furthermore, this is in effect yet another exponential relationship which fails to incorporate the saturation. Furthermore, the threshold was set *very* conservatively with regards to the Karstadt et al. study results for this initial investigation. Re-calculating the results of erosion models and classifying the case of  $n_2 = 100$  krpm and  $d_3 = 470 \mu\text{m}$  as effectively erosion-less would lead to a much higher threshold and would probably show that the central nozzle avoids erosion for the bench test case.

## 5.3 Overall Drawbacks and Considerations

Generally speaking, the problem of liquid impingement erosion in an application such as low-pressure exhaust gas recirculation is very complex. There is a myriad of branches along which this problem can be elaborated. For example, it is impossible to say at this stage how a central nozzle would affect the formation of droplets. Perhaps it would allow for a greater droplet condensation, and a bigger droplet size ripping off the nozzle walls, and so causing more erosion. Perhaps the droplets would have stayed small and harmless if they had been allowed to spread out in the whole intake. Or, if they had collected on the walls of the main intake pipe, perhaps they would have behaved like the wall film in the Karstadt et al. study, and become atomized by the recirculation regions at the ported shroud which is present in the real compressor.

### 5.3.1 Flow Interpretation and Operating Points

Figures 4.4 and 4.5 show the relative and absolute velocity magnitude graphs of flow development along blade leading edge. Gas exiting the central nozzle flows towards the blade leading edge significantly faster than the gas in the outer, main pipe. The impact velocity is interpreted to be increased because of the central nozzle being so narrow in relation to the mass flow coming through it.

Different engine load points affect the mass flow of EGR through the low-pressure route and therefore through the central nozzle for the new design. Investigating control strategies for EGR loops at different load points is not in the scope of this work. It is however safe to assume that for increasing engine load, the EGR path will switch to high-pressure at some point. When this happens there will be no exhaust gas specifically routed through the central nozzle.

It must nevertheless be stressed that a low-pressure EGR has been specifically studied here, i.e. a low mass flow and pressure ratio. The central nozzle however, once installed, will be present for the whole operational range. It may be expected that the obstruction it causes is much more significant at a higher mass flow. For example: as the central nozzle flow approaches the impeller eye, the impeller screw will force the central flow out radially, and the inner walls of the nozzle will confine this radially moving gas. Flow will not be able to spread itself over the entire radius of the channel and blade. This will cause an acceleration/increase in pressure in the nozzle and could perhaps cause a local shock. There would then be a shock both at blade tip and root, which raises issues for performance and material longevity.

## 5.4 Accuracy of Compressor Map

The compressor map used, shown in Fig. 3.3, is for a compressor with a ported shroud. Compressors with ported shrouds have wider maps, meaning larger operational regions. The compressor used in simulations does not have a ported shroud, which suggests it should reach surge and choke limits sooner. The chosen operating points for Cases III and IV are quite far to the right in the map. It may be possible that the lack of ported shroud has a significant enough effect on the flow characteristics for it to have implications for convergence issues.

## 5.5 Conclusions

An aim of admitting exhaust gas through a narrow central nozzle was to reduce the velocity at which exhaust gas condensate hits the compressor blades. The computational work performed here has indicated that exhaust gas will flow faster when admitted through a central nozzle intake, compared to a standard intake. However, the computational

analysis suggests that this speed increase is dwarfed by the speed-reducing effect of the placement of the nozzle, evading the high flow speeds near blade tips.

The framework for two-phase CFD simulations is provided, and arguments are presented to support the use of the most simple kind of two-phase analysis for relevant results in future.

The assessed erosion models have unearthed relevant factors for liquid impingement erosion. Indication is given of the erosive potential of droplet diameter and droplet impact velocity combinations, through suggestions of threshold values obtained from accessible experimental results. A starting point for the quantification of erosion for aluminium at different impingement angles is given through an explicit formula of eroded material per impinged mass. The formula has been interpreted and applied for actual numerical values.

This work has illuminated several aspects of designing an erosion resistant turbo compressor intake. It is at this stage not clear what an optimal design would be, but the work performed strongly suggests that a central nozzle would decrease the erosive potential of water droplets in the exhaust gas. Given the possible advantages of lower exhaust emissions and simpler aftertreatment systems, it may be of great commercial interest to Volvo Trucks to keep developing this design for a new green DME truck in the near future.

# Bibliography

- [1] European Commission Press Release Database. Transport 2050: The major challenges, the key measures, 2011. [http://europa.eu/rapid/press-release\\_MEMO-11-197\\_en.htm](http://europa.eu/rapid/press-release_MEMO-11-197_en.htm) Retrieved 7th June, 2016.
- [2] European Commission Climate Action. Road transport: Reducing co2 emissions from vehicles, 2016. [http://ec.europa.eu/clima/policies/transport/vehicles/index\\_en.htm](http://ec.europa.eu/clima/policies/transport/vehicles/index_en.htm) Retrieved 7th June, 2016.
- [3] European Commission Climate Action. Reducing co2 emissions from heavy-duty vehicles, 2016. [http://europa.eu/rapid/press-release\\_MEMO-11-197\\_en.htm](http://europa.eu/rapid/press-release_MEMO-11-197_en.htm) Retrieved 7th June, 2016.
- [4] Prenzinger P. Hiereth, H. *Charging the Internal Combustion Engine*. Springer Wien New York, 2007.
- [5] Volvo Group. Volvo group sustainability report 2010: Carbon dioxide neutral transports – future vision of carbon dioxide neutral transport, 2010. <http://reports.volvogroup.com/en/EnvironmentalResponsibility/CarbonDioxideNeutralTransports.html> Retrieved 23rd May, 2016 (download link at top left of page).
- [6] Müller et al. System and control concept for future turbocharger exhaust gas recirculation systems for diesel passenger cars. *BorgWarner Turbo & Emissions Systems: Knowledge Library*, 2005. <http://www.turbos.bwauto.com/press/knowledgeLibrary.aspx> Retrieved 20th June 2016.
- [7] Hall C.A. Dixon S.L. *Fluid Mechanics and Thermodynamics of Turbomachinery*. 5th edition.
- [8] Sonic Performance. Turbochargers: Garrett gtw ball bearing - garrett gtw3884r ballbearing supercore. [http://www.sonicperformance.com.au/841691\\_dash\\_5003S/Garrett-GTW3884R-Ballbearing-Supercore/pd.php](http://www.sonicperformance.com.au/841691_dash_5003S/Garrett-GTW3884R-Ballbearing-Supercore/pd.php) Retrieved 28th August, 2016.

- [9] Tomas Grönstedt. Turbomachinery, tme210 lecture notes: Centrifugal pumps, centrifugal compressors, 2015.
- [10] European Biofuels Technology Platform. Dimethyl ether (dme), 2011. [http://www.biofuelstp.eu/fact\\_sheets.html](http://www.biofuelstp.eu/fact_sheets.html) Retrieved 23rd May, 2016.
- [11] Trucking Info. Dme: An alternative fuel that is coming soon, 2013. <http://www.truckinginfo.com/channel/fuel-smarts/article/story/2013/10/dme-an-alternative-fuel-that-is-coming-soon.aspx> Retrieved 23rd May, 2016.
- [12] Super Street Network. Turbocharge understanding guide - how a turbo works - boost basics: Photo gallery: How a turbo works compressor and turbine, 2009. <http://www.superstreetonline.com/how-to/engine/130-0909-turbocharge-understanding-guide/#photo-05> Retrieved 28th August, 2016.
- [13] Münz et al. Turbocharger for emission concepts with low-pressure-end exhaust-gas recirculation. *BorgWarner Turbo & Emissions Systems: Knowledge Library*, 2007. <http://www.turbos.bwauto.com/press/knowledgeLibrary.aspx> Retrieved 23rd February 2016.
- [14] Volvo Powertrain. Water drain concept mg9 euro5, 2009.
- [15] Volvo Powertrain. Engineering report 660553: Development and initial function test of md13 with a low-pressure egr system featuring an improved resistance to water condensation at compressor intake, 2015.
- [16] Volvo Powertrain. Egr drain test mg9 euro5, 2015.
- [17] Heymann Frank J. Liquid impingement erosion. *Friction, Lubrication, and Wear Technology (ASM International)*, 18:221–231, 1992.
- [18] R. W. Revie and Herbert H. Uhlig. *Uhlig's Corrosion Handbook*. Wiley, Hoboken, N.J, 3rd edition, 2011. Chapter 18.
- [19] Shuji Hattori and Masaya Kakuichi. Effect of impact angle on liquid droplet impingement erosion. *Wear*, 298-299(1):1–7, 2013.
- [20] Shuji Hattori and Makoto Takinami. Comparison of cavitation erosion rate with liquid impingement erosion rate. *Wear*, 269(3):310–316, 2010.
- [21] S. Soni. Analysis of liquid droplet erosion for steam turbine blades of composite material. *International Journal of Mechanical Engineering and Robotics Research*, 1(3):214–226, 2012.
- [22] R. I. Crane. Droplet deposition in steam turbines. *Proceedings of the Institution of Mechanical Engineers, Part C: Journal of Mechanical Engineering Science*, 218(8):859–870, 2004.

- [23] Hiroyuki Kawagishi, Akihiro Onoda, Naoki Shibukawa, and Yoshiki Niizeki. Development of moisture loss models in steam turbines. *Heat Transfer—Asian Research*, 42(7):651–664, 2013.
- [24] Volvo Powertrain. After market training session: Egr drain concept on mg9 euro 5, 2010.
- [25] J. Starzmann, M. V. Casey, and J. F. Mayer. *Water droplet flow paths and droplet deposition in low pressure steam turbines*. 2013.
- [26] M. Ahmad, M. Schatz, and M. V. Casey. Experimental investigation of droplet size influence on low pressure steam turbine blade erosion. *Wear*, 303(1-2):83–86, 2013.
- [27] Toshiyuki Sanada, Masao Watanabe, Minori Shirota, Masao Yamase, and Takayuki Saito. Impact of high-speed steam-droplet spray on solid surface. *Fluid Dynamics Research*, 40(7-8):627, 2008.
- [28] Jr. George F. Schmitt. Liquid and solid particle impact erosion, 1979. <http://www.dtic.mil/dtic/tr/fulltext/u2/a080607.pdf> Retrieved 22nd February, 2016.
- [29] V. N. Amelyushkin and B. N. Agafonov. Special features of erosion wear of rotor blades of cogeneration steam turbines. *Power Technology and Engineering*, 36(6):359–362, 2002.
- [30] Jobaidur R. Khan and Ting Wang. Three-dimensional modeling for wet compression in a single stage compressor including liquid particle erosion analysis. *Journal of Engineering for Gas Turbines and Power*, 133(1):12001, 2011.
- [31] M. Ahmad, M. Casey, and N. Sürken. Experimental assessment of droplet impact erosion resistance of steam turbine blade materials. *Wear*, 267(9):1605–1618, 2009.
- [32] J. H. Brunton G. P. Thomas. Drop impingement erosion of metals. *Proceedings of the Royal Society of London. Series A, Mathematical and Physical Sciences*, 314(1519):549–565, 1970.
- [33] W. Tabakoff, R. Kotwal, and A. Hamed. Erosion study of different materials affected by coal ash particles. *Wear*, 52(1):161 – 173, 1979.
- [34] Benim A. C. and Neuhoff H. G. Analysis of erosion behaviour in a turbocharger radial turbine. *Int. J. for Numerical Methods in Fluids*, 16:259–285, 1993.
- [35] W. Tabakoff and A. Hamed. Effect of environmental particles on a radial compressor. *J. Propulsion*, 5(6):731 – 737, 1989.
- [36] S. et al Karstadt. Effect of water droplets caused by low pressure egr on spinning compressor wheels.  
BorgWarner Turbo Systems Engineering, Germany and FEV, Germany  
[users.telenet.be/veerle\\_haai/Compressor\\_erosion.pdf](http://users.telenet.be/veerle_haai/Compressor_erosion.pdf) Retrieved 23rd February 2016.

- [37] Ghenaiet A. Simulation of particle trajectories and erosion in a centrifugal compressor. *ASME. J. Turbomach.*, 134(5):19 pages, 2012.
- [38] R. W. Revie and Herbert H. Uhlig. *Uhlig's Corrosion Handbook*. Wiley, Hoboken, N.J, 3rd edition, 2011. Chapter 65.
- [39] Joergl et al. Re-introduction unit for lp-egr condensate at/before the compressor, 01 2009. United States Patent Application Publication.
- [40] SRT Forums. Pre-turbo w/i !!! what's your take on it ?, 2006. Post nr. 15, <http://www.srtforums.com/forums/f189/pre-turbo-w-i-what-s-your-take-296709/> Retrieved 7th June, 2016.
- [41] LandRacing. Calculating water injection and placement, 2007. <http://www.landracing.com/forum/index.php?topic=2436.15;wap2> Retrieved 7th June, 2016.
- [42] Andersson R. et al. Andersson, B. *CFD For Engineers*. 2011.
- [43] Crowe T. C. et al. *Multiphase Flow With Droplets and Particles*. CRC Press Taylor & Francis Group, 2nd edition, 2012.
- [44] A. Ghenaiet. Simulations of particulate flows through a radial gas turbine. *Proceedings of 11th European Conference on Turbomachinery Fluid dynamics Thermodynamics*, 2015.
- [45] Nored M. Brun K. and Kurz R. Proceedings of the forty-first turbomachinery symposium. *Turbomachinery Laboratory, Texas A & M University*, 2012.
- [46] Jr. George F. Schmitt. Air psychrometric chart.
- [47] Audizine. Thread: 2001 2.0l comp 5857 build, 2012. Post nr. 42, <http://www.audizine.com/forum/showthread.php/464621-2001-2-01-Comp-5857-Build/page2> Image link [http://px6.streetfire.net/0002/72/99/2042799\\_600.jpg](http://px6.streetfire.net/0002/72/99/2042799_600.jpg) Retrieved 28th August, 2016.
- [48] CD-Adapco. Star-CCM+ Documentation - User Guide - ... - Understanding the K-Omega Wall Treatment.
- [49] CD-Adapco. Star-CCM+ Documentation - User Guide - ... - How Do I Choose A K-Omega Turbulence Model.
- [50] <http://kaffee.50webs.com/Science/activities/Chem/H2O.Vapor.Pressure.Data.html> Retrieved 8th June 2016.
- [51] <http://www.nist.gov/data/PDFfiles/jpcrd231.pdf> Retrieved 8th June 2016.

# A

## Deriving Compressible Flow Relations

Extending the right hand side of Eq. 2.7 gives:

$$\frac{pc}{RT} = \frac{pc\sqrt{\gamma T_0}}{\sqrt{RT}\sqrt{RT}\sqrt{\gamma T_0}} \quad (\text{A.1})$$

where  $c/\sqrt{\gamma RT} = M$  so that:

$$\frac{\dot{m}}{A} = \frac{pc\sqrt{\gamma T_0}}{\sqrt{RT}\sqrt{RT}\sqrt{\gamma T_0}} = \frac{pM\sqrt{\gamma T_0}}{\sqrt{RTT_0}} = \frac{pM}{\sqrt{T_0}} \sqrt{\frac{\gamma}{R}} \sqrt{\frac{T_0}{T}} \quad (\text{A.2})$$

This also leads to:

$$\frac{\dot{m}}{A} = \frac{pM}{\sqrt{T_0}} \sqrt{\frac{\gamma}{R}} \sqrt{\frac{T_0}{T}} \Rightarrow \frac{\dot{m}}{A} = pM \sqrt{\frac{\gamma}{RT}} \Rightarrow M = \frac{\dot{m}}{pA} \frac{\sqrt{RT}}{\sqrt{\gamma}} \quad (\text{A.3})$$

From compressible flow theory in the form of Eq. 2.1, we have  $\frac{T_0}{T} = 1 + \frac{(\gamma-1)}{2} M^2$ , which can be used with Eq. A.1 to give:

$$\frac{\dot{m}}{A} = \frac{pM}{\sqrt{T_0}} \sqrt{\frac{\gamma}{R}} \sqrt{1 + \frac{(\gamma-1)}{2} M^2} \quad (\text{A.4})$$

which becomes:

$$\frac{\dot{m}\sqrt{RT_0}}{pA} = M\sqrt{\gamma}\sqrt{1 + \frac{(\gamma-1)}{2}M^2} \quad (\text{A.5})$$

and, taking the square of both sides:

$$\left(\frac{\dot{m}}{pA}\right)^2 RT_0 = M^2\gamma\left(1 + \frac{(\gamma-1)}{2}M^2\right) \quad (\text{A.6})$$

Now the expression isolates the Mach number. Applying compressible flow relations from Eq. 2.2, it follows that:

$$\left(\frac{P_0}{P}\right)^{\frac{\gamma-1}{\gamma}} = 1 + \frac{\gamma-1}{2}M^2 \quad (\text{A.7})$$

which can be re-arranged to form:

$$\left(\frac{P_0}{P}\right)^{\frac{\gamma-1}{\gamma}} = \frac{1}{2} + \sqrt{\left(\frac{1}{2} + \frac{\gamma-1}{2}M^2\right)^2} = \frac{1}{2} + \sqrt{\frac{1}{4} + 2\frac{1}{2}\frac{\gamma-1}{2}M^2 + \left(\frac{\gamma-1}{2}M^2\right)^2} \quad (\text{A.8})$$

which can be factorised into:

$$\left(\frac{P_0}{P}\right)^{\frac{\gamma-1}{\gamma}} = \frac{1}{2} + \sqrt{\frac{1}{4} + \frac{\gamma-1}{2}M^2\left(1 + \frac{\gamma-1}{2}M^2\right)} = \frac{1}{2} + \sqrt{\frac{1}{4} + \frac{\gamma-1}{2}M^2\frac{T_0}{T}} \quad (\text{A.9})$$

Substituting the Mach number from Eq. A.3 gives:

$$\left(\frac{P_0}{P}\right)^{\frac{\gamma-1}{\gamma}} = \frac{1}{2} + \sqrt{\frac{1}{4} + \frac{\gamma-1}{2}\left(\frac{\dot{m}}{pA}\frac{\sqrt{RT_0}}{\sqrt{\gamma}}\right)^2\frac{T_0}{T}} = \frac{1}{2} + \sqrt{\frac{1}{4} + \frac{\gamma-1}{2}\left(\frac{\dot{m}}{pA}\right)^2\frac{RT_0}{\gamma T}} \quad (\text{A.10})$$

which can be written:

$$\left(\frac{P_0}{P}\right)^{\frac{\gamma-1}{\gamma}} = \sqrt{\frac{1}{4} + \frac{\gamma-1}{2\gamma}\left(\frac{\dot{m}}{pA}\right)^2\frac{RT_0}{T}} = \sqrt{\frac{1}{4} + \frac{\gamma-1}{2\gamma}\left(\frac{\dot{m}}{pA}\right)^2RT_0} \quad (\text{A.11})$$

All in all:

$$\left(\frac{P_0}{P}\right)^{\frac{\gamma-1}{\gamma}} = \frac{1}{2} + \sqrt{\frac{1}{4} + \frac{\gamma-1}{2\gamma}\left(\frac{\dot{m}}{pA}\right)^2RT_0} \quad (\text{A.12})$$

and finally:

$$P_0 = P \left( \frac{1}{2} + \sqrt{\frac{1}{4} + \frac{\gamma - 1}{2\gamma} \left( \frac{\dot{m}}{pA} \right)^2 RT_0} \right)^{\frac{\gamma}{\gamma-1}} \quad (\text{A.13})$$

# B

## Relating Pumps by Flow Coefficient

Assume that two pumps  $a$  and  $b$  are similar in everything except size, and that the sizes are related as  $D_a = 0.75D_b$ . Equating the flow coefficients then gives:

$$\phi_a = \phi_b \Rightarrow \frac{Q_a}{N_a D_a^3} = \frac{Q_b}{N_b D_b^3} \quad (\text{B.1})$$

The following relationship can then be formed from the diameter correlation :

$$\frac{Q_a}{N_a (0.75D_b)^3} = \frac{Q_b}{N_b D_b^3} \Rightarrow N_a (0.75D_b)^3 = N_b D_b^3 \quad (\text{B.2})$$

which, given the same flow rate  $Q_a = Q_b$ , leads to the following relationship between the rotational speeds of  $b$  and  $a$ :

$$\frac{N_b}{N_a} = \frac{0.42D_a^3}{D_a^3} \Rightarrow \frac{N_b}{N_a} = 0.42 \quad (\text{B.3})$$

Hence, a larger compressor  $b$  will need to rotate more slowly to achieve the same pressure ratio at a given flow rate.

# C

## Derivation of Explicit Droplet Impulse

Recognising the fact that impact area can, using Eq. 2.13, be written as:

$$A_{impact} = \pi r_{contact}^2 = \pi \left( R \frac{v_{impact}}{a_l} \right)^2$$

It is then possible to re-write Eq. 2.17 using this and Eq. 2.12 as well as the definition for  $t_2$  from Eq. 2.16:

$$I = P_{impact} A_{impact} t_2 = \frac{R}{v_{impact}} \left( 1 - \sqrt{1 - \frac{v_{impact}^2}{a_l^2}} \right) \rho_l a_l v_{impact} \left( 1 + \frac{k v_{impact}}{a_l} \right) \pi \left( R \frac{v_{impact}}{a_l} \right)^2 \quad (C.1)$$

Which can be simplified to:

$$I = P_{impact} A_{impact} t_2 = \frac{R}{v_{impact}} \left( 1 - \sqrt{1 - \frac{v_{impact}^2}{a_l^2}} \right) \rho_l a_l v_{impact} \left( 1 + \frac{k v_{impact}}{a_l} \right) \pi \left( R \frac{v_{impact}}{a_l} \right)^2 \quad (C.2)$$

and further:

$$I = \frac{R}{v_{impact}} \left( 1 - \sqrt{1 - \frac{v_{impact}^2}{a_l^2}} \right) \rho_l v_{impact} (a_l + k v_{impact}) \pi \left( R \frac{v_{impact}}{a_l} \right)^2 \quad (\text{C.3})$$

Finally:

$$I = \left( 1 - \sqrt{1 - \frac{v_{impact}^2}{a_l^2}} \right) \rho_l (a_l + k v_{impact}) \pi R^3 \left( \frac{v_{impact}}{a_l} \right)^2 \quad (\text{C.4})$$

# D

## Erosion of Coal Ash on Aluminium

The coefficients introduced in Eq. 2.20 for aluminium are defined in Table D.1 below:

**Table D.1:** Numerical values of coefficients used in calculations. Here  $\beta_0$  represents the angle for the greatest erosion (approx.  $25^\circ$  for aluminium), input in radians to calculate  $A_3$ .

Coefficient	Value for Aluminium	Value for Steel
$A_1$	$1.5699 \cdot 10^{-6}$	$1.5051 \cdot 10^{-6}$
$A_2$	0.3193	0.296
$A_3$	$\frac{90}{\beta_0} = \frac{90}{25 \cdot 2\pi/360} = 206.2648$	206.2648
$A_4$	0.0016	0.0016
$A_5$	$2 \cdot 10^{-12}$	$5 \cdot 10^{-13}$

# E

## Karstadt et al. Study Parameters

Presented here is a summary of parameters from the Karstadt et al. study [36] which is much referred to throughout this work. Values in bold are original values, other values have been calculated or deduced from these. Parameters general to the whole setup are given in the following list:

- ★  $\mathbf{d} = 47.5 \cdot 10^{-3} \text{ m}$
- ★  $r = d/2$
- ★  $\mathbf{r}_{\text{inj}} = \frac{2}{3}\mathbf{r}$
- ★  $U = \Omega \cdot r_{\text{inj}}$
- ★  $\mathbf{c}_{\text{droplets}} = 24.5 \text{ m/s}$
- ★ Assume most of the incoming droplet/gas velocity is axial
- ★  $w = \sqrt{c^2 + U^2}$

Table E.1 gives values for the experiment that varied droplet size; Table E.2 gives values for the rotational speed variation experiment.

**Table E.1:** Experiment varying droplet size. Rotational speed  $n = 150 \text{ krpm}$ .

Parameter				
$\mathbf{d}_{\text{droplet}} (\mu\text{m})$	<b>153</b>	<b>340</b>	<b>470</b>	<b>1120</b>
$r_{\text{droplet}} (\mu\text{m})$	76.5	170	235	560
$\dot{\mathbf{Q}} (\text{l/h})$	<b>0.54</b>	<b>1.26</b>	<b>3.2</b>	<b>11.3</b>

**Table E.2:** Experiment varying the rotational speed of the compressor. It is shown which relative velocities have been extracted from this data. The droplet size for this experiment was  $d_{droplet} = 470 \mu\text{m}$ .

Parameter				
<b>n</b> (krpm)	<b>50</b>	<b>100</b>	<b>150</b>	<b>200</b>
$\Omega = 1000 \cdot 2 \cdot \pi / 60n$ (rad/s)	5236	10472	15708	20944
$U = \Omega \cdot r_{inj}$ (m/s)	82.9	165.8	248.7	331.6
$w$ (m/s)	86.4	167.6	249.9	332.5

# F

## Grid Independence Study

**Table F.1:** Number of cells in the different parts of the computational meshes used for the grid independence study performed for the CFD calculations. The study was performed for the geometry of turbo compressor with the central nozzle installed.

Base Size	Diffuser	Impeller	Inlet	Total
$5 \cdot 10^{-3}$ m	13237	168378	21829	203444
$25 \cdot 10^{-4}$ m	33645	487727	66182	587554
$2 \cdot 10^{-3}$ m	46695	658712	95650	801057
$15 \cdot 10^{-4}$ m	88128	938458	186558	1213144
$1 \cdot 10^{-3}$ m	196664	1777815	390411	2364890
$9 \cdot 10^{-4}$ m	242597	2142098	509563	2894258
$8 \cdot 10^{-4}$ m	317180	2603628	747669	3668477
$5 \cdot 10^{-4}$ m	905688	7282531	1989429	10177648

# G

## Fraction of Particles Impinged

Presented here are the numerical values from work by Ghenaiet referred to in Section 3.3.7. Using select values from “Table 2” in Ghenaiet [37], it is possible to calculate the amount of particles impinging on the main blade for a fixed compressor speed, but varied concentrations of sand, see Table G.1

**Table G.1:** Values extracted from Ghenaiet [37] for 60 000 rpm.

Conc (mg/m <sup>3</sup> )	$\zeta$ (mg main blade eroded)	$\varepsilon$	Impacted g/s	Admitted g/s	Hit fraction %
50	8.4057	1.4103	0.0017	1.6555	1.0001
100	16.5771	1.3373	0.0034	3.3432	1.0299
150	24.8148	1.391	0.0050	4.9554	1.0000
200	34.1457	1.4326	0.0066	6.6203	1.0001
300	50.5884	1.4177	0.0099	9.9115	1.0001

The same procedure can then be repeated for one concentration but at different rotational speeds. This is done as shown in Table G.2:

**Table G.2:** Values extracted from Ghenaiet [37] for 150 mg/m<sup>3</sup> concentration.

rpm	$\zeta$ (mg main blade eroded)	$\varepsilon$	Impacted g/s	Admitted g/s	Hit fraction %
40k	3.275	0.3683	0.0025	2.4701	1.0000
60k	24.8148	1.391	0.0050	4.9554	1.0000
80k	60.7177	2.8657	0.0059	5.8854	1.0000
100k	115.514	4.9345	0.0065	6.5024	1.0000

# H

## Results For Cases I and II

CFD results for the higher operational points of Case I and Case II (as marked in Fig. 3.3) are given below. This is to compare calculated compressor performance for different cases with what is expected from the compressor map. The geometry and mesh is the same as for Case III, i.e. without the nozzle. The model and solver choices are the same as Cases III and IV. The parameters set to correspond to operational points I and II are given in Table H.1.

**Table H.1:** The conditions set in Star-CCM+ for the operating points representing Case I and Case II.

CFD Setup	Case I	Case II
Mass flow total (kg/s)	0.42	0.347
Mass flow set (kg/s)	0.06	0.04957
Static pressure diffuser outlet (Pa)	317000	215000
Static temperature diffuser outlet (K)	480	415
Rotational speed (rpm)	121300	100000
Pressure ratio $P_{03}/P_{01}$ from map	3.793	2.775

**Table H.2:** A summary of the most important monitored quantities for CFD Case I and Case II. The last two rows are based on the calculated value  $P_{03}$ , the derivation of which is outlined in Section 3.2.2.

CFD Results	Case I	Case II
Static pressure diffuser outlet (Pa)	301351	215000
Static pressure inlet (Pa)	97140	97067.9
Mass flow (kg/s)	0.06	0.04957
Total pressure diffuser outlet (Pa)	410688.5	276526.8
Total pressure inlet (Pa)	98456.2	97999.1
Calculated total pressure volute outlet $P_{03}$ (kg/s)	357181	248693.5
Pressure ratio $P_{03}/P_{01}$ calculated	3.628	2.538

The difference in relative Mach numbers at mid blade span for Cases I and II can be seen in Fig. H.1, and at tip span in Fig. H.2.

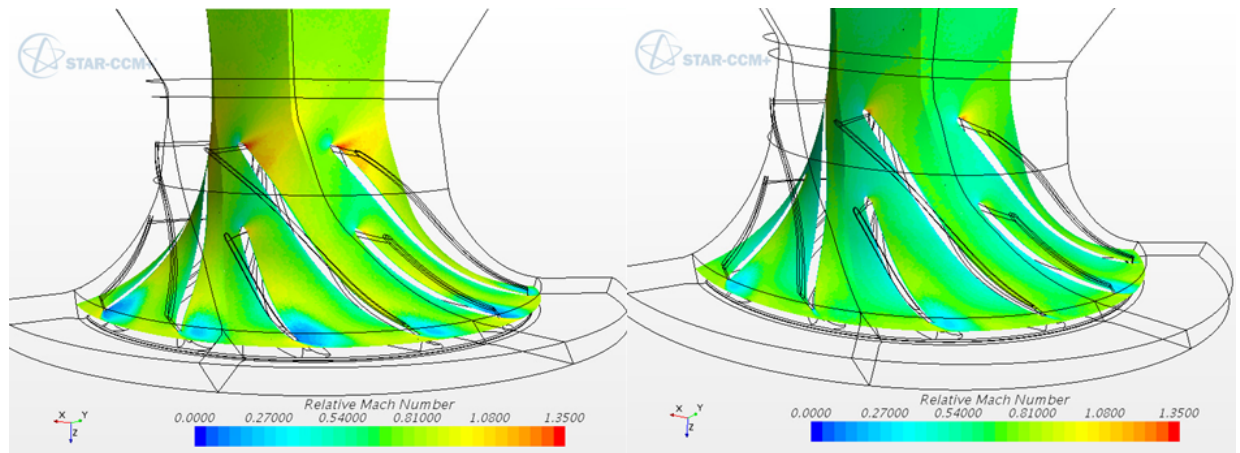


**Figure H.1:** Relative Mach number at mid blade span for Case I (left) and II (right).

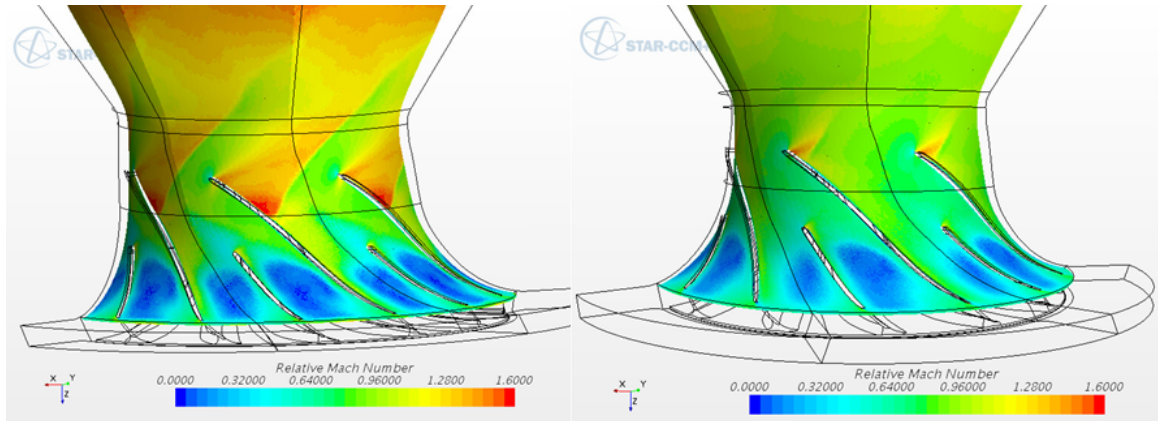


**Figure H.2:** Relative Mach number at blade tip span for Case I (left) and II (right).

Views of the static pressure distribution through the impeller for both cases can be seen in Fig. H.3.

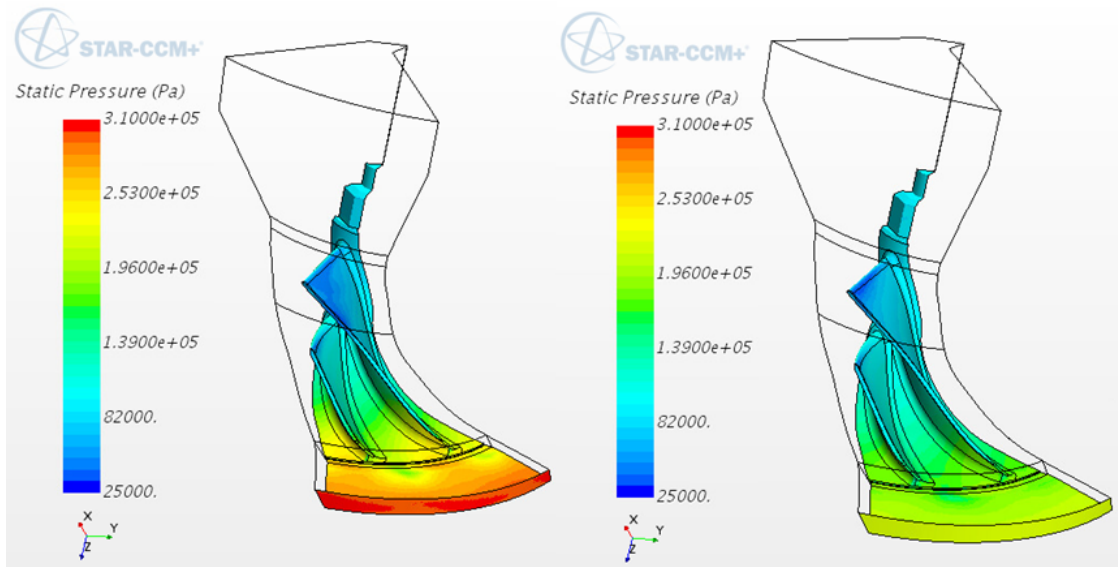


**Figure H.3:** Static pressure distribution throughout the impeller for Case I (left) and II (right).

The  $y^+$  for two different views of Cases I and II are shown in Fig. H.4 and Fig. H.5. It can be seen that the  $y^+$  values in the diffuser are higher than would be desired.

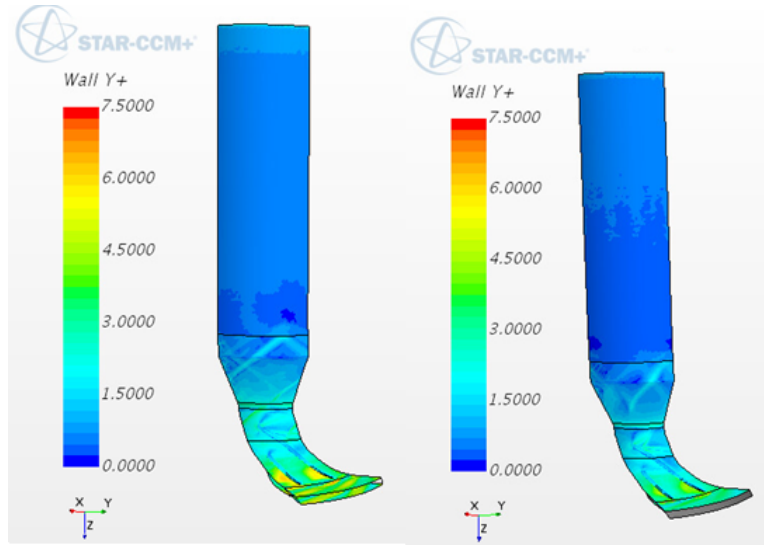


Figure H.4: Wall  $y+$  values for one view of Cases I (left) and II (right).

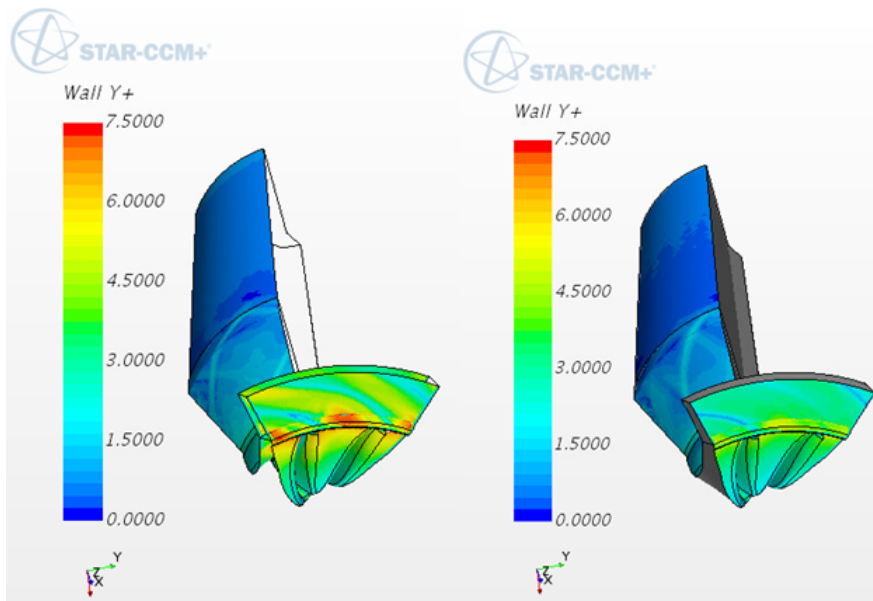
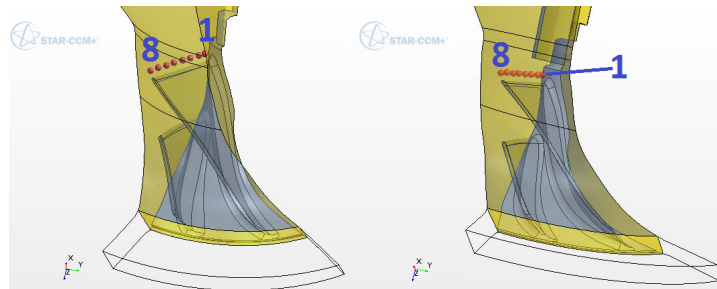


Figure H.5: Wall  $y+$  values for one view of Cases I (left) and II (right).

# I

## Calculation of Stokes Number

For Cases III and IV, the numerical values for dynamic viscosity and density used to calculate the Stokes number are given in Tables I.1 and I.2. The positions 1-8 in the tables represent the different measurement points. Figure I.1 indicates where these points are located for the two cases.



**Figure I.1:** Illustrating the measurement positions used to determine values of local flow density and dynamic viscosity for the calculations of Stokes numbers for cases with and without the nozzle.

**Table I.1:** Dynamic viscosity for Case III and IV. The measurements are taken along 8 points just above the blade leading edge. These points are shown in Fig. I.1.

Position	Dynamic viscosity (Pas)	
	Case III	Case IV
1	1.828949e-05	1.855360e-05
2	1.831419e-05	1.849994e-05
3	1.830686e-05	1.816061e-05
4	1.831902e-05	1.815616e-05
5	1.832486e-05	1.814104e-05
6	1.833231e-05	1.813521e-05
7	1.837315e-05	1.815157e-05
8	1.838711e-05	1.826810e-05

**Table I.2:** Density for Case III and IV. The measurements are taken along 8 points just above the blade leading edge. These points are shown in Fig. I.1.

Position	Density (kg/m <sup>3</sup> )	
	Case III	Case IV
1	1.141384	1.121255
2	1.144180	1.123174
3	1.140439	1.138901
4	1.140134	1.137818
5	1.138359	1.134961
6	1.134986	1.133748
7	1.134389	1.137209
8	1.125196	1.121680

# J

## Mixing Temperature Cases III-IV

$$T_{EGR} = 35^\circ\text{C}$$

$$T_{air} = 22^\circ\text{C}$$

$$\dot{m}_{air} = 0.0237428 \text{ kg/s}$$

$$\dot{m}_{EGR} = 0.00452571 \text{ kg/s}$$

Enthalpy balance:

$$c_{p,EGR}\dot{m}_{EGR}\Delta T_{EGR} = c_{p,air}\dot{m}_{air}\Delta T_{air}$$

Assuming that the EGR has the same properties as air means that the specific heats  $c_p$  cancel out:

$$\dot{m}_{EGR}(T_{mix} - T_{air}) = c_{p,air}\dot{m}_{air}(T_{EGR} - T_{mix})$$

which leads to:

$$T_{mix} = \frac{T_{EGR}\dot{m}_{EGR} + T_{air}\dot{m}_{air}}{\dot{m}_{EGR} + \dot{m}_{air}}$$

which, inserting numerical values, becomes:

$$T_{mix} = \frac{35 \cdot 0.00452571 + 22 \cdot 0.0237428}{0.0237428 + 0.00452571} = \frac{0.6807}{0.02826851} = 24^\circ\text{C}$$